TECHNISCHE UNIVERSITÄT WIEN

Institut für Fertigungstechnik und Hochleistungslasertechnik

Master Thesis

Studies for the determination of the process dynamics with Finite Element Method on a BTA deep hole drilling machine

conducted for the purpose of attainment of the academic degree of
Master of Science under the instruction of
Univ.-Prof. Dipl. Ing. Dr. Bleicher
(Institute for Production Engineering and Laser Technology)
submitted to Vienna University of Technology
Faculty of Mechanical and Industrial Engineering

by
Wang Chao
0928641 (066 445)
Linzerstrasse 283-8
Vienna, Austria

Vienna, 10.10.2016 Chao Wang

Ich habe zur Kenntnis genommen, dass ich zur Drucklegung meiner Arbeit unter der Bezeichnung

Diplomarbeit

nur mit Bewilligung der Prüfungskommission berechtigt bin.

Ich erkläre weiters an Eides statt, dass ich meine Diplomarbeit nach den anerkannten Grundsätzen für wissenschaftliche Abhandlungen selbstständig ausgeführt habe und alle verwendeten Hilfsmittel, insbesondere die zugrunde gelegte Literatur, genannt habe.

Weiters erkläre ich, dass ich dieses Diplomarbeitsthema bisher weder im In- noch Ausland einer Beurteilerin/einem Beurteiler zur Begutachtung in irgendeiner Form als Prüfungsarbeit vorgelegt habe und, dass diese Arbeit mit der vom Begutachter beurteilten Arbeit übereinstimmt.

Wien, 10.10.2016 Chao Wang

Acknowledgement

I would like to thank my instructors Professor. Friedrich Bleicher and MSc. Andreas Steininger for their patient help during the working process of this thesis. And I would like to thank CADFEM (Austria) GmbH for the excellent support with the setup of simulation in Ansys Workbench 16.0.

Abstract

BTA (Boring and Trepanning Association) deep hole drilling is a widely applied cutting method to manufacture or process bores. In this thesis, numerical simulations with Finite Element Method for the determination of eigenfrequencies of a BTA deep drilling machine in real boundary and working conditions are executed with Ansys Workbench in order to study dynamic disturbance during deep hole drilling processes. The pre-stressed modal analysis gives the information regarding varying dominant eigenmodes and the corresponding critical locations on the boring bar of BTA tool with different drilling depths. To prevent chatter vibration and spiralling during the deep hole drilling process, a real-time monitoring of varying system dynamics would be recommended and the results from the simulation are considered as reliable references in this case. Furthermore, the influences of the one-way Fluid-Structure Interaction, drilling-depth dependent values of boundary conditions and material damping effect are proven not to be neglected comparing to the influence of mechanical loads on BTA tool head in modal analysis.

Keywords: Deep Hole Drilling, BTA, Modal Analysis, Finite Element Method, Fluid-Structure Interaction, Rotor Dynamics, Effective Modal Mass.

Abbreviations

BTA	Boring and Trepanning Association
FEM	Finite Element Method
FSI	Fluid-Structure Interaction
CFD	Computational Fluid Dynamics
ACF	Autocorrelation Function
MPC	Multi-Point-Constraint
RMS	Root Mean Square
SSE	Sum of Squared Errors

Nomenclatures

C	-	Damping matrix
$c_{SB,1}, c_{SB,2}$	$\frac{Nms}{rad}$	Torsional damping factors of stuffing box
D_b	mm	External diameter of BTA boring bar
d_b	mm	Internal diameter of BTA boring bar
D_h	mm	External diameter of BTA tool head
D_{LD}	m	Distance between clamping end and Lanchester damper
$D_{SB,1}, D_{SB,2}$	m	Distances between clamping end and stuffing box
E_b	MPa	Elastic modulus of material of BTA boring bar
E_{cg}	MPa	Elastic modulus of material of cutters and guide pads
E_h	MPa	Elastic modulus of the material of BTA tool head
F	N	Total cutting force
F_{axial}	N	Axial force
$\vec{f}$	-	Vector of external excitation and force
$\vec{f}_f$	N	Body force in fluid domain

$\vec{f_s}$	N	Body force in solid domain
$f_{exp,i},\ f_{num,i}$	Hz	Experimental and numerical values of i-th eigenfrequency
K	-	Stiffness matrix
k_{LD}	$\frac{N}{m}$	Elastic stiffness of Lanchester damper
$k_{SB,1}, k_{SB,2}$	$\frac{N}{m}$	Elastic stiffness of stuffing box
k_W	$\frac{N}{m}$	Elastic stiffness of workpiece
L_b	mm	Length of BTA boring bar without the thread
L_{bc-ld}	mm	Distance between Lanchester damper and boring bar chuck
L_{cl}	mm	Length of clamp in boring bar chuck
L_{LD}	mm	Length of Lanchester damper
$L_{LD,left}, L_{LD,right}$	mm	Ineffective lengths of Lanchester damper
L_h	mm	Length of BTA tool head
L_{sb}	mm	Dual spacing of the stuffing box
L_{th}	mm	Length of thread
M	-	Mass matrix
$M_N,\ M_P$	Nm	Bending moment in normal and passive directions
M_T	Nm	Torsional moment
$\bar{M}$	-	Generalized mass matrix
$m_{eff,j}$	kg	Effective modal mass for mode j
$\vec{n_f}, \vec{n_s}$	-	Normal vectors at FSI interface from fluid and solid domains
$\vec{u_f}, \vec{u_s}$	-	Displacements in fluid and solid domains at FSI interface
v_c	$\frac{Liter}{min}$	Flow speed of fluid
$\vec{v_f}$	-	Vector of velocity in fluid domain
$\vec{v_s}$	-	Vector of velocity in solid domain
x_1, x_2	-	Degrees of freedoms of the vibration
α	$\frac{1}{s \cdot rad}$	Material proportional damping factor
β	s	Material proportional damping factor
$\bar{\Gamma}$	-	Coefficient vector
μ_{cg}	-	Poisson´s ratio of material of cutters and guide pads

μ_h	-	Poisson´s ratio of material of BTA tool head
μ_b	-	Poisson´s ratio of material of BTA boring bar
ν_f	$\frac{mm^2}{s}$	Viscosity of cutting fluid
ξ	-	Unit ground displacement vector
ρ_b	$\frac{kg}{m^3}$	Density of material of BTA boring bar
ρ_{cg}	$\frac{kg}{m^3}$	Density of material of cutters and guide pads
ρ_f	$\frac{g}{ml}$	Density of cutting fluid
ρ_h	$\frac{kg}{m^3}$	Density of material of BTA tool head
ρ_s	-	Density in solid domain
σ_f	-	Stress tensor in fluid domain
σ_s	-	Stress tensor in solid domain
Φ_j	kg	Modal participation factor for mode j
Ψ	-	Eigenvector matrix
ω	-	Eigenvalue of dynamic system
$\frac{D}{Dt}$	-	Material derivative
$\frac{\partial}{\partial t}$	-	Partial derivative with respect to time
∇	-	Nabla symbol

Contents

1 Introduction

Boring and Trepanning Association (BTA) deep hole drilling is applied to manufacture deep holes with a diameter starting from 6 mm and a length to diameter ratio larger than 3 (l/d>3)[1]. During the deep hole drilling processes, the cooling lubricant is supplied through the gap between the BTA tool and the workpiece and flushes the cutting chips out via the inner of the boring bar. BTA deep hole drilling machines could be applied for solid drilling, trepanning and boring. The qualities of the manufactured bores, such as bore diameter, surface roughness, mismatch of axes etc.[1] are often influenced by the superposition of torsional and flexural vibrations, which cause dynamic disturbance in deep hole drilling processes and are known as chatter vibration and spiralling. Chatter vibration could damage the BTA tool and create harsh noise while spiralling leads to a multi-lobe shaped cross section of the manufactured bore, increases the roundness error and damages the inner surface of the produced bore. This thesis is considered as a part of the research regarding dynamic disturbance in deep hole drilling processes with BTA deep hole drilling machines. In this thesis, the solid drilling process with a BTA deep hole drilling machine is the basis for the simulation. The relation between the eigenfrequencies and varying boundary and working conditions is studied. The dependency of eigenfrequencies of a BTA deep hole drilling machine on the varying drilling depth is investigated, as the drilling depth is an essential factor that influences the eigenfrequencies. All boundary and working conditions are taken into consideration, such as the influences of cooling lubricant flow, mechanical loads and damping effects, the elastic support between the Lanchester damper and the boring bar, the one between the stuffing box and the boring bar and the one between the workpiece and the tool head. The numerical simulation is based on the finite element method (FEM) and coupled with computational fluid dynamics (CFD). The results of the simulation are worthy of reference for further studies regarding dynamic disturbance during BTA deep hole drilling processes and could contribute to further researches regarding countermeasures against chatter vibration and spiralling, especially in the areas for the real-time monitoring and operating reference.

2 State-of-the-art

2.1 Backgrounds

BTA deep hole drilling belongs to the family of conventional deep hole drilling methods and has a good reputation for high quality of finish. Figure 2.1 shows a conventional BTA deep hole drilling machine. Fritz et al. [6] have declared that deep hole drilling methods comparing to conventional drilling methods have advantages in terms of drilling performance, surface quality after machining and machining of hard material. However, the discrepancy comparing to the ideal flawless process impairs the quality of the produced bore and is generally caused by the so-called self-excited vibration during the hole drilling process. The self-excited torsional vibration, which is known as chatter vibration, leads to creation of noise and severe wear of BTA tool during drilling process. The self-excited bending vibration, which is also known as spiralling or twisted drilling, leads to poor qualities of hole surface in terms of the roughness, roundness error, surface texture and mismatch of axes. Sometimes it could lead to an useless workpiece. The BTA boring tool is susceptible to these vibrations due to its slender geometry, which leads to small torsional and bending stiffness. The influence of the self-excited vibration must be avoided as BTA deep hole drilling is usually applied for the last machining procedure and hence the cost could be tremendous. Researches have shown that torsional and bending eigenfrequencies are interrelated with chatter vibration and spiralling respectively. Therefore the cognizance of the eigenfrequencies of BTA deep drilling machine in different drilling depths and different boundary and working conditions is of vital importance to predict, counteract or avoid chatter vibration and spiralling in the deep hole drilling process.

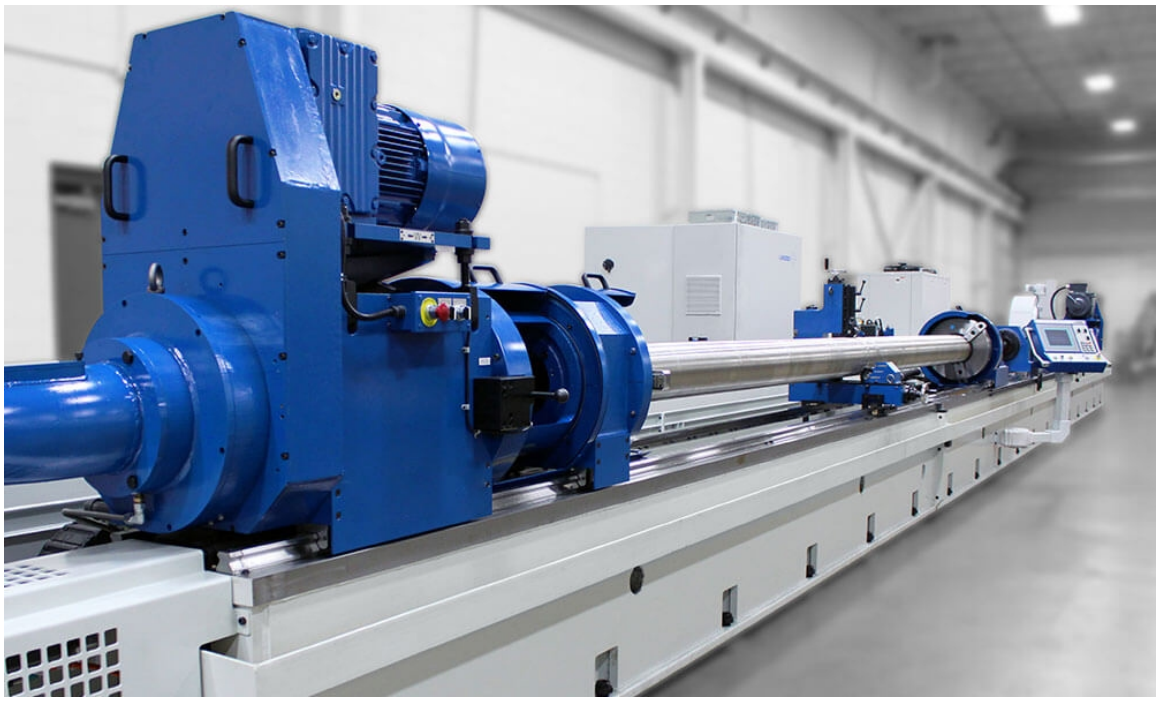

Figure 2.1: A conventional BTA deep hole drilling machine [35].

2.2 Setup and working principle of general BTA deep drilling machines

The general setup and working principle of a BTA deep drilling machine are shown in figure 2.2 and 2.3 respectively. In figure 2.2 the left end of the boring bar is clamped to the left drive unit via the boring bar chuck. A Lanchester damper that is fixed on the machine bed is applied on the boring bar. The stuffing box for the coolant supply gives support on the boring bar and the joint between the stuffing box and workpiece is sealed. Figure 2.4 shows the setup of the Lanchester damper. Figures 2.5 and 2.6 show the setup of the stuffing box in the coolant supply unit.

In figure 2.3, the BTA drilling tool consists of one tool head (10), two guide pads (1 and 4) and one cutting edge (3). The tool head is connected to the boring bar (8) via the screw joint (9). During a machining process the cooling lubricant (7) flows from the inlet of the stuffing box through the gap between the BTA tool and the workpiece to reach the chip mouth (2) and then flushes out the cutting chips via the cylindrical cavity inside the tool head and the boring bar. The seal (5) between the workpiece and the stuffing box prevents the leakage of coolant. The drilling bush (6) contributes to the stable starting drilling phase of the drilling process. The explanation for the notations in figure 2.3 is seen in table 2.1.

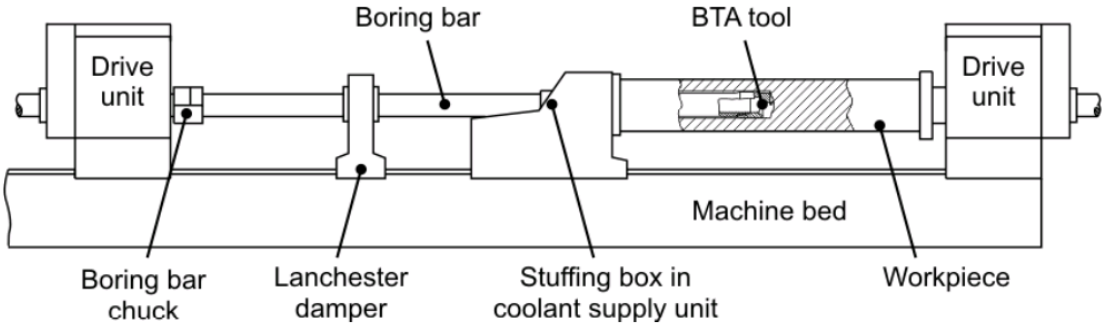

Figure 2.2: General setup of BTA deep drilling machine [15].

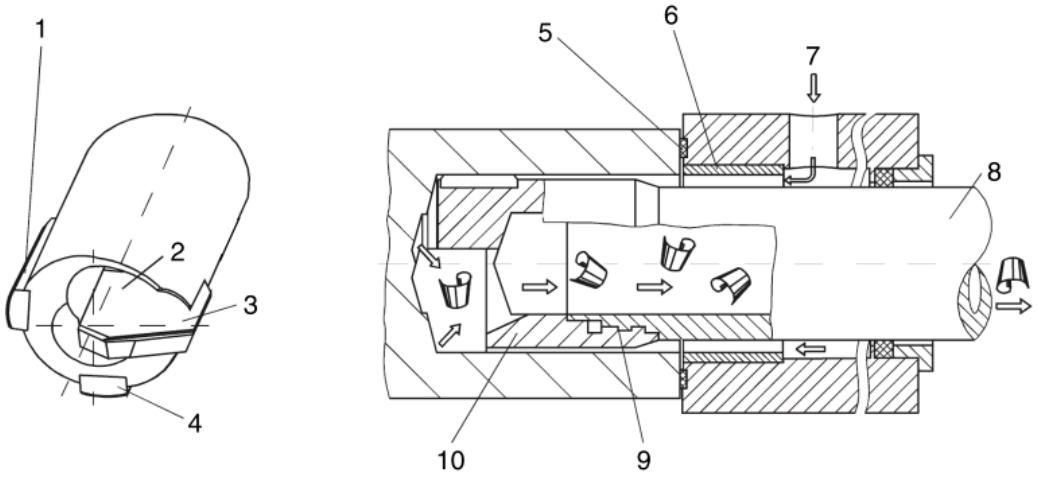

Figure 2.3: Working principle of BTA deep drilling machine according to [1].

Number	Description	Number	Description
1	Guide pad 1	6	Drilling bush
2	Chip mouth	7	Cooling lubricant
3	Cutting edge	8	Boring bar
4	Guide pad 2	9	Screw joint
5	Seal	10	Tool head

Table 2.1: Explanation for the notations in figure 2.3.

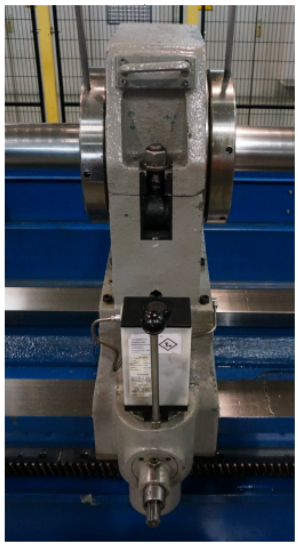

(a) A conventional Lanchester damper. Source: IFT, TU Wien

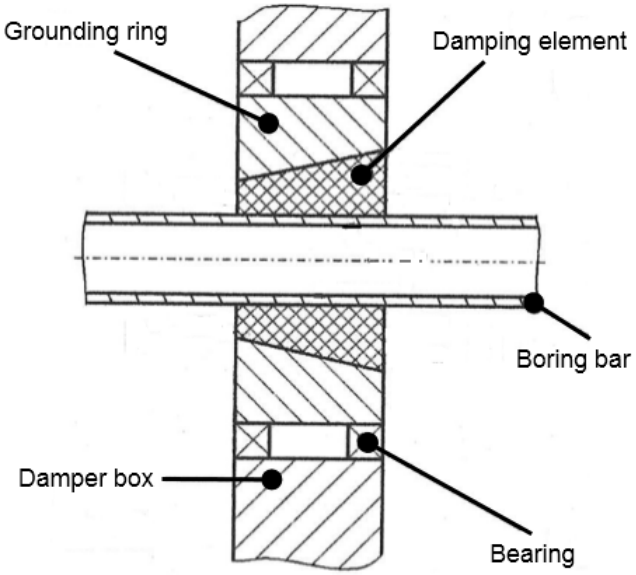

(b) Sketch of a Lanchester damper [18].

Figure 2.4: General setup of a Lanchester damper.

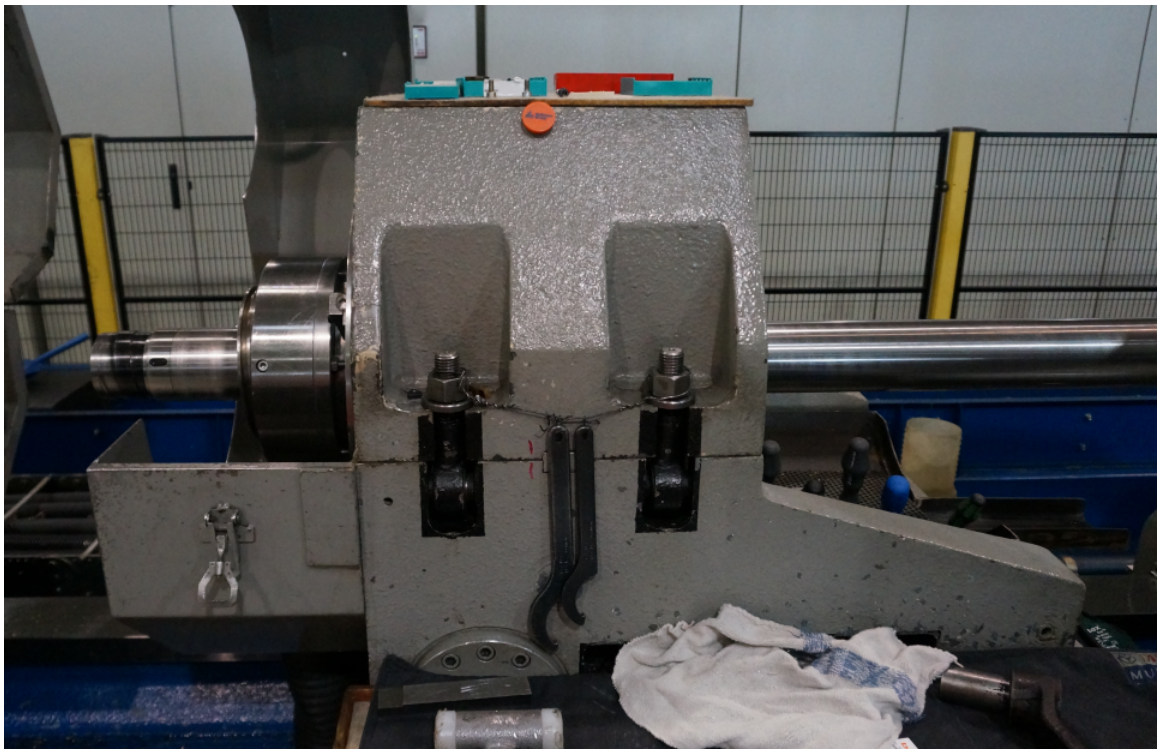

Figure 2.5: A conventional stuffing box. Source: IFT, TU Wien

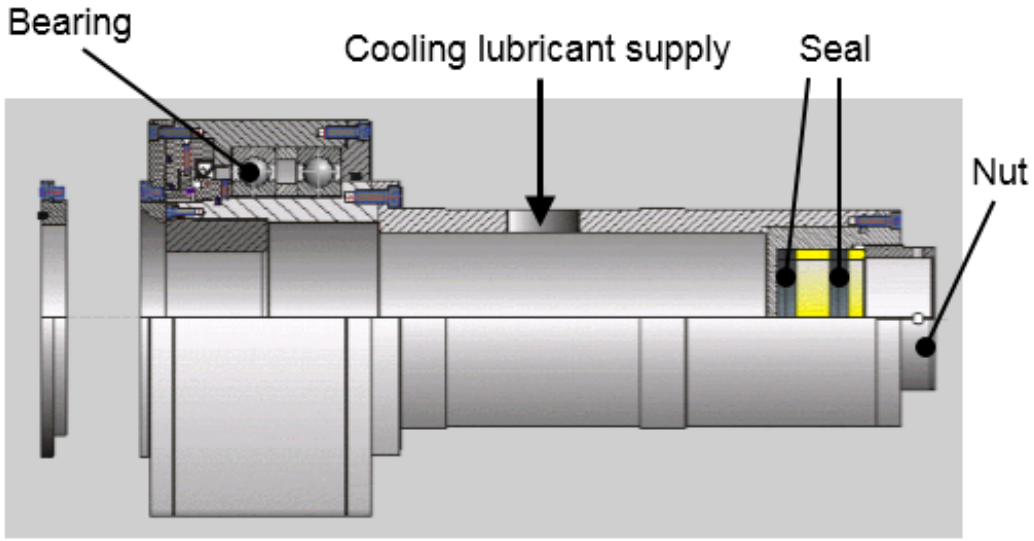

Figure 2.6: Sketch of a stuffing box [36].

The workpiece is clamped with the drive unit on the right-hand side (seen in figure 2.2). This leads to three available operating modes, which are seen in figure 2.7 and 2.8.

- Rotating BTA tool with fixed workpiece, feed from the tool or workpiece.
- Rotating workpiece with fixed BTA tool, feed from the tool.
- Rotating BTA tool with rotating workpiece in the opposite direction, feed from the tool.

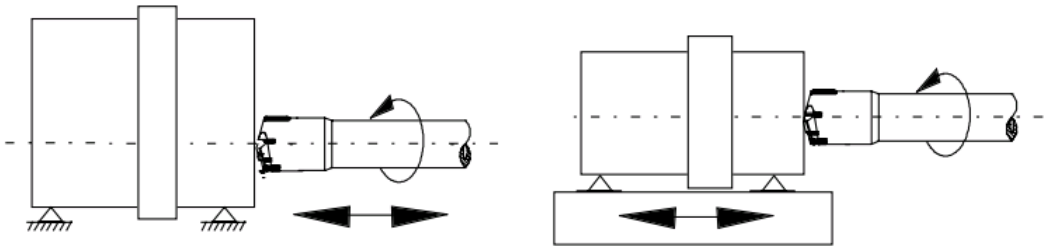

(a) Rotating BTA tool with fixed workpiece, feed from the tool.

(b) Rotating BTA tool with fixed workpiece, feed from the workpiece.

Figure 2.7: Rotating BTA tool with fixed workpiece [1].

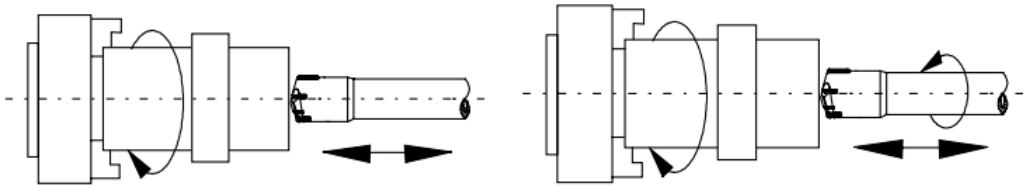

(a) Rotating workpiece with fixed BTA tool, feed from the tool.

(b) Rotating BTA tool with rotating workpiece in the opposite direction, feed from the tool.

Figure 2.8: Rotating workpiece with fixed BTA tool and rotating BTA tool with rotating workpiece in the opposite direction [1].

Due to the big ratio between length and diameter of the manufactured hole, BTA deep drilling method is susceptible to dynamical instability. The quality of the via BTA deep drilling method manufactured bores are often influenced by the superposition of torsional and flexural vibrations, which cause dynamic disturbance during drilling processes and are also known as chatter vibration and spiralling. Chatter vibration is mainly caused by self-excited torsional vibration, which leads to severe wear of boring tool and creates harsh noises during drilling process. Spiralling is generated from self-excited bending vibration, which leads to a helical propagation of hole with multi-lobe cross section along the drilling axis. A brief introduction to the self-excited vibration is given as follows.

2.3 Self-excited vibration

As mentioned before, chatter vibration and spiralling result from self-excited torsional and bending vibration respectively. The causes of self-excited vibration have been studied by many researchers so far and three major reasons are stated as follows:

- Regenerative effect.
- Positional coupling.
- Falling characteristic curve of drilling moment.

The third reason above is according to [18] not as important as the other two because it is usually seen in processing with low cutting speed and not considered as a main factor for BTA deep drilling process nowadays. Tlusty et al. [9] have given the mathematical derivation of characteristic equations for self-excited vibration of a simplified model based on regenerative effect plus positional coupling principle and obtained the analytical criteria of stability for both principles. Therefore the first and second reasons are considered as main reasons for self-excited vibration in BTA deep hole drilling process and will be introduced as follows.

2.3.1 Regenerative effect

During a deep hole drilling process, a pulse-like excitation is easily triggered by e.g. noise floor or static unbalance in the machine operation. This kind of excitation leads to eigenvibrations of the machine, which force the cutting movement on the surface of the workpiece into a wave-like shape in accordance with eigenfrequencies of the machine. After repeated cutting in the wave-like shape, which means repeated excitation with eigenfrequencies of the machine, the relative vibration between machine and workpiece could exceed the restriction of damping and stiffness of the machine, which means the cutting in the wave-like surface of the workpiece is unable to be stopped. Weck et al. [10] established a simplified model based on control engineering and gave the criteria of stability for self-excited vibration due to regenerative effect and positional coupling principle with Nyquist plot. This resulted the conclusion regarding influence factors of chatter vibration and appropriate countermeasures were also proposed. The illustration of regenerative effect is shown in figure 2.9 [11]. Here v_c represents the cutting speed and F represents the total cutting force. An arbitrary pulse-like excitation, which leads to the eigenvibration of the machine, leaves a wave-like surface on the workpiece after cutting, with however a possibly declining amplitude of the vibration due to the existing damping and stiffness. After each rotation, the machine is excited again into its eigenvibration due to the cutting into the previously manufactured wave-like surface. At last, the cutting and producing of the wave-like surface of the workpiece are uncontrollably repeated due to the limited stiffness and damping properties of the machine.

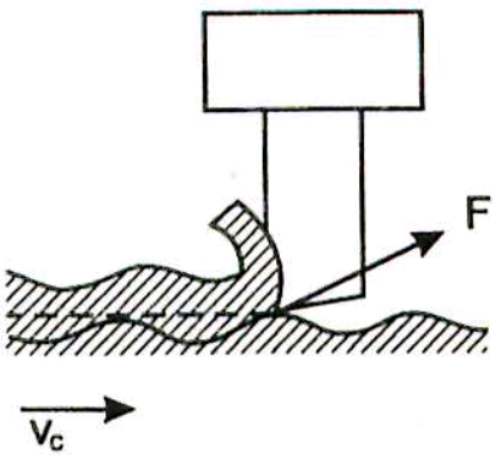

Figure 2.9: Regenerative effect of a simplified cutting process [11].

2.3.2 Positional coupling

If the vibration of the cutting edge of the BTA tool is in more than one direction possible, which also means the relative movement between the cutting edge and the workpiece possesses at least two degrees of freedom, then positional coupling is considered as the major cause for the self-excited vibration. Thai [12] has confirmed positional coupling as the main reason of self-excited torsional vibration based on theoretical stability analysis combining experiments. He also gave suggestions to improve the Lanchester damper and the recognition of self-excited vibrations. A simplified illustration of this principle is shown in figure 2.10 [10]. Here v_c represents the cutting speed, x_1 and x_2 represent the two degrees of freedom in the vibrations and F represents the total cutting force. The vibrations in the two directions are triggered by the cutting force and both vibrate with the same eigenfrequency. The angle between the two directions defines the phase delay, which leads to an elliptical relative movement between the cutting tool and the workpiece.

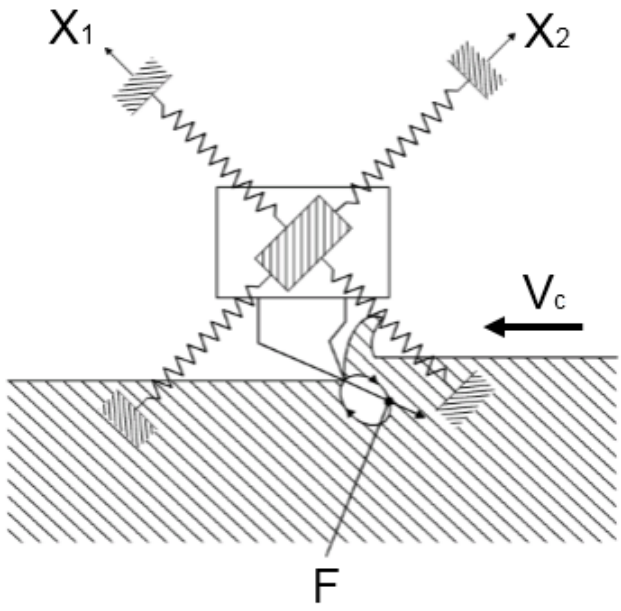

Figure 2.10: Positional coupling of a simplified model [10].

2.4 Chatter Vibration

Chatter vibration leads to severe wear of BTA tool and creates harsh noises during the deep hole drilling process. It could also leave radial chatter marks on the bottom of the produced hole (seen in figure 2.11 [22]). Studies have proven that chatter vibration is related to the self-excited torsional vibration. Many studies are focused on the analysis of chatter vibration and its prevention. Wolfrum et al. [5] derived the motion equation from the idea of finite element by discretizing the boring tool in space and achieved the simulation by using fourth order method on this model. They have successfully simulated the regenerative process and given the relation between the start of chatter vibration and the initial working point. Weinert et al. [14] verified via experimental and finite element methods the influence of the time variant drilling depth on the changing of modal damping, which is responsible for the transition of chatter states regarding different torsional eigenfrequencies during a BTA deep hole drilling process. Theis et al. [21] studied the relation between the machine parameters and the drilling depth where the machining process started to change its dynamic state based on experimental design for BTA deep hole drilling. Weinert et al. [22] proceeded the determination of the transition for chattering in a BTA deep drilling process via Fourier analysis and autocorrelation function (ACF) method based on the experimental measurement of acceleration on the tool head and found that ACF method could predict the chatter vibration earlier than using Fourier analysis. Weinert et al. [23] studied the connection between the parameter of their established statistical model and the parameter of a BTA drilling process. They have observed the different phases including transition from stable state to the beginning of chatter vibration in a dynamic process based on experimental analysis. Dieter [11] created an automatic system consisting of a recognizing component of vibration, a driving component for the determination of coupling location and a controlling component based on a hydraulically controlled Lanchester damper with improved characteristics regarding the pressing element against chatter vibration during a BTA drilling process.

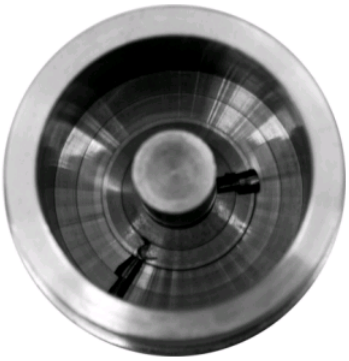

Figure 2.11: Radial chatter marks [22].

2.5 Spiralling

Studies have proven the relation between spiralling and bending eigenfrequencies of a BTA deep hole drilling machine. Spiralling leads to severe deviation of the cross section of the produced hole from standard requirement. The cross section shows a multi-lobe shape and propagates helically along the axis of the bore, which leaves periodic sloping marks on the hole surface (seen in figure 2.12 (a) [22]). An example of a cross section of the bore with 5 lobes is seen in figure 2.12 (b) [2].

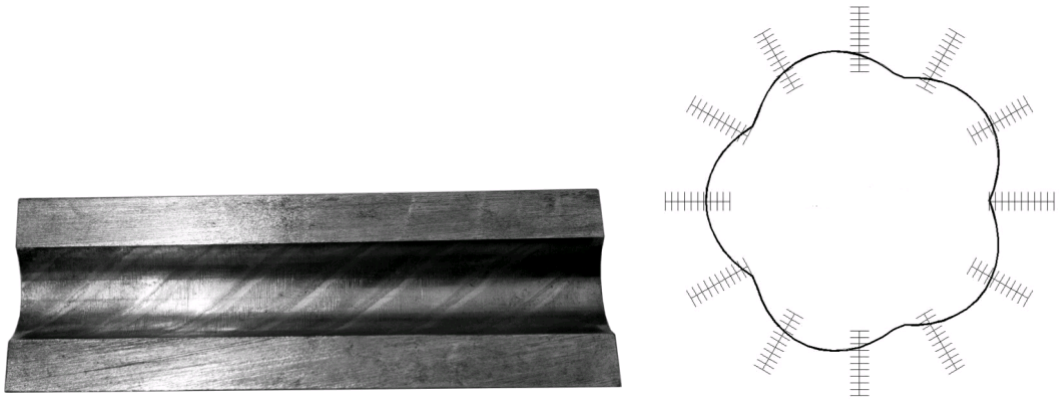

(a) Marks due to spiralling on the inner of a bore.

(b) Sketch of a cross section with 5 lobes.

Figure 2.12: Consequences due to spiralling on produced hole [2, 22].

Many studies have been conducted regarding analysis of spiralling and its prevention. Gessesse et al. [20] revealed two major causes of spiralling via experimental studies with commercial BTA solid tools and proved that the lateral natural frequencies were related to the occurrence of spiralling. Deng et al. [2] carried out a study of roundness error after giving the derivation of analytical expression of the dynamic radial deflection based on Euler beam theory under consideration of radial excitation force. The results were compared with the ones from experiments in different working conditions and showed a good agreement. Sakuma et al. [4] designed a special model to study the action of guide pads during the working process of a BTA machine. They have carried out the calculation of bending eigenfrequencies with consideration of varying relative position between boring bar and stuffing box. Stockert [13] listed the factors regarding the formation of spiralling and proved the significant influence due to angular positions of guide pads on the formation of spiralling and the form of manufactured holes based on the results from experiments. Raabe [19] developed an efficient model for the determination of bending eigenfrequencies to prevent spiralling during a machining process with BTA deep drilling tool via approximation of the simulated results towards the measured solid-borne noise of the drilling tool in real working conditions. Matsuzaki et al. [16] applied the transfer matrix method on the analytical study of the occurrence of rifling marks on the surface of the machined

hole and the results from the eigenanalysis agree well with the ones from experiments. They have proposed an effective countermeasure as well. Szepannek et al. [15] developed a method for the determination of unknown parameters of an established mechanic model. The method was via approximation of frequency responses from the fitted system towards results from measured periodogram data. This method could be used for process control to monitor the appearance of spiralling during a BTA deep hole drilling process. Kong et al. [17] verified the effectiveness of a countermeasure experimentally against vibration during a BTA drilling process via applying magneto-rheological fluid damper with adjustment of excited current and suppression position.

Furthermore, some researches have also been done regarding the determination of eigenproperties of a BTA deep drilling machine with consideration of different coupling conditions. Perng et al. [3] investigated the eigenproperties of a rotating BTA drill shaft based on both Euler and Timoshenko beam theories using Hamiltion's principle for derivation of governing equations and used Galerkin's method as solution tool. The system was in coupling with rotational motion, cutting fluid with constant velocity inside boring bar and axial forces. The validity of the analytical solutions was verified by comparing with results from experiments. Chin et al. [7] gave the theoretical analysis for determination of eigenproperties based on Euler beam theory for BTA deep drilling tool without tool head in coupling with static fluid from inside of the boring bar and also the tool including tool head with coupling of cutting fluid under constant flow velocity inside the boring bar. The results showed a good agreement with the experimental data. Chin et al. [8] gave the theoretical analysis for determination of eigenproperties based on Euler beam theory for BTA deep drilling tool without tool head and without coupling of fluid and also the tool including tool head without coupling of fluid. The results showed a good agreement with the experimental data.

3 Objective and approach

Via finite element (FE) simulation the relation between the development of critical eigenfrequencies of a BTA deep drilling machine and the drilling depth in real operating conditions could be discovered for further developments of countermeasures against self-excited vibrations. A real-time recognition of critical eigenfrequencies is of vital importance both for manual and automatic operations to avoid spiralling and chatter vibration and this can be done with FE simulation efficiently. The corresponding dominant eigenmodes are also available from FE simulation and their usages lie mainly in the determination of critical locations of maximal deflections in the critical eigenmodes for the setup of additional dampers. Operations such as altering the location of Lanchester damper and adjusting the rotational speed could treat results from FE simulation as authentic references. In the automatic damping system of a BTA deep hole drilling machine, the FE simulation could be integrated into the unit of real-time monitoring.

3.1 Predefined assumptions and problem statement

In this thesis, the 3D model of the studied BTA deep hole drilling tool is shown in figure 3.1. In FE simulation, some topological corrections, such as chamfer, irrelevant geometrical complexities which worsen the quality of mesh, empties that can be filled and all possible defeatures, are executed to improve the quality of mesh generation. The topological optimization is considered as acceptable and necessary for further simulation. Within the demand of further studies, some factors are simplified, such as the ineffective lengths of Lanchester damper is set as 20% of the total physical length and the stiffness within the ineffective lengths is neglected. More details are seen in chapter 4.1. The procedure for the study of self-excited torsional and bending vibrations of the BTA deep drilling tool could be summarized as a "pre-stressed modal analysis". The influences of different boundary and working conditions on the modal analysis will be distinguished. The executive strategies are given in chapter 3.2.

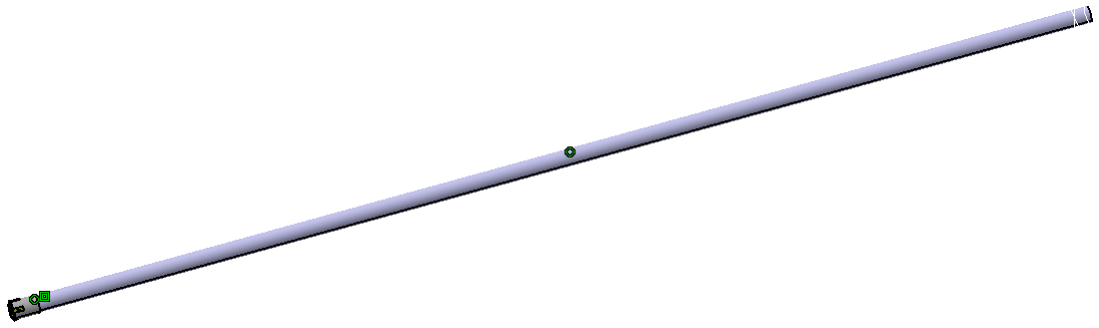

Figure 3.1: 3D model of the BTA deep hole drilling tool.

The detail of the BTA tool head is shown in figure 3.2 (a), (b) and (c) respectively. The constructional difference here comparing to the one in [1] lies in the number of

guide pads and cutters, and their relative positions. This improvement contributes to a higher dynamic stability during deep hole drilling processes.

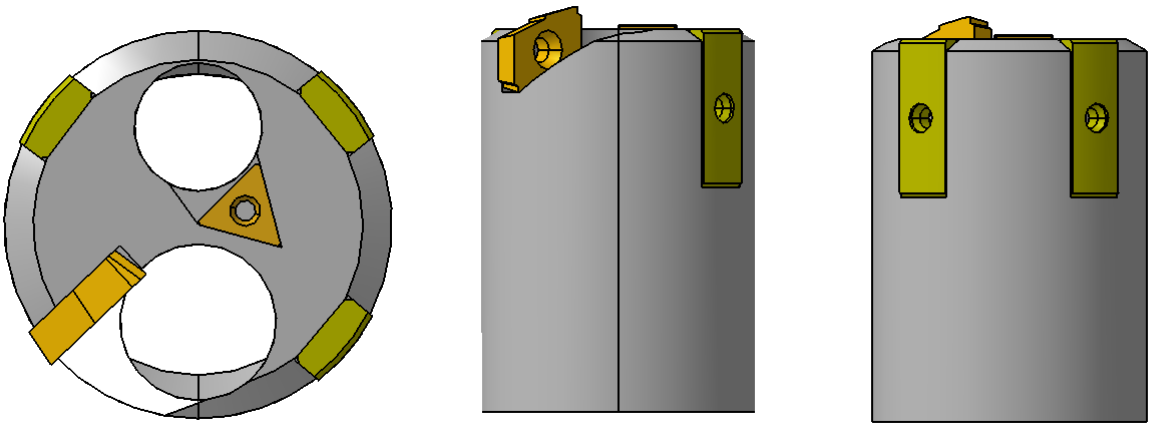

(a) BTA tool head top view. (b) BTA tool head front view. (c) BTA tool head right view.

Figure 3.2: 3D model of BTA tool head in different views.

The data of BTA tool head and boring bar are seen in table 3.1.

Toohead		
External diameter	D_h	69.5 mm
Length	L_h	97 mm
Density	ρ_h	7700 $\frac{kg}{m^3}$
Poisson's ratio	μ_h	0.27
Elastic modulus	E_h	212000 MPa
Boring bar		
External diameter	D_b	62 mm
Internal diameter	d_b	48 mm
Length without thread	L_b	3959 mm
Length of thread	L_{th}	41 mm
Density	ρ_b	7700 $\frac{kg}{m^3}$
Poisson's ratio	μ_b	0.30
Elastic modulus	E_b	210000 MPa
Length of clamp in boring bar chuck	L_{cl}	125 mm
Stuffing Box		
Dual spacing	L_{sb}	90 mm
Speed of cutting fluid	v_c	320 $\frac{Liter}{min}$
Density of cutting fluid	ρ_f	0.867 $\frac{g}{ml}$
Viscosity of cutting fluid	ν_f	15 $\frac{mm^2}{s}$
Lanchester Damper		
Distance to boring bar chuck	L_{bc-ld}	1000 mm
Length	L_{ld}	80 mm
Cutters and Guide Pads		
Elastic modulus	E_{cg}	600000 MPa
Poisson's ratio	μ_{cg}	0.22
Density	ρ_{cg}	14800 $\frac{kg}{m^3}$

Table 3.1: Physical data for BTA setup and input in FE simulation

3.2 Executive strategy

The modal analysis is pre-stressed with coupling conditions from static mechanical module and fluid dynamic module. The setup of the procedure in Ansys Workbench 16.0 is shown in figure 3.3.

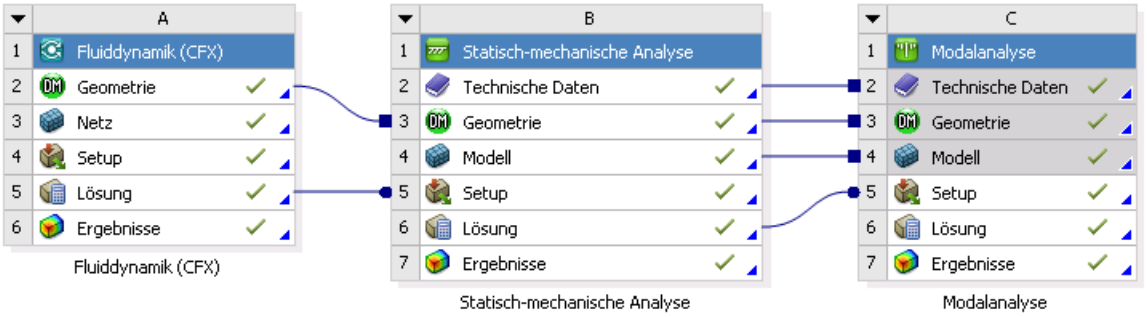

Figure 3.3: Setup for FE simulation in Ansys Workbench.

The process chart in figure 3.4 is given to illustrate the setup and process in Ansys Workbench.

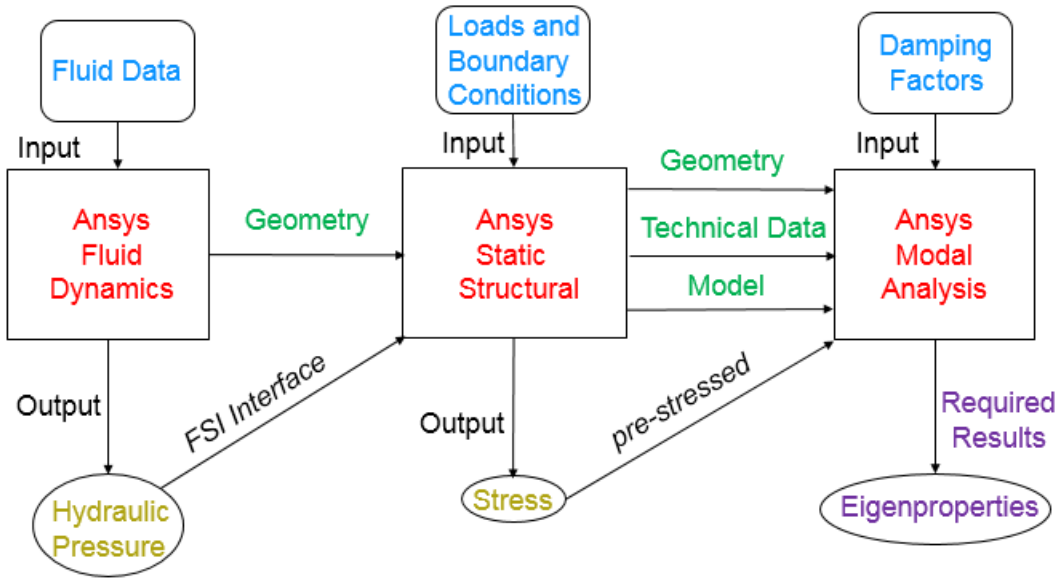

Figure 3.4: Illustration of the setup and process in Ansys Workbench. Blue: input data, red: applied modules in Ansys Workbench, green: shared data, yellow: interim results, purple: required results.

The strategies for the problem solution are as follows.

Phase 1: Determination of essential parameters for FE simulation

- Summarizing essential parameters for FE simulation.
- Parameter study of boundary and working conditions.

Phase 2: FE Simulation

- Pre-processing for mechanical domain and fluid domain: topological optimization, mesh configuration and convergence study
- Simulation in different coupling conditions and study of their influences.
- Determination of the relation between critical eigenproperties and drilling depth for different setups of the Lanchester damper.
- Post-processing: Interpretation of the results and countermeasures recommendation.

4 Implementation of FE Simulation

4.1 Analysis of boundary and working conditions

In order to gain the results in real working and boundary conditions, the influences from the stuffing box, the Lanchester damper and the workpiece on the BTA tool are considered. In [14, 18], the torsional damping and elastic supporting effects from the stuffing box, the elastic supporting effect from the Lanchester damper and the workpiece, the material damping factors of the boring bar are obtained with experimental and numerical methods. According to [18], an experimental modal analysis could be designed as follows.

First of all, the trigger and measurement in the modal experiment for torsional vibration could be executed both tangentially with flange on the boring bar. The Lanchester damper is not applied during the experiment in order to obtain clear torsional responses. Furthermore, the experiment for bending vibration is only supposed to focus on the lateral measurement. The trigger via hammer could be executed with consideration of nodal nodes. The potential nodal nodes are known for zero displacement in vibration and are supposed to appear at the supporting areas in stuffing box and Lanchester damper plus the equidistant locations between the supports. The locations of sensors for the measurement of lateral acceleration should have also taken the potential nodal nodes into consideration. The plan for the experiments should take the drilling depth as a critical influential factor into consideration. For the determination of the first three torsional plus first five bending eigenfrequencies, a mean valued frequency response of 10 repeated measurements at each drilling depth could be computed for the final determination of eigenfrequencies. The effective length of the Lanchester damper is supposed to be shorter than its physical length according to [18, 29]. The details of the Lanchester damper and stuffing box are shown in figure 4.1 (a) and (b). In figure 4.1 (a), $L_{LD,left}$ and $L_{LD,right}$ refer to the ineffective lengths in the physical length of Lanchester damper L_{LD} due to wear and error from production respectively. $L_{LD,left}$ and $L_{LD,right}$ are assumed to be 10% of L_{LD} respectively. In figure 4.1 (b), unknown torsional damping effects from stuffing box to boring bar are brought at the two contact locations.

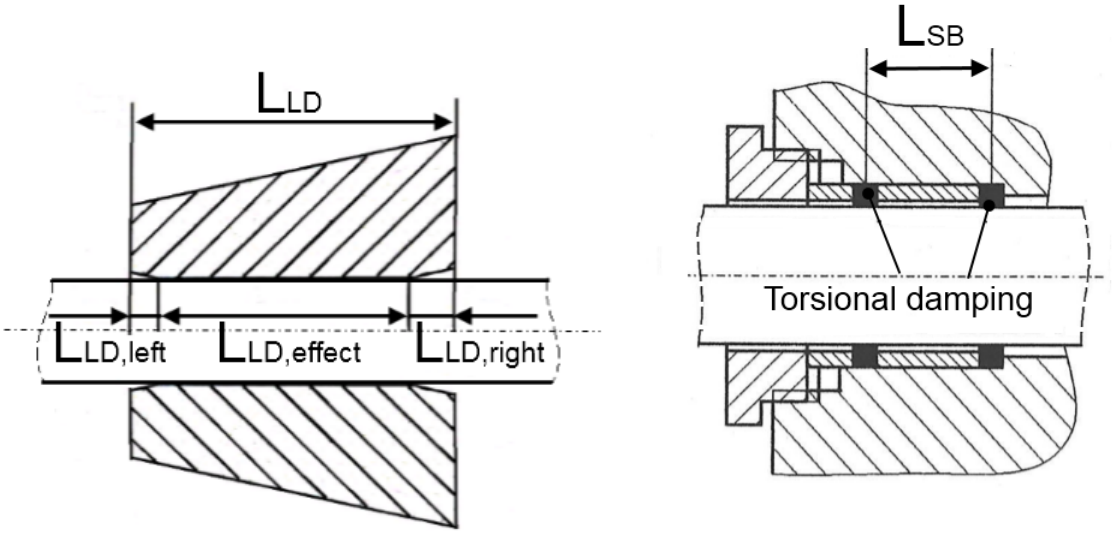

(a) Lanchester damper.

(b) Stuffing box.

Figure 4.1: Models of Lanchester damper and stuffing box [18].

The setup of the BTA deep drilling tool is shown in figure 4.2. Label 1, 2, 3, 4 and 5 refer to the Lanchester damper, boring bar, stuffing box, workpiece and BTA tool head respectively. $D_{SB,1}$, $D_{SB,2}$ and D_{LD} refer to the distances between the clamping end and the two contacting locations of stuffing box plus the Lanchester damper respectively, where $D_{SB,1}$ and $D_{SB,2}$ depend on the drilling depth.

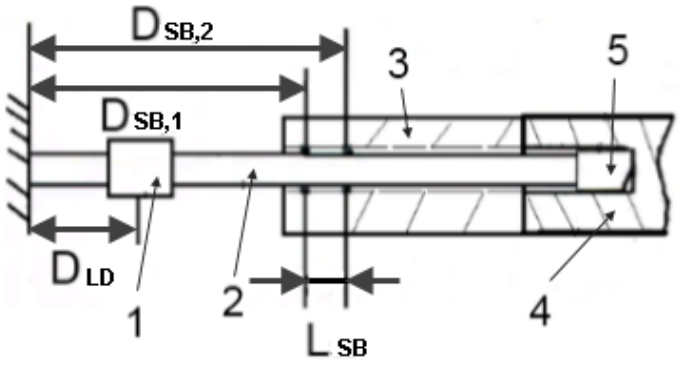

Figure 4.2: Sketch of the setup of BTA tool. 1: Lanchester damper, 2: Boring bar, 3: Stuffing box, 4: Workpiece, 5: BTA tool head.

A common tool of the evaluation of measured eigenfrequencies is via ME Scope and the determination of the elastic stiffness at the contacting area between the Lanchester damper and the boring bar k_{LD} and the elastic stiffness at the contacting areas

between the stuffing box and the boring bar $k_{SB,1,2}$ could be succeeded with experimental measurements. However the elastic stiffness between the workpiece and the BTA tool head k_W was not able to measure due to the working condition. Although many researches are done with ideal rigid support or extremly large stiffness for k_W (seen in [14, 19]), according to [18] the stiffness is supposed to be limited and varies as the drilling depth changes. Furthermore, regarding the unknown torsional damping factors from contact locations between stuffing box and boring bar $c_{SB,1}$, $c_{SB,2}$ plus the material proportional damping factors α and β, numerical studies are done in many researches, such as by applying Nelder-Mead Simplex method according to [30]. The strategy is based on monitoring the SSE (short for "Sum of Squared Errors"), which is obtained by comparing measured and calculated eigenfrequencies via iteration of input regarding unknown factors [31]. Based on the mechanical model in [18], the method is to evaluate the eigenproperty of the system of equations, which are derived from the finitely discrete model. The system of equations is given as (4.1).

$$M\ddot{x} + C\dot{x} + Kx = 0 \tag{4.1}$$

where C, M and K represent the damping, mass and stiffness matrix respectively. x is the vector that contains all degrees of freedom of the discrete model.

The approach for this system is conventionally using (4.2) for the solving procedure, where X, j, ω and t represent the norm of the vector, imaginary unit, eigenvalue of the system of equations and quantity of time respectively.

$$x = Xe^{j\omega t} \tag{4.2}$$

Eventually for the non-trivial solution of the system, which is e.g. undamped, the equation (4.3) must hold.

$$det(K - \omega^2 M) = 0 \tag{4.3}$$

Furthermore, the proportional material damping model (4.4) is used to simulate the system damping, where α and β are the material damping factors.

$$C = \alpha M + \beta K \tag{4.4}$$

The aim is to minimize the value of function h, which is defined in (4.5)

$$h = \sum_{i=1}^{n} (f_{exp,i} - f_{num,i})^2 \tag{4.5}$$

f_{exp} and f_{num} are the experimental and numerical values of eigenfrequencies respectively. n is the number of treated eigenfrequencies. The values of the unknown factors in this thesis are rationally assumed based on the study in [18]. Numerical programs for the determination of material and torsional damping ratios are written in Matlab for the support of further study with experimental measurements. The programs and the input values of determined factors for FE simulation are seen in Appendices.

4.2 Numerical study of damping effects in modal analysis

In this section, the influence of damping factors on the determination of eigenfrequencies is studied. The purpose is to evaluate the experimental and numerical cost for the determination of torsional and material damping factors by comparing the discrepancy of eigenfrequencies with and without damping effects. As the damping effects will not be considered in static structural module, the study is only applied for modal analysis module. A FE simulation using beam element is carried out. One line body is modeled with a defined cross section, which corresponds to the cross section of boring bar. The line body is meshed with beam 188 element, which is based on Timoshenko beam theory. Comparing to 2D and 3D element, the beam element reduces computational effort while maintains satisfied results in modal analysis. The line body is meshed with 2000 elements and simply clamped at one end without other conditions. The only variable is damping effect. The simulation is conducted both for damping free and damping attached cases. For damping attached cases a further distinction is among torsional damping only, material damping only and two damping effects together. The setting of torsional spring is given in figure 4.3.

The relative errors regarding torsional and bending eigenfrequencies are shown in table 4.1 and 4.2. T-N, M-N, T+M-N refer to the comparison between the natural eigenfrequencies and the damped eigenfrequencies in simulations with torsional damping, material proportional damping and both at the same time respectively.

Order of torsional Ef	rel.error T-N	rel.error M-N	rel.error T+M-N
1	-0.01%	-0.08%	-0.09%
2	-0.00%	-0.03%	-0.03%
3	-0.00%	-0.01%	-0.01%

Table 4.1: Relative error for torsional eigenfrequencies with different damping effects.

Order of bending Ef	rel.error T-N	rel.error M-N	rel.error T+M-N
1	0.00%	-7.00%	-7.00%
2	0.00%	-0.87%	-0.87%
3	0.00%	-0.23%	-0.23%
4	0.00%	-0.09%	-0.09%

Table 4.2: Relative error for bending eigenfrequencies with different damping effects.

In table 4.1 it can be seen that both torsional and material proportional damping effects reduce the torsional eigenfrequencies. However, the influence for higher order

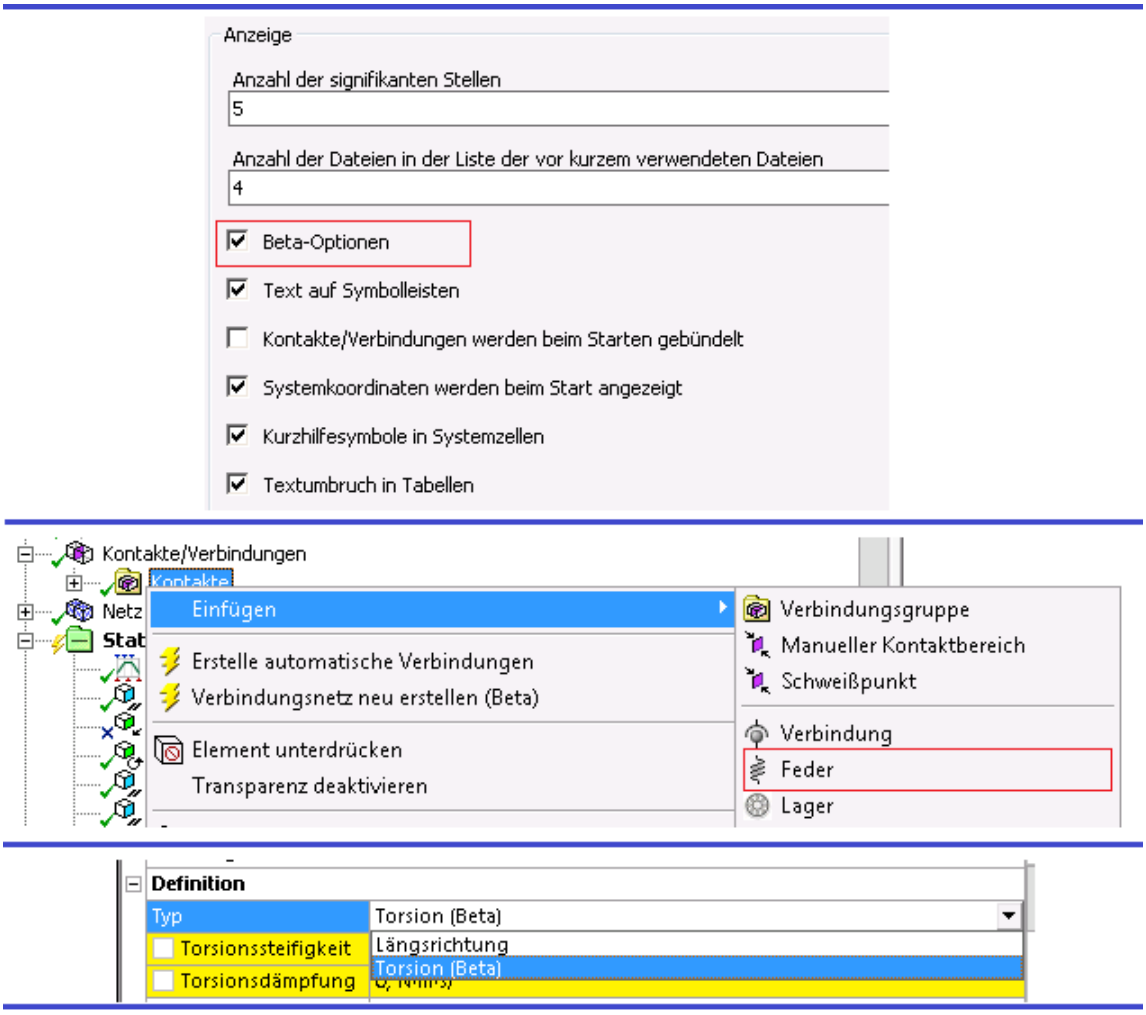

Figure 4.3: Setting for torsional damping spring in Ansys Workbench 16.0.

torsional eigenfrequencies is decreasing. A combination from both effects leads to larger damping effect, but the effect is not simply added from both. For the same order of torsional eigenfrequency, the torsional damping is less effective comparing to material damping.

In table 4.2 it can be seen that only material proportional damping reduces the bending eigenfrequencies and as the order of eigenfrequency increases, the damping effect is decreasing. The original natural eigenfrequency was around 3 Hz and this was not shown in the results in damped simulation. One reasonable explanation is that the damping effect is big enough to prevent the triggering of resonance at this frequency. This can be seen that the material damping reduces the 1st order eigenfrequency for more than 7%. After that, the damping effect drops monotonically. Therefore, the 3 Hz natural eigenfrequency could be damped to almost 0 Hz, which represents rigid body case.

All in all, the torsional damping effect from stuffing box contributes only a very limited effect to torsional eigenvibration, while material proportional damping influences both torsional and bending eigenvibrations and the effect is not supposed to be neglected. Therefore, for further FE simulation, due to the limited damping effect and also because the torsional damping function is currently still in beta features in Ansys WB 16.0, the effect of material damping is to be included while the torsional damping effect is to be dropped.

4.3 Convergence study in static structural mechanics

Every FE simulation requires around 80% of the total working time for pre-processing because the quality of the generated mesh determines the usefulness of the result significantly. Therefore a convergence study to determine a proper mesh is conducted before the simulation starts.

The convergence study is mainly focused on the boring bar, because firstly, in [14] the FE simulation was conducted both for the model with BTA tool head and the model without BTA tool head and the results showed an acceptable discrepancy. The computational effort for the latter model is however much smaller. Furthermore, due to the high length to diameter ratio, the boring bar is simulated with shell element and the connection between the BTA tool head and the boring bar is set as one MPC (Multi-Point-Constraint) connection in Ansys Workbench. So the meshes in tool head and boring bar are not necessarily consistent. Last but not least, the mapping of results from fluid domain requires high quality of mesh in structure domain and the main interface is in boring bar instead of tool head.

Due to the thin shell model of the boring bar, one layer shell element with element type shell 181 is created in Ansys Workbench. There are two variables that are set to change the mesh. One is the number of division on the perimeter of the circular cross section (note as NoD_C) and the other one is the number of division in the longitudinal direction (note as NoD_L). Figure 4.4 shows the thin shell model of the boring bar and figure 4.5 shows the local mesh controls for the specified discretization.

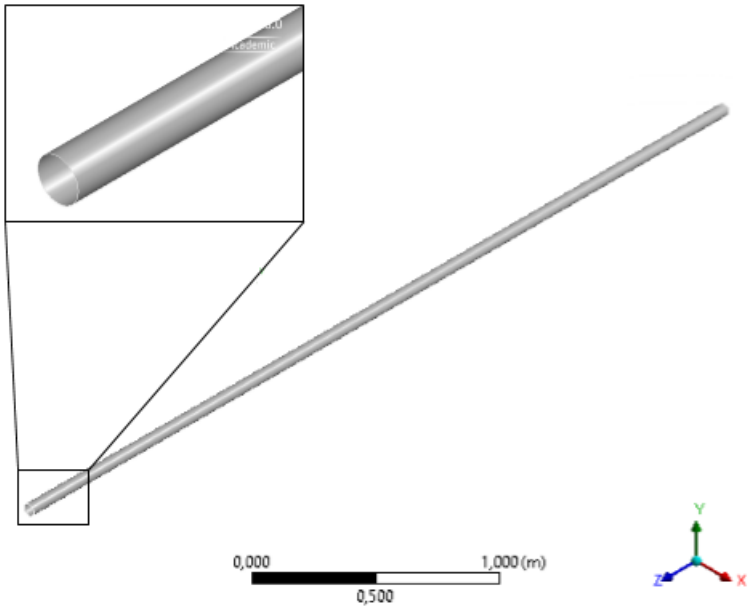

Figure 4.4: Thin shell model of the BTA boring bar.

Although a pre-stressed modal analysis is needed, the stress field in fluid domain

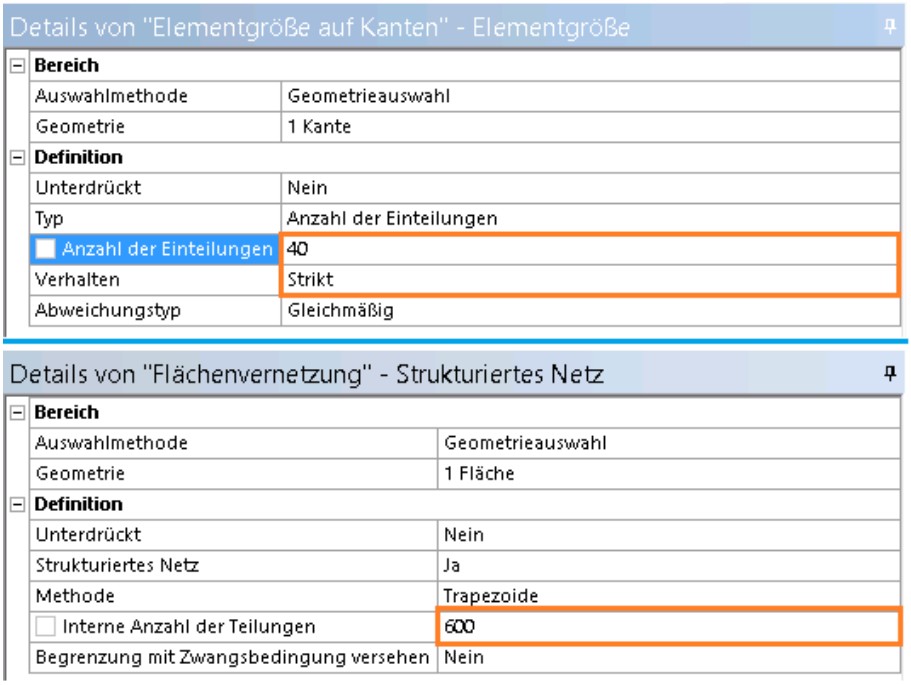

Figure 4.5: Local mesh control settings for specified discretization.

and solid domain are to be determined first because the stress will be applied in the modal analysis later on. Therefore the convergence study here runs for a simple static structural analysis, in which stress is defined as output. The reference for error determination is via monitoring the varying relative error till it reaches one percent, which is set as the termination criterion. The boring bar is clamped at one end while the other end is applied with a force in lateral direction. The observed stress is the von Mises stress at a fixed monitor point on the boring bar.

Firstly, the changes of mesh quality as the two variable change are observed. The tendency of the change is obviously small for available criteria in Ansys static structural module except for aspect ratio. These can be seen in table 4.3 with two randomly picked combinations. This is due to the fact that meshing method for surface is inserted in local mesh control to produce quadrilateral mesh in the regular cylindrical geometry. So the varying quality criterion is the aspect ratio only and according to the user guide in Hypermesh, the acceptable aspect ratio for simulation regarding stress field is till 1:3. Although the best ratio is 1:1, this leads however to high density of mesh and the computational effort rises. This is possibly not seen in the simple loading case here, but will be seen in the analysis with larger computational burden due to the complex geometry of tool head and the mapping of the result from fluid domain later on. Therefore, the 1:3 aspect ratio is chosen for the following phase as the minimal criterion.

Criteria	NoD_L=100, NoD_C=10	NoD_L=120, NoD_C=60	Optimum
Jacobian Ratio	1.0023	1.002	1
Warping Factor	0	0	0
Parallel Deviation	max. 0.08	max. 0.07	0
Maximum Corner Angle	90 deg	90 deg	90 deg
Skewness	0	0	0
Orthogonal Quality	1	1	1
Aspect Ratio	max. 1:2.87	max. 1:14.27	1:1

Table 4.3: Change of mesh quality in two random combinations.

The approach for convergence study is that based on the chosen aspect ratio, the best choice of NoD_L regarding different NoD_C are determined and their corresponding computational relative errors are calculated until the criterion is reached. The progress is shown in table 4.4 and 4.5

Trial	NoD_C	opt. NoD_L	max. Aspect ratio	Relative error in %
1	10	100	1 : 2.87	–
2	20	200	1 : 2.85	-2.04
3	30	300	1 : 2.86	-1.56
4	40	400	1 : 2.86	1.74
5	50	500	1 : 2.86	1.69
6	60	600	1 : 2.86	1.69
7	70	700	1 : 2.86	1.12
8	80	800	1 : 2.86	1.09
9	90	900	1 : 2.86	0.78

Table 4.4: Global convergence study regarding stress field.

Trial	Set 1	Set 2	Rel. error in %
1	10×90	10×100	-0.24
2	20×190	20×200	0.07
3	30×290	30×300	0.05
4	40×390	40×400	0.23
5	50×490	50×500	0.18
6	60×590	60×600	0.14
7	70×690	70×700	0.11
8	80×790	80×800	0.09
9	90×890	90×900	0.08

Table 4.5: Transversal convergence study regarding stress field.

Beside the convergence near the combination around 90 × 900, two intersections between the convergence history and criterion are also captured in table 4.4 and 4.5 for the combination around 30 × 300 and 40 × 400. To disambiguate this seeming convergence point, the convergence study regarding deformation is conducted as a reference with analytical solution based on Timoshenko beam theory. The reason is that the requirement of aspect ratio for simulation of deformation is according to Hypermesh user manual around 1:5, which is lower than that for stress field. Therefore with the same model, the mesh for stress field study is denser than the one for deformation. The convergence history for deformation is shown in table 4.6.

Trial	NoD_C	opt. NoD_L	max. Aspect ratio	Relative error in %
1	10	60	1 : 4.88	9.58
2	20	120	1 : 4.74	2.93
3	30	180	1 : 4.76	1.74
4	40	230	1 : 4.97	1.33
5	50	290	1 : 4.92	1.15
6	60	350	1 : 4.90	1.04
7	70	420	1 : 4.76	0.94

Table 4.6: Convergence study regarding deformation.

Here, to reach the convergence criterion of 1%, the combination is recorded as 70×420,

which equals 29400 shell elements, while the seeming convergence point shows around 40×400, which represents 16000 shell elements. Therefore the seeming convergence point is safely exclusive. The reason for this ambiguity is possibly due to the fact that the error in the simulation of stress field is one order higher than the one in deformation, as the latter one is for the calculation of stress field further accumulated. The sensitivity of error accumulation in stress field is one order higher than the one in simulation of deformation and therefore a larger fluctuation could be observed in convergence study of stress field, but possibly not in the one of deformation. The convergence histories for stress field and deformation are shown in figure 4.6.

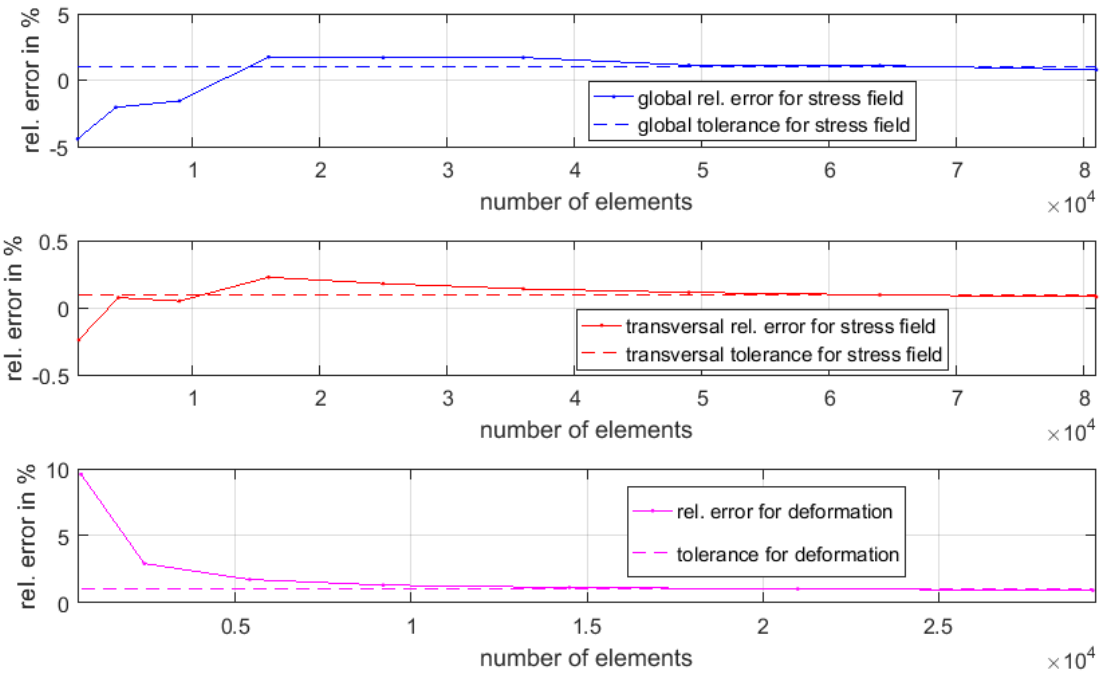

Figure 4.6: Convergence study for stress field and deformation in static structural module.

With the satisfaction of the criterion for aspect ratio, the numbers of division at the perimeter on the cross section and the one in longitudinal direction are set as 90 and 900 respectively for the lowest computational effort. For automatic adjustment in default settings in FE simulation later on, as long as this minimal criterion is satisfied, the result is considered as reliable for the calculation and transfer of stress.

As mentioned before, the meshing process for the BTA tool head is not straightforward comparing to the boring bar due to its complex geometry. Beside the advanced curvature function in global setting, local mesh refinement and mesh size control are applied to improve its mesh quality. Furthermore, a comparison between tetrahedral

and hexahedral mesh regarding the critical mesh criterion, skewness, shows tetrahedral mesh fits the complex geometries better than hexahedral mesh. Therefore, a local mesh method using tetrahedral meshing method is applied for the tool head to limit the maximal skewness within the acceptable range according to Ansys user manual.

4.4 Introduction to Fluid-Structure Interaction (FSI)

FSI is short for Fluid-Structure Interaction and it represents a kind of problem requiring knowledge from multidisciplinary fields. In this thesis the BTA tool interacts with the coolant flow during the deep hole drilling process. The vibration of the solid structure will not be stopped but obviously resisted by the surrounding cutting flow and this effect will be studied to determine the influence on the eigenfrequencies of BTA tool. An illustration regarding FSI is shown in figure 4.7. The fluid domain is colored blue and the solid domain is colored black. The broken red line between two domains represents the interface, where data could transfer between two domains. The governing equations in two domains are according to [24, 25, 27] given as follows.

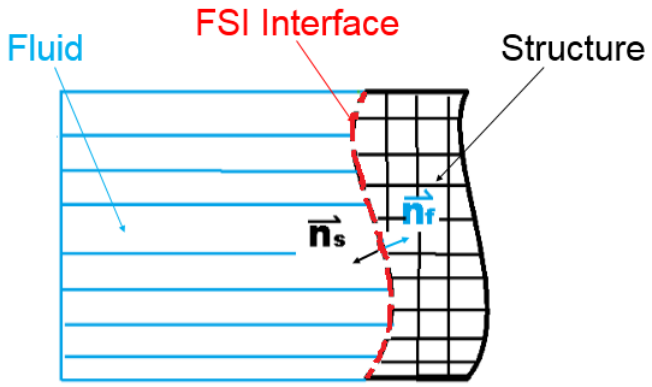

Figure 4.7: Illustration of Fluid-Structure Interaction.

$$\frac{\partial \rho_f}{\partial t} + \nabla \cdot (\rho_f \vec{v_f}) = 0 \tag{4.6}$$

$$\rho_f \frac{D\vec{v_f}}{Dt} - \nabla \cdot \sigma_f = \vec{f_f} \tag{4.7}$$

$$\rho_s \frac{\partial \vec{v_s}}{\partial t} - \nabla \cdot \sigma_s = \vec{f_s} \tag{4.8}$$

Here the subscripts f and s represent the fluid and solid domain respectively. m, ρ, v, σ and f correspond to the quantity of mass, density, velocity, stress tensor and body force respectively. The equations (4.6) and (4.7) are mass conservation equation and Navier-Stokes equation in fluid dynamics respectively while the equation (4.8) is the momentum conversation equation in solid mechanics. In the FSI simulation later on, the mass of fluid domain doesn't have to be added to the solid structure to capture the conventionally known "resisting effect". The reason is that in equation (4.7), σ_f includes pressure effect and the mass conservation equation (4.6) holds for the whole fluid domain, so there is no need to add mass to structure after transferring the pressure at FSI interface. The coupling conditions at FSI interface are given in

(4.9a) and (4.9b) [24, 25, 27]. Here u and $\vec{n}$ represent the displacement and normal vector at FSI interface. The directions of normal vectors are shown in figure 4.7.

$$\vec{u_f} = \vec{u_s}, \tag{4.9a}$$

$$\vec{n_f} \cdot \sigma_f = \vec{n_s} \cdot \sigma_s, \tag{4.9b}$$

The condition (4.9a) represents the equal displacement at the FSI interface and the condition (4.9b) represents the equilibrium of stress. In the configuration in FE simulation, the definition of the interface is important because the definition of "wall" in CFD depends on the viscosity of cutting fluid. In case the fluid model is non-viscous, the coupling condition (4.9a) has to be modified so that the relative movement in tangential direction along interface is not prohibited anymore although the movement in normal direction remains banned [24].

There are two different approaches for solving FSI problems. The first approach is called the monolithic approach, which solves the governing equations in both domains simultaneously and the second approach is called the partitioned approach, which solves the equations separately (seen in [27, 28]). For the FE simulation in Ansys Workbench 16.0, the partitioned approach is applied and one-way FSI is needed in this thesis without large geometric deformation. However, especially when the deformation at interface is large comparing to the geometry of structure, one challenge in FSI known as moving mesh occurs at interface if partitioned approach is applied, as this approach requires conforming mesh, which means the mesh generation must comply the deformed geometric boundary. The cause of moving mesh is that the load transfer from fluid to structure via interface will cause linear or non-linear dynamic response in structure. This will in return lead to deformation at interface and the displacement there will be transferred back to fluid domain, which is to be interpolated and conform the deformation at interface. Therefore the mesh at interface must be regenerated to conform the geometric change. Although some tools are available in CFD programs, extra programming regarding mesh generation is often required.

4.5 Convergence study in fluid dynamics

The fluid calculation is executed in Ansys CFX module. The fluid domain is shown in figure 4.8. The green marks A and B represent the inlet and outlet of the coolant flow respectively.

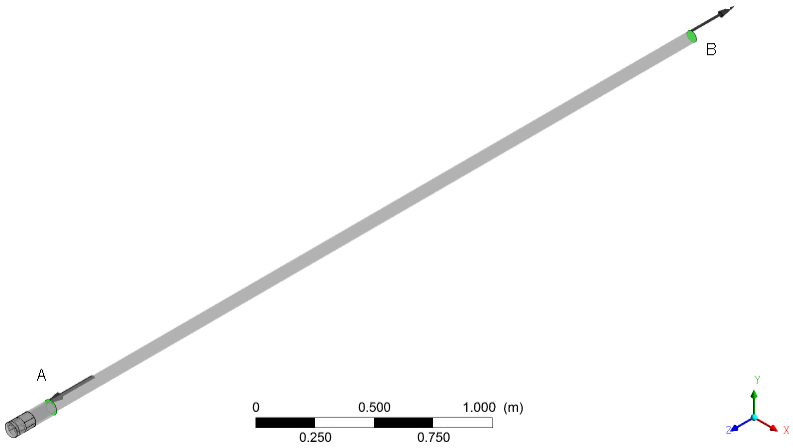

Figure 4.8: Illustration of fluid domain in Ansys CFX.

The details of inlet A and outlet B are shown in figure 4.9 (a) and (b).

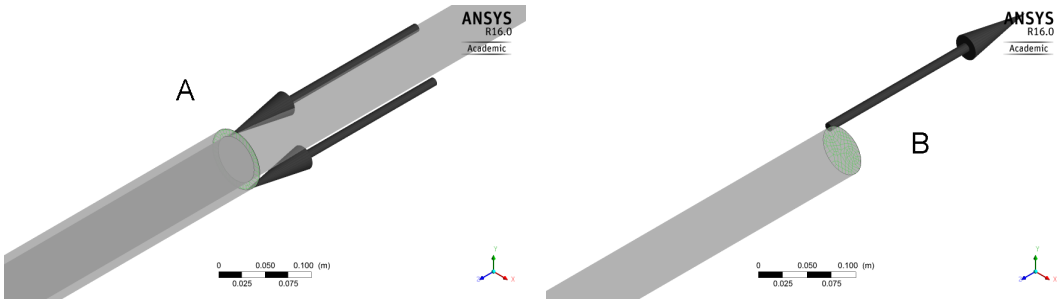

(a) A. Inlet in fluid domain.

(b) B. Outlet in fluid domain.

Figure 4.9: Inlet and outlet in fluid domain.

The simulation is defined as a laminar flow as the Reynold number doesn't reach the range for turbulent flow. Similarly, a convergence study is carried out. The dominant criteria in CFX are the minimal orthogonal angle (in degree), the maximal expansion factor and the maximal aspect ratio. The monitored quantities are the default RMS U-Moment, RMS V-Moment, RMS W-Moment and RMS P-Mass, where RMS refers to "Root Mean Square". The termination criterion is set as 1×10^{-4} for all four quantities. The results are shown in table 4.7.

Element size in mm	3	3	3	2	1	Ideal Range
Method	Hex	Tet	Auto	Auto	Auto	-
Min. Orthogonal Angle	3.4	30.8	57.2	63.3	70.2	> 20
Max. Expansion Factor	6220	153	12	4	2	< 20
Max. Aspect Ratio	106	6	5	3	2	< 100
RMS U-Moment $\times 10^{-4}$	40	4.3	3.7	1.6	0.7	< 1
RMS V-Moment $\times 10^{-4}$	50	3.7	3.8	1.8	0.9	< 1
RMS W-Moment $\times 10^{-4}$	60	14	16	4.9	0.8	< 1
RMS P-Mass $\times 10^{-4}$	70	0.2	0.11	0.07	0.03	< 1

Table 4.7: Convergence study in fluid domain.

The simulation converges reluctantly with 1 mm size of element with 94 iterations, while the computational effort is already extremely high. An optimization of the original model is recommended for the study in the future.

The hydraulic pressure, which is calculated in Ansys CFX, will be transferred to the static mechanic module. The definition of the interface for the transmission of the data on the mechanic model, the illustration of the hydraulic pressure on the cross section of the thin shell boring bar and one example of the stress field on the interface of the mechanic model at the drilling depth of 250 mm after mapping and interpolation of the pressure in accordance with the meshes from the two coupled fields are given in figure 4.10, 4.11 and 4.12 respectively. According to Bernoulli's principle, the hydraulic pressure is supposed to be larger when the flow velocity is smaller. In the simulation, minimal pressure is observed around the tool head, when the cross section of the flow is small, which leads to high velocity. In the inner of the boring bar, the cross section is large and the pressure there is the largest. Furthermore, as the hydraulic pressure is added on the shell element, comparing to the solid element, where two interfaces are seperated, the pressure on the shell element is supposed to be higher than the experimental data, but the results of the simulation satisfies with both types of elements.

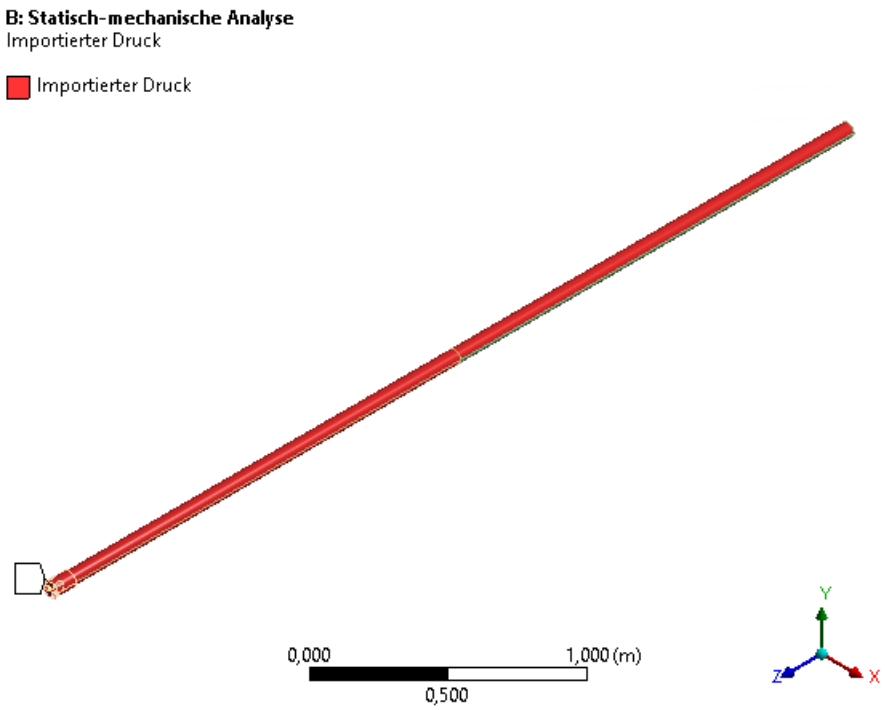

Figure 4.10: Definition of interface for data transmission (selected surfaces).

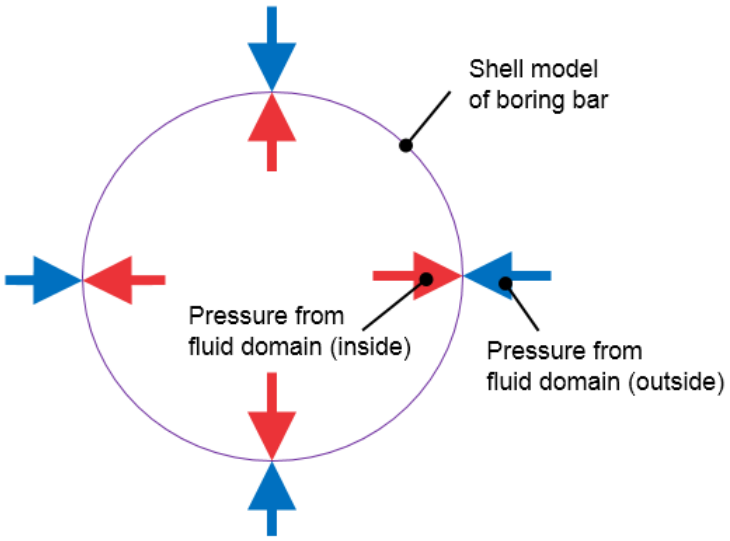

Figure 4.11: Hydraulic pressure on the thin shell model of the boring bar (cross section).

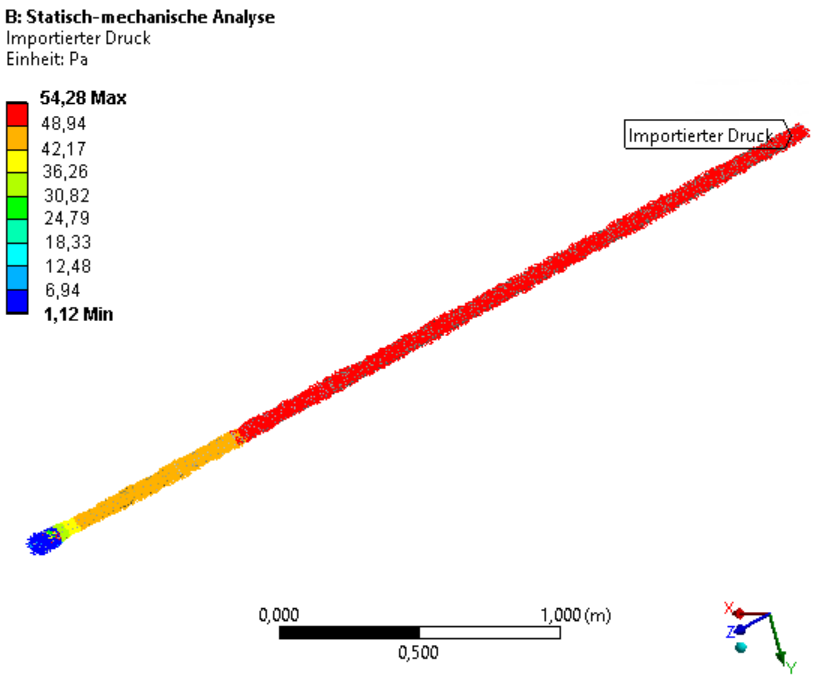

Figure 4.12: Distribution of the pressure field on the interface.

5 Results and Discussion

5.1 Rotor dynamics analysis

To fulfill the completeness of this thesis, a rotor dynamics analysis was carried out at first. The simulations were both for the setup with a fixed position of the Lanchester damper on the boring bar and the setup with a varying position of the Lanchester damper as the drilling depth changed. The results were recorded for the simulations in the drilling depth of 250 mm, 500 mm, 750 mm and 1000 mm respectively. The model was considered as non-loaded and the elastic supports at the clamping end, contact zones of stuffing box and Lanchester damper were simulated with COMBI214 bearing elements respectively without considering rotational damping effect. The range of monitored rotational speed was set up to 2000 rad/s. The Campbell diagrams are shown in figure 5.1 to 5.8.

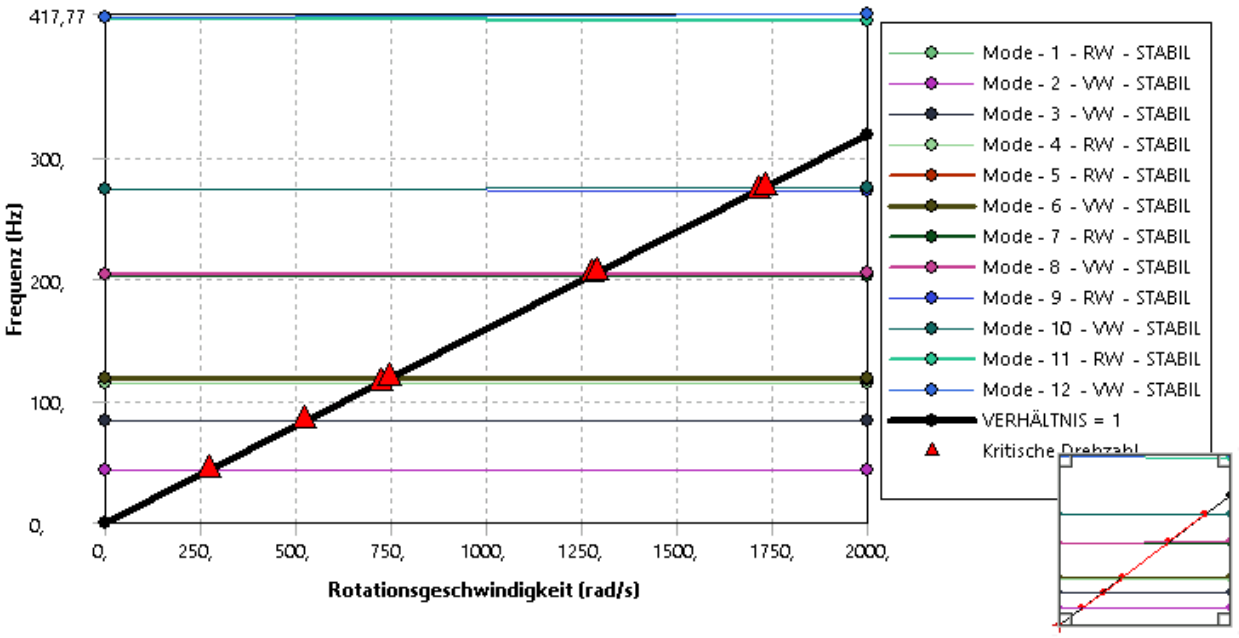

Figure 5.1: Campbell diagram at the drilling depth of 250 mm with fixed Lanchester damper.

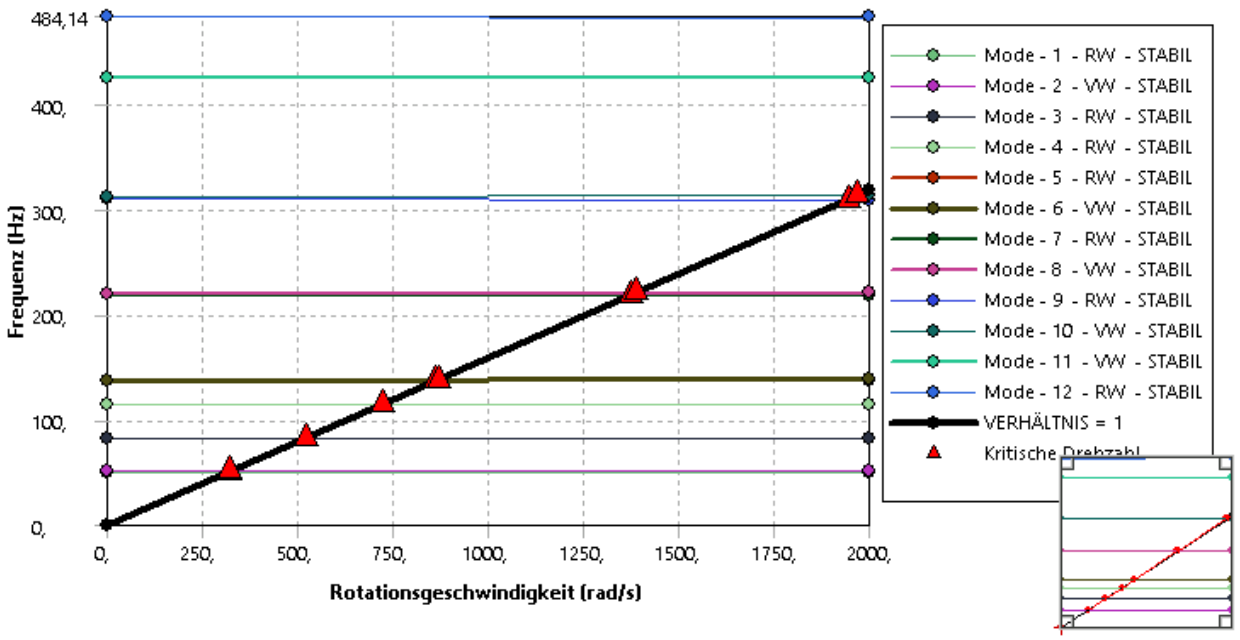

Figure 5.2: Campbell diagram at the drilling depth of 500 mm with fixed Lanchester damper.

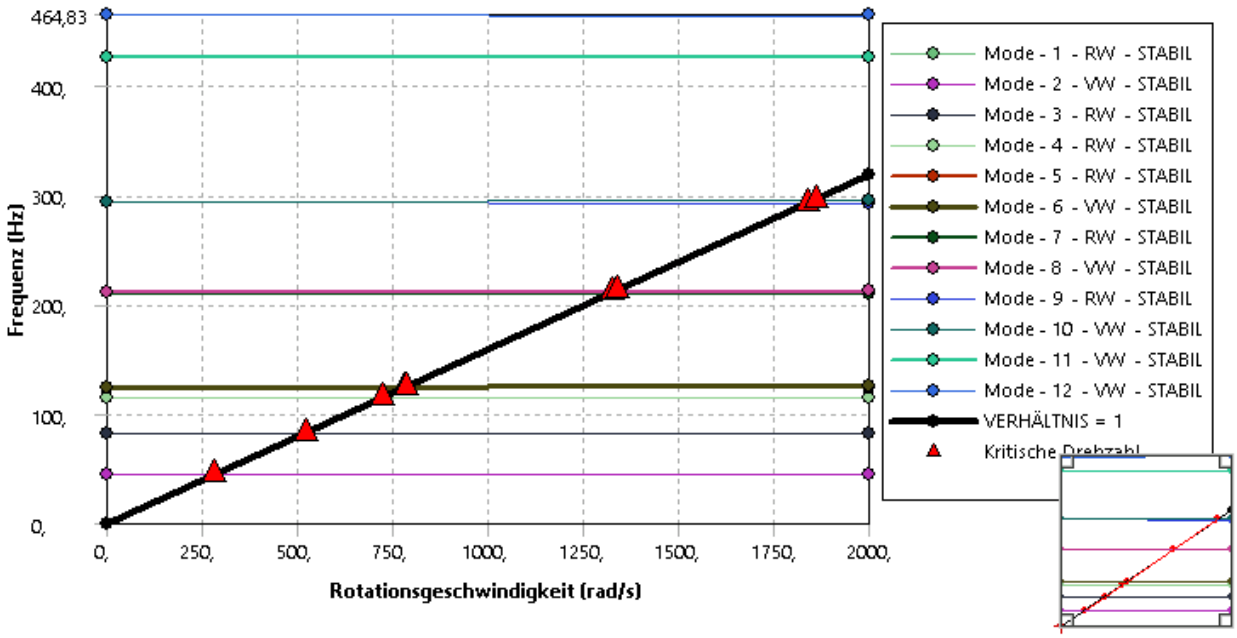

Figure 5.3: Campbell diagram at the drilling depth of 750 mm with fixed Lanchester damper.

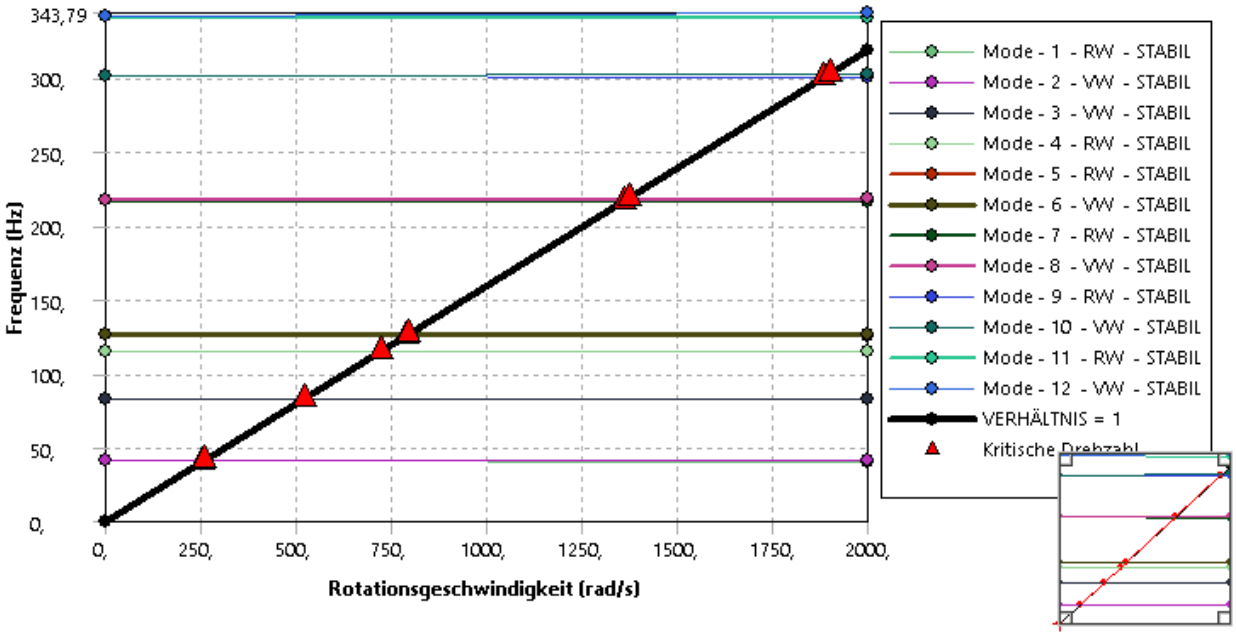

Figure 5.4: Campbell diagram at the drilling depth of 1000 mm with fixed Lanchester damper.

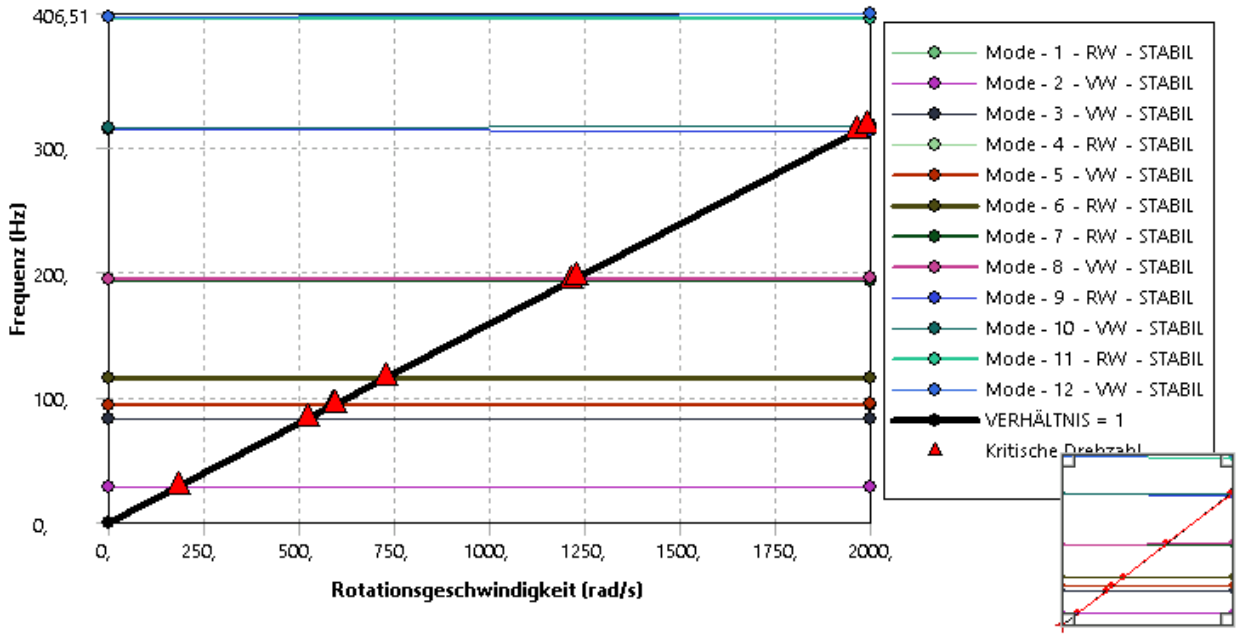

Figure 5.5: Campbell diagram at the drilling depth of 250 mm with moving Lanchester damper.

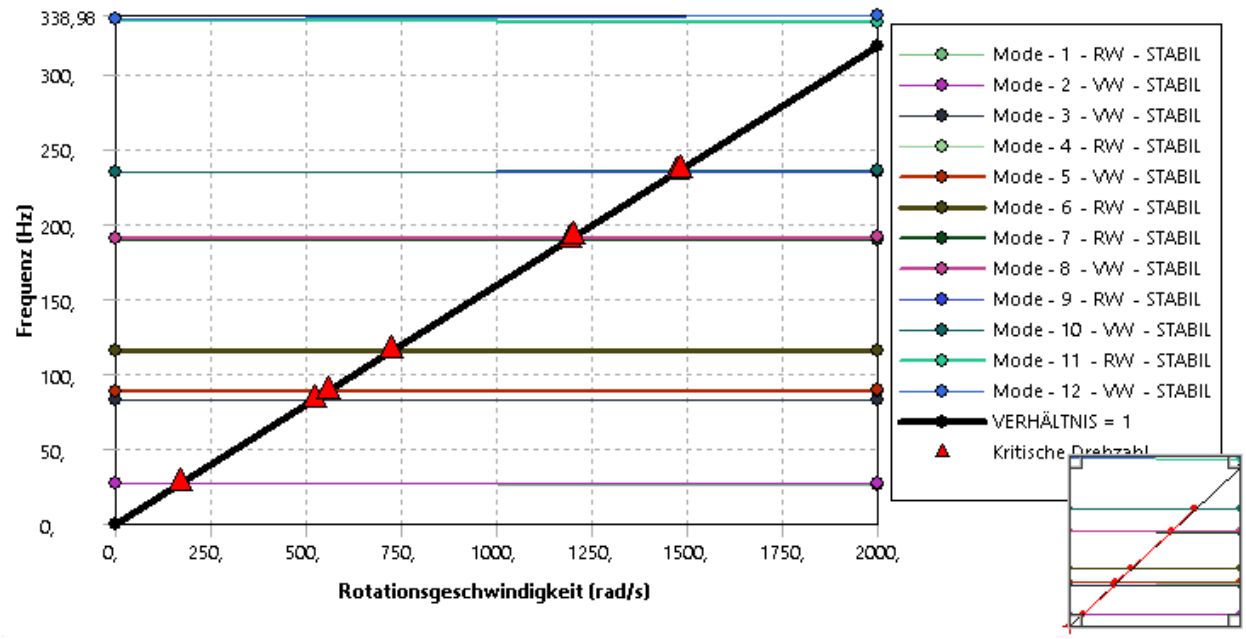

Figure 5.6: Campbell diagram at the drilling depth of 500 mm with moving Lanchester damper.

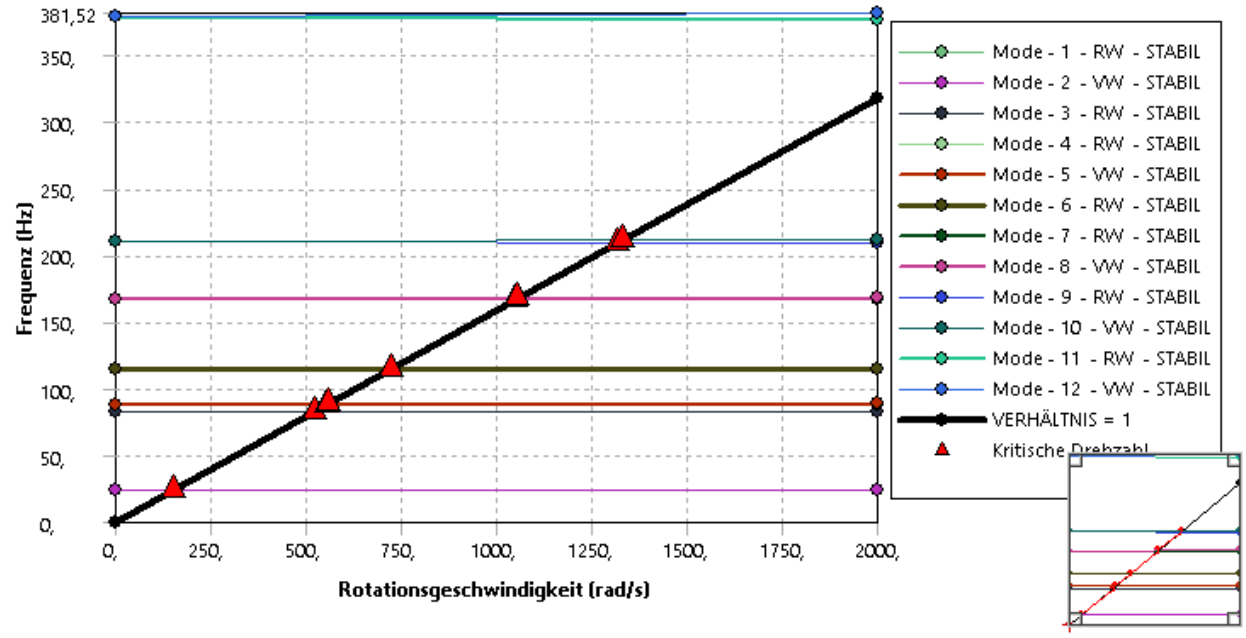

Figure 5.7: Campbell diagram at the drilling depth of 750 mm with moving Lanchester damper.

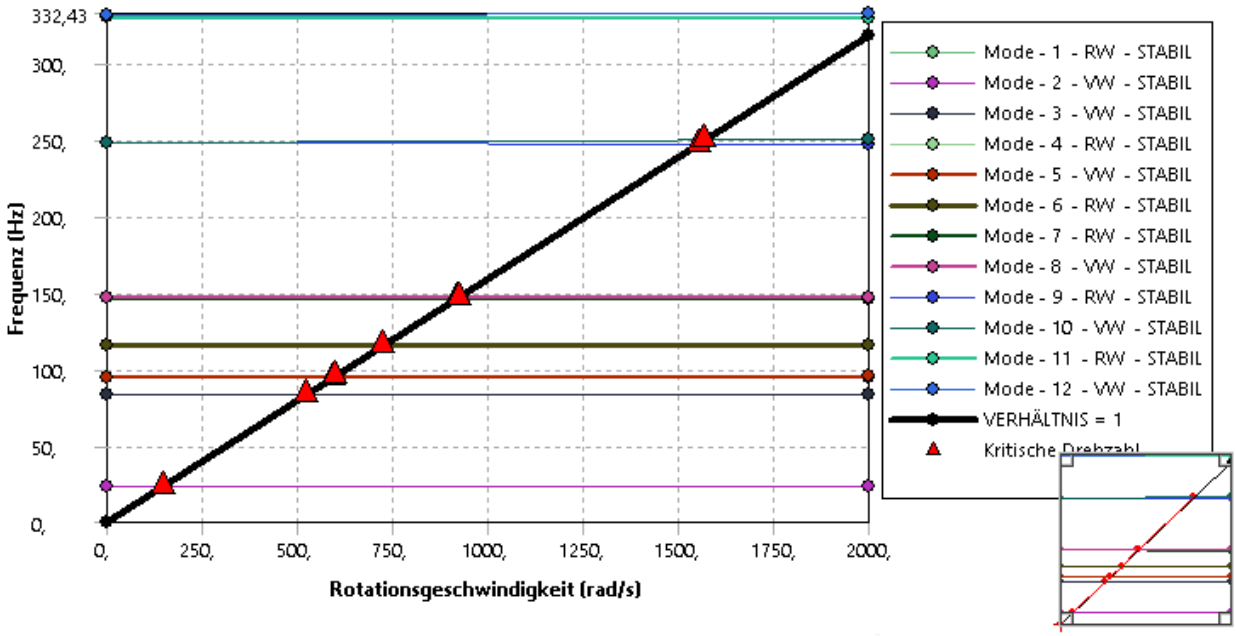

Figure 5.8: Campbell diagram at the drilling depth of 1000 mm with moving Lanchester damper.

The critical rotational speeds and corresponding eigenfrequencies with the fixed Lanchester damper are listed in table 5.1 and 5.2

Drilling depth	Frequency in Hz	Rotational speed in rad/s	Type of vibration
250 mm	43	270	Bending
	83	522	Longitudinal
	118	741	Torsional
	204	1282	Bending
	274	1722	Bending
500 mm	51	320	Bending
	83	522	Longitudinal
	114	716	Torsional
	137	861	Bending
	220	1382	Bending
	311	1954	Bending

Table 5.1: Critical speed at 250 mm and 500 mm drilling depth with fixed Lanchester damper.

Drilling depth	Frequency in Hz	Rotational speed in rad/s	Type of vibration
750 mm	45	283	Bending
	83	522	Longitudinal
	115	723	Torsional
	125	785	Bending
	212	1332	Bending
	295	1854	Bending
1000 mm	41	258	Bending
	83	522	Longitudinal
	115	723	Torsional
	126	792	Bending
	217	1363	Bending
	301	1891	Bending

Table 5.2: Critical speed at 750 mm and 1000 mm drilling depth with fixed Lanchester damper.

The critical rotational speeds and corresponding eigenfrequencies with the moving Lanchester damper are shown in table 5.3 and 5.4

Drilling depth	Frequency in Hz	Rotational speed in rad/s	Type of vibration
250 mm	29	182	Bending
	83	522	Longitudinal
	94	591	Bending
	115	723	Torsional
	194	1219	Bending
	314	1993	Bending
500 mm	27	170	Bending
	83	522	Longitudinal
	89	559	Bending
	115	723	Torsional
	190	1194	Bending
	235	1477	Bending

Table 5.3: Critical speed at 250 mm and 500 mm drilling depth with moving Lanchester damper.

Drilling depth	Frequency in Hz	Rotational speed in rad/s	Type of vibration
750 mm	24	151	Bending
	83	522	Longitudinal
	88	553	Bending
	115	723	Torsional
	167	1049	Bending
	210	1319	Bending
1000 mm	24	151	Bending
	83	522	Longitudinal
	94	591	Bending
	115	723	Torsional
	146	917	Bending
	248	1558	Bending

Table 5.4: Critical speed at 750 mm and 1000 mm drilling depth with moving Lanchester damper.

5.2 Pre-stressed modal analysis

Similarly, in the pre-stressed modal analysis, two setups regarding Lanchester damper were studied separately. One was that the distance between the Lanchester damper and the clamping end of the boring bar was fixed during drilling process and the other one was that the distance between the Lanchester damper and the stuffing box was fixed, which represented that the Lanchester damper moved during the drilling process. The reason for choosing modal analysis instead of harmonic analysis is that the eigenmodes must be plotted and the critical locations on the boring bar must be recorded regarding varying drilling depth for the further study of countermeasures against dynamic instability. Note that in the model setup in Ansys Workbench, the origin point in global coordinate system corresponds to the clamping end of boring bar and the axis of boring bar lies in the positive direction of z-axis.

5.2.1 Mechanical loads

The topologically optimized BTA tool head model and the for the specification of mechanical loads required local coordinate system are shown in figure 5.9 (a) and (b) respectively. The topology of the BTA tool head, guide pads and cutters influences not only the mesh generation in static structural module, but also the mesh in CFX module, as the fluid domain is created via boolean operation with the topology in the solid domain as the reference. The z-axis of the established local coordinate system matches the center axis of tool head, while the x-z plane matches the side face of a cutter as shown in figure 5.9 (b).

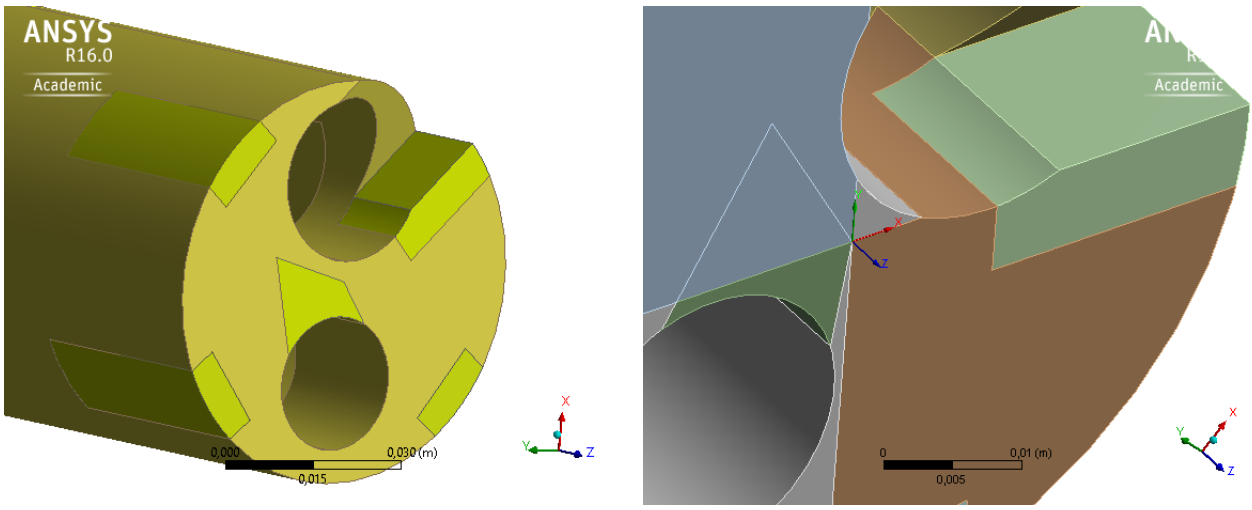

(a) Geometry of BTA tool head.

(b) Local coordinate system.

Figure 5.9: Geometry of tool head and local coordinate system in Ansys Workbench.

The axial force and torque that are applied on the tool head are shown in figure 5.10

(a) and (b) respectively.

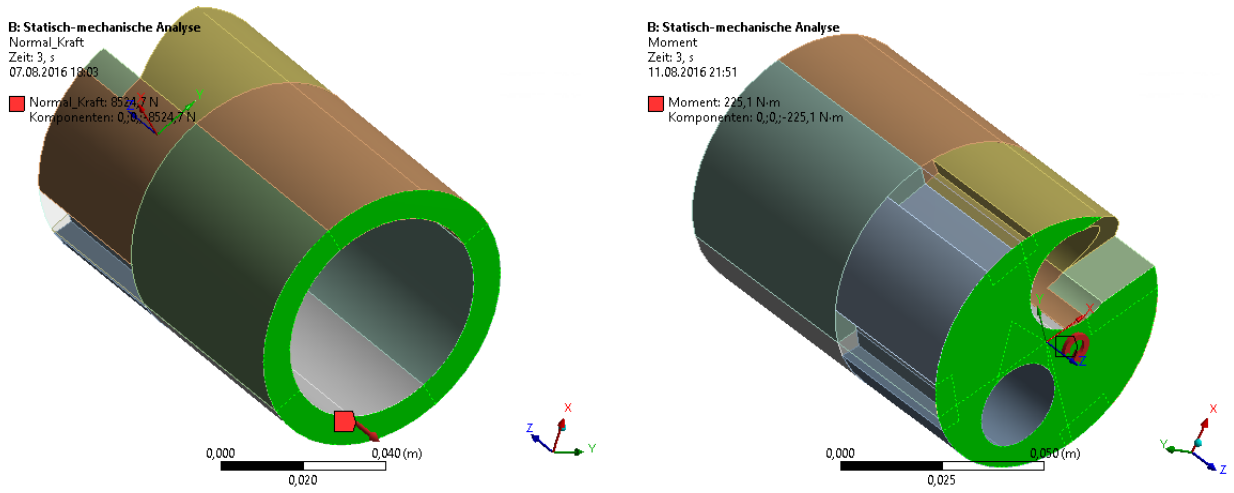

(a) Axial force in z direction.

(b) Torque on the front face of BTA tool head.

Figure 5.10: Axial force and Torque on the BTA tool head.

The bending moment in the normal direction was applied on the cut face in x-z plane of local coordinate system while the bending moment in the passive direction was applied on the cut face in y-z plane of local coordinate system. These are shown in figure 5.11 (a) and (b) respectively. The values of the axial force, the torsional and bending moments are obtained from experiments and given in Appendices.

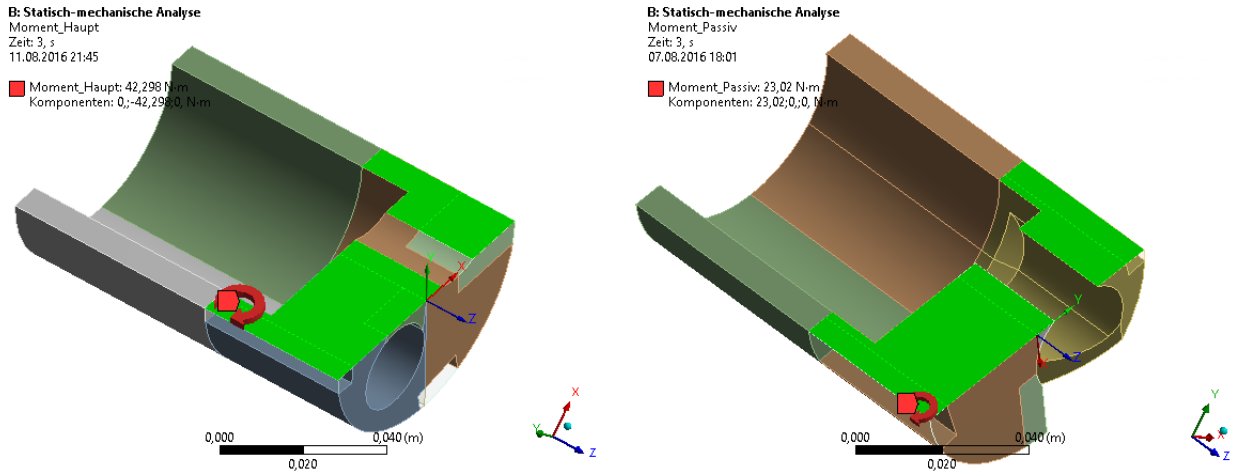

(a) Bending moment in normal direction.

(b) Bending moment in passive direction.

Figure 5.11: Bending moment on the tool head.

5.2.2 Modal participation factor and effective modal mass

To determine the dominant eigenmode, the modal participation factor and effective modal mass are generally considered as the criteria. The eigenmode with the largest values of these two is considered as dominant. A brief introduction is according to [32, 33, 34] given as follows.

Consider a dynamic system with a form in (5.1), where M, C, K, x and $\vec{f}$ represent the mass matrix, damping matrix, stiffness matrix, vector of degrees of freedoms and vector of external excitation and force respectively.

$$M\ddot{x} + C\dot{x} + Kx = \vec{f} \tag{5.1}$$

With the help of modal analysis, the eigenvector matrix can be obtained and noted as Ψ. The generalized mass matrix $\bar{M}$ and the coefficient vector $\bar{\Gamma}$ are then defined in (5.2) and (5.3), where ξ is the so-called unit ground displacement vector.

$$\bar{M} = \Psi^T M \Psi \tag{5.2}$$

$$\bar{\Gamma} = \Psi^T M \xi \tag{5.3}$$

According to Ansys manual, ξ is given in each direction of the global Cartesian coordinate system as the assumed displacement spectrum for the computation of participation factors.

The modal participation factor for mode j is then given in (5.4)

$$\Phi_j = \frac{\bar{\Gamma}_j}{\bar{M}_{jj}} \tag{5.4}$$

and the effective modal mass $m_{eff,j}$ for mode j is defined as (5.5)

$$m_{eff,j} = \frac{\bar{\Gamma}_j^2}{\bar{M}_{jj}} \tag{5.5}$$

Both modal participation factor and effective modal mass could be used to evaluate the dominant eigenmodes in modal analysis. Due to the conservation of mass in the dynamic system, Ansys Workbench has listed the results of ratios of the effective modal mass to the total mass, which will be used for the determination of dominant eigenmodes in this thesis.

5.2.3 Simulation with fixed Lanchester damper on the boring bar

The results of bending eigenfrequencies with varying drilling depth are shown in table 5.5 and 5.6.

Drilling depth in mm	Ef1 in Hz	Ef2 in Hz	Ef3 in Hz	Ef4 in Hz	Ef5 in Hz
50	34.1	99.6	197.2	291.4	326.1
100	36.5	104.8	205.6	291.5	337.3
150	38.6	109.8	214.1	291.7	349.0
200	40.5	114.4	222.4	291.8	360.8
250	42.2	119.0	230.8	291.9	372.7
300	43.9	123.5	239.3	292.0	383.8
350	45.6	128.1	248.1	292.1	386.5
400	47.3	132.9	257.2	292.2	368.9
450	49.0	137.8	266.5	292.5	346.5
500	50.9	143.0	275.9	293.0	323.3

Table 5.5: Bending eigenfrequencies with fixed Lanchester damper part 1.

Drilling depth in mm	Ef1 in Hz	Ef2 in Hz	Ef3 in Hz	Ef4 in Hz	Ef5 in Hz
550	52.8	148.3	284.4	294.4	300.8
600	54.8	153.9	277.2	289.9	301.5
650	57.0	159.7	256.8	290.8	311.8
700	59.2	165.5	238.0	291.2	323.6
750	61.6	171.0	222.0	291.4	336.1
800	64.1	174.8	209.0	291.6	349.2
850	66.7	173.5	203.5	291.7	362.6
900	69.5	166.0	206.1	291.8	374.9
950	72.4	156.4	213.2	291.8	379.9
1000	75.4	147.0	221.8	291.9	371.7

Table 5.6: Bending eigenfrequencies with fixed Lanchester damper part 2.

The results of torsional eigenfrequencies with varying drilling depth are shown in table 5.7 and 5.8.

Drilling depth in mm	Ef1 in Hz	Ef2 in Hz	Ef3 in Hz
50	252.4	740.0	1199.2
100	252.3	740.0	1199.2
150	252.3	740.0	1199.2
200	252.3	740.0	1199.2
250	252.3	740.0	1199.1
300	252.3	739.9	1199.1
350	252.3	739.9	1199.1
400	252.3	739.9	1199.1
450	252.3	739.9	1199.1
500	252.3	739.9	1199.1

Table 5.7: Torsional eigenfrequencies with fixed Lanchester damper part 1.

Drilling Depth in mm	Ef1 in Hz	Ef2 in Hz	Ef3 in Hz
550	252.3	739.8	1199.1
600	252.2	739.8	1199.1
650	252.2	739.8	1199.1
700	252.2	739.8	1199.2
750	252.2	739.8	1199.2
800	252.2	739.8	1199.2
850	252.2	739.8	1199.2
900	252.1	739.8	1199.2
950	252.1	739.8	1199.2
1000	252.1	739.8	1199.2

Table 5.8: Torsional eigenfrequencies with fixed Lanchester damper part 2.

The tendency chart of the drilling-depth dependent bending and torsional eigenfrequencies is shown in figure 5.12, where blue lines represent bending eigenfrequencies and red lines represent torsional eigenfrequencies respectively.

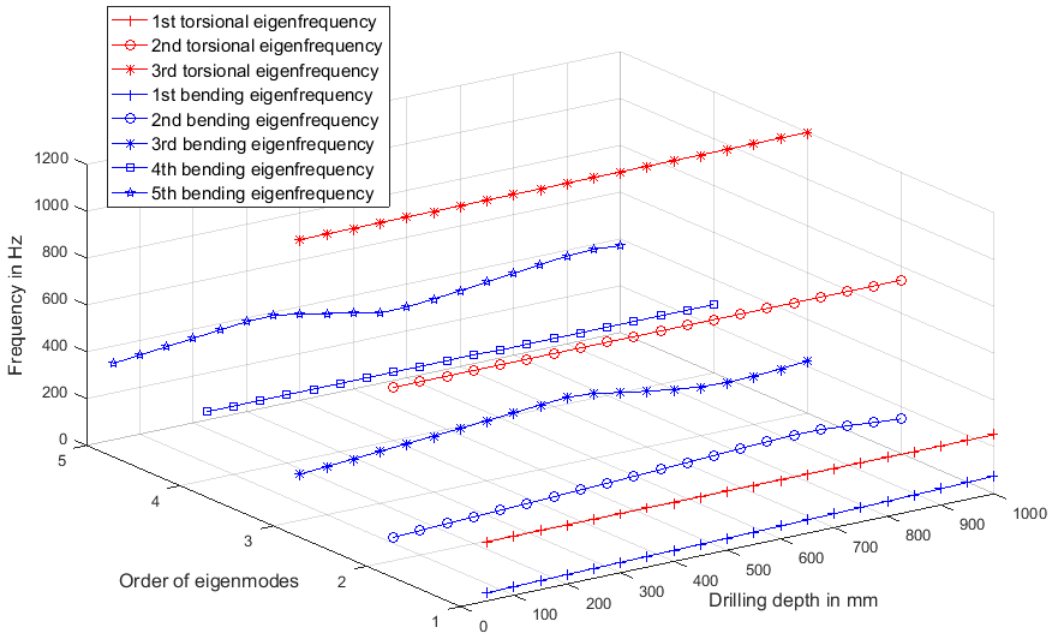

Figure 5.12: Bending and torsional eigenfrequencies with different drilling depths for fixed damper.

In figure 5.12 it can be seen that with the fixed Lanchester damper, bending eigenfrequencies vary significantly with different drilling depths while the torsional eigenfrequencies stay almost constant. Their values could be seen in table 5.5 to 5.8.

The first dominant eigenmodes and their corresponding ratios of effective mass and locations on the boring bar in bending modal analysis with respect to drilling depths were recorded and the results are listed in table 5.9 and 5.10

Drilling depth	Order of 1st dominant mode	Ratio of eff. mass	z-coordinate in m
50 mm	1	50.8%	2.55
100 mm	1	49.5%	2.50
150 mm	1	48.5%	2.46
200 mm	1	47.4%	2.42
250 mm	1	46.1%	2.40
300 mm	1	44.9%	2.37
350 mm	1	44.2%	2.34
400 mm	1	43.5%	2.32
450 mm	1	42.7%	2.30
500 mm	1	41.8%	2.27

Table 5.9: Study of first dominant bending eigenmodes with fixed Lanchester damper part 1.

Drilling depth	Order of 1st dominant mode	Ratio of eff. mass	z-coordinate in m
550 mm	1	40.8%	2.25
600 mm	1	39.8%	2.23
650 mm	1	38.7%	2.21
700 mm	1	37.5%	2.18
750 mm	1	36.2%	2.16
800 mm	1	34.9%	2.13
850 mm	1	33.5%	2.11
900 mm	1	31.9%	2.08
950 mm	1	30.2%	2.06
1000 mm	1	28.4%	2.04

Table 5.10: Study of first dominant bending eigenmodes with fixed Lanchester damper part 2.

The results in terms of the computation of modal participation factor and the effective mass are from a unit displacement spectrum vector in the three translational

directions in the global coordinate system in Ansys Workbench and the ratios of the effective mass from torsional eigenmodes are therefore significantly smaller than those of bending eigenmodes. The criterion here for the determination of the dominant torsional mode is therefore the comparison among the results from torsional eigenmodes only, which is different from the criterion in bending analysis. The dominant eigenmodes and their corresponding ratios of effective mass in torsional modal analysis were recorded and the results are listed in table 5.11 and 5.12. Comparing to the bending case, the critical location for torsional vibration is fixed at the end face of tool head.

Drilling depth	Order of 1st dominant mode	Ratio of eff. mass (torsional only)
50 mm	1	69.2%
100 mm	1	67.7%
150 mm	1	65.8%
200 mm	1	64.3%
250 mm	1	62.7%
300 mm	1	59.8%
350 mm	1	58.2%
400 mm	1	59.3%
450 mm	1	61.5%
500 mm	1	62.1%

Table 5.11: Study of first dominant torsional eigenmodes with fixed Lanchester damper part 1.

Drilling depth	Order of 1st dominant mode	Ratio of eff. mass (torsional only)
550 mm	1	59.9%
600 mm	1	57.3%
650 mm	1	54.9%
700 mm	1	50.8%
750 mm	1	48.3%
800 mm	1	50.4%
850 mm	1	52.9%
900 mm	1	49.2%
950 mm	1	44.7%
1000 mm	1	38.3%

Table 5.12: Study of first dominant torsional eigenmodes with fixed Lanchester damper part 2.

To meet the demand for further researches, the second dominant bending eigenmodes are recorded and are given in table 5.13 and 5.14 for fixed Lanchester damper. The determination of dominant modes is based on the computation of modal participation factors and the effective mass, which is however obtained with a unit displacement vector in the global coordinate system and the bending analysis influences the results on a different order of magnitude comparing to torsional analysis. The critical locations of torsional eigenmodes are fixed at the front face of tool head during the deep hole drilling process and the prior countermeasure for chatter prevention is controlling of the rotational speed, while the countermeasures regarding spiralling take the critical locations on the boring bar as critical factors into consideration and the damage on the workpiece due to spiralling is more significant comparing to chatter vibration. The study for the second dominant mode is therefore of vital importance for prevention of spiralling comparing to chatter vibration.

Drilling depth	Order of 2nd dominant mode	Ratio of eff. mass	z-coordinate in m
50 mm	4	13.5%	0.56
100 mm	4	13.9%	0.56
150 mm	4	14.0%	0.56
200 mm	4	13.6%	0.56
250 mm	4	13.6%	0.56
300 mm	4	13.5%	0.56
350 mm	4	13.0%	0.56
400 mm	4	11.7%	0.56
450 mm	4	12.7%	0.56
500 mm	4	15.0%	0.56

Table 5.13: Study of the second dominant bending eigenmodes with fixed Lanchester damper part 1.

Drilling depth	Order of 2nd dominant mode	Ratio of eff. mass	z-coordinate in m
550 mm	4	19.7%	0.56
600 mm	3	14.7%	3.53
650 mm	3	13.7%	3.52
700 mm	4	14.5%	0.56
750 mm	3	23.5%	3.48
800 mm	3	20.8%	3.47
850 mm	2	21.4%	3.44
900 mm	2	22.2%	3.42
950 mm	2	21.4%	3.40
1000 mm	4	18.8%	0.56

Table 5.14: Study of the second dominant bending eigenmodes with fixed Lanchester damper part 2.

The characteristics of dominant eigenmodes regarding drilling depth are shown in figure 5.13.

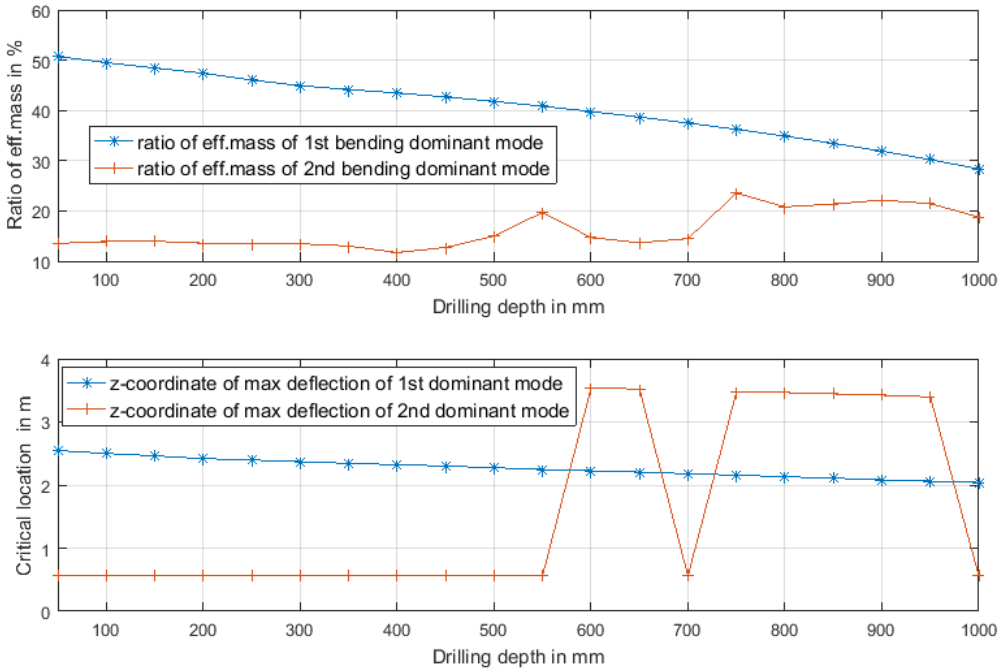

Figure 5.13: Critical analysis for bending modes with fixed damper.

Here it can be seen that the ratio of effective mass of the first dominant mode stays above than that of the second dominant mode during the drilling process and the corresponding critical location on the boring bar moves slowly towards the end of the boring bar. The ratio of effective mass of the second dominant mode increases as the BTA tool drills deeper. The difference between the ratios of effective mass of the first and second dominant modes decreases during the drilling process, which means the energy of vibration starts to distribute to multiple eigenmodes. From the drilling depth of 750 mm till 1000 mm, the difference narrows more significantly than in other drilling depths. The critical location for the second dominant mode fluctuates from the end of the boring bar to the part that is inside or near the workpiece starting from the drilling depth of 550 mm till 1000 mm. Considering the high ratio of effective mass, the boring bar inside the workpiece with drilling depth between 750 mm and 950 mm could be subjected to a bending vibration with noticeable amplitude.

5.2.4 Comparison of the influence from each boundary condition

Comparing to the fully stressed model with varying values of boundary conditions, the simulations were also carried out to determine the influence of each variable. The results of the setup without mechanical loads comparing to the fully stressed model at the drilling depths of 50 mm and 100 mm are shown in table 5.15.

Eigenfrequency	50 mm	rel. Error	100 mm	rel. Error
BEf 1 in Hz	34.4	1.0%	36.8	0.9%
BEf 2 in Hz	100.0	0.4%	105.3	0.4%
BEf 3 in Hz	197.7	0.2%	206.1	0.2%
BEf 4 in Hz	291.7	0.1%	291.9	0.1%
BEf 5 in Hz	326.6	0.2%	337.8	0.1%
Order of 1st dominant mode	1	-	1	-
Ratio of eff. mass	50.8%	0.0%	49.5%	0.0%
Eigenfrequency	50 mm	rel. Error	100 mm	rel. Error
TEf 1 in Hz	252.4	0.0%	252.4	0.0%
TEf 2 in Hz	740.0	0.0%	740.0	0.0%
TEf 3 in Hz	1199.2	0.0%	1199.2	0.0%
Order of 1st dominant mode	1	-	1	-
Ratio of eff. mass	69.2%	0.0%	67.7%	0.0%

Table 5.15: Results without mechanical loads for drilling depths of 50 and 100 mm.

Here it can be seen the difference between results with and without mechanical loads for the eigenfrequencies is relatively small. The largest relative error shows at the first bending mode at 50 mm drilling depth with around 1%. The small difference is mainly due to the fact that the mechanical loads are applied at BTA tool head, where elastic support with high stiffness limits the deformation (seen in chapter 4.1). Furthermore, no significant difference is observed between the results in the drilling depths of 50 mm and 100 mm. The small influence is mainly seen in different orders of eigenfrequency while the eigenmodes don't change. Similar results are also observed in the simulations for other drilling depths. The mechanical loads are therefore suggested to be ignored in case a better mesh quality and less computational effort are required.

The results of setup without FSI comparing to the fully stressed model for the drilling depths of 50 mm and 100 mm are shown in table 5.16.

Eigenfrequency	50 mm	rel. Error	100 mm	rel. Error
BEf 1 in Hz	35.4	3.9%	37.9	3.9%
BEf 2 in Hz	103.4	3.8%	108.7	3.7%
BEf 3 in Hz	204.8	3.8%	213.5	3.9%
BEf 4 in Hz	302.0	3.6%	302.1	3.6%
BEf 5 in Hz	338.4	3.8%	350.0	3.8%
Order of 1st dominant mode	1	-	1	-
Ratio of eff. mass	51.2%	1.0%	50.0%	0.9%
Eigenfrequency	50 mm	rel. Error	100 mm	rel. Error
TEf 1 in Hz	256.2	1.5%	255.8	1.4%
TEf 2 in Hz	748.6	1.2%	748.6	1.2%
TEf 3 in Hz	1219.5	1.7%	1219.5	1.7%
Order of 1st dominant mode	1	-	1	-
Ratio of eff. mass	69.5%	0.5%	68.1%	0.5%

Table 5.16: Results without FSI for the drilling depths of 50 and 100 mm.

Here it can be seen the eigenfrequencies without FSI are higher than those with FSI in each order. This is mainly due to the damping effect from fluid domain. The influence of FSI is larger in bending eigenfrequencies than that in torsional ones. The dominant modes however don't change. Furthermore, no significant difference is observed between the results in the drilling depths of 50 mm and 100 mm. Similar results are also observed in the simulations for other drilling depths. The relative error for bending eigenfrequencies is around 3% and therefore the FSI is not suggested to be overlooked.

The results of setup with mean values of boundary conditions in different drilling depths comparing to the results with drilling-depth dependent inputs at the drilling depths of 50 mm and 100 mm are shown in table 5.17. The reason for chosing 50 mm and 100 mm drilling depths is that the values of factors for 50 mm and 100 mm differ from the mean values more significantly than the ones for other drilling depths.

Eigenfrequency	50 mm	rel. Error	100 mm	rel. Error
BEf 1 in Hz	32.8	-3.6%	35.4	-3.0%
BEf 2 in Hz	96.9	-2.7%	102.3	-2.4%
BEf 3 in Hz	193.0	-2.1%	201.6	-2.0%
BEf 4 in Hz	290.6	-0.3%	290.8	-0.2%
BEf 5 in Hz	320.8	-1.6%	332.5	-1.4%
Order of 1st dominant mode	1	-	1	-
Ratio of eff. mass	50.6%	-0.4%	49.4%	-0.2%
Eigenfrequency	50 mm	rel. Error	100 mm	rel. Error
TEf 1 in Hz	249.9	-1.0%	249.8	-1.0%
TEf 2 in Hz	730.0	-1.4%	729.9	-1.4%
TEf 3 in Hz	1157.3	-3.5%	1157.3	-3.5%
Order of 1st dominant mode	1	-	1	-
Ratio of eff. mass	68.9%	-0.4%	67.4%	-0.5%

Table 5.17: Results with mean values of factors for the drilling depths of 50 and 100 mm

Here it can be seen the results with mean values of factors as the input show a difference with less than 4% comparing to the ones with varying values in different drilling depths. The reason lies mainly in the influence on the construction of the stiffness matrix of the dynamic system in the FE simulation. Moreover, the input of the drilling-depth dependent values could inherit accumulated error from numerical approximation towards experimental data, the comparison here is therefore mainly supposed to verify the validity of the assumption that the drilling-depth dependent values of boundary conditions influence the eigenanalyses. Some researches are also done in ideal boundary conditions, such as rigid support instead of elastic support for tool head. Whether these simplifications are acceptable depends on the error tolerance for different cases.

5.2.5 Simulation with moving Lanchester damper on the boring bar

The results for bending eigenanalysis are shown in table 5.18 and 5.19.

Drilling depth in mm	Ef1 in Hz	Ef2 in Hz	Ef3 in Hz	Ef4 in Hz	Ef5 in Hz
50	40.5	114.5	223.6	307.1	367.2
100	42.1	118.6	231.5	308.7	379.9
150	43.7	122.9	239.7	310.3	393.2
200	45.4	127.4	248.5	311.6	407.3
250	47.2	132.2	257.6	312.5	422.2
300	49.1	137.3	267.3	313.3	437.9
350	51.1	142.7	277.5	313.8	454.5
400	53.2	148.3	288.1	314.3	471.8
450	55.5	154.3	299.4	315.2	444.8
500	57.8	160.7	308.7	317.9	401.8

Table 5.18: Bending eigenfrequencies with moving Lanchester damper part 1.

Drilling depth in mm	Ef1 in Hz	Ef2 in Hz	Ef3 in Hz	Ef4 in Hz	Ef5 in Hz
550	60.4	167.5	312.4	327.2	363.1
600	63.1	174.7	313.2	328.5	340.5
650	65.9	182.4	298.2	313.6	354.8
700	69.0	190.5	271.5	313.8	370.3
750	72.2	199.3	247.9	313.9	386.9
800	75.7	208.6	227.1	314.0	404.7
850	79.5	208.6	218.7	314.1	423.8
900	83.5	192.3	229.4	314.2	444.2
950	87.8	177.7	240.9	314.3	466.0
1000	92.4	164.7	253.3	314.4	460.6

Table 5.19: Bending eigenfrequencies with moving Lanchester damper part 2.

The results for torsional eigenanalysis are shown in table 5.20 and 5.21 .

Drilling depth in mm	Ef1 in Hz	Ef2 in Hz	Ef3 in Hz
50	533.0	663.5	1072.6
100	540.8	638.8	1090.3
150	547.7	617.4	1108.7
200	551.6	600.9	1127.7
250	548.4	593.6	1147.4
300	537.0	596.2	1167.7
350	522.4	603.7	1188.6
400	507.2	613.4	1210.0
450	492.4	624.3	1231.5
500	478.1	635.9	1252.7

Table 5.20: Torsional eigenfrequencies with moving Lanchester damper part 1.

Drilling depth in mm	Ef1 in Hz	Ef2 in Hz	Ef3 in Hz
550	464.6	648.2	1272.0
600	451.7	661.2	1284.9
650	439.5	674.9	1282.2
700	427.9	689.1	1263.1
750	416.9	704.0	1236.9
800	406.5	719.7	1208.9
850	396.5	736.0	1181.1
900	387.1	753.1	1154.0
950	378.1	771.0	1128.0
1000	369.5	789.6	1103.0

Table 5.21: Torsional eigenfrequencies with moving Lanchester damper part 2.

The tendency chart of the drilling-depth dependent bending and torsional eigenfrequencies is shown in figure 5.14, where blue lines represent bending eigenfrequencies and red lines represent torsional eigenfrequencies in the drilling process respectively. In figure 5.14 it can be seen that with the moving Lanchester damper, both bending

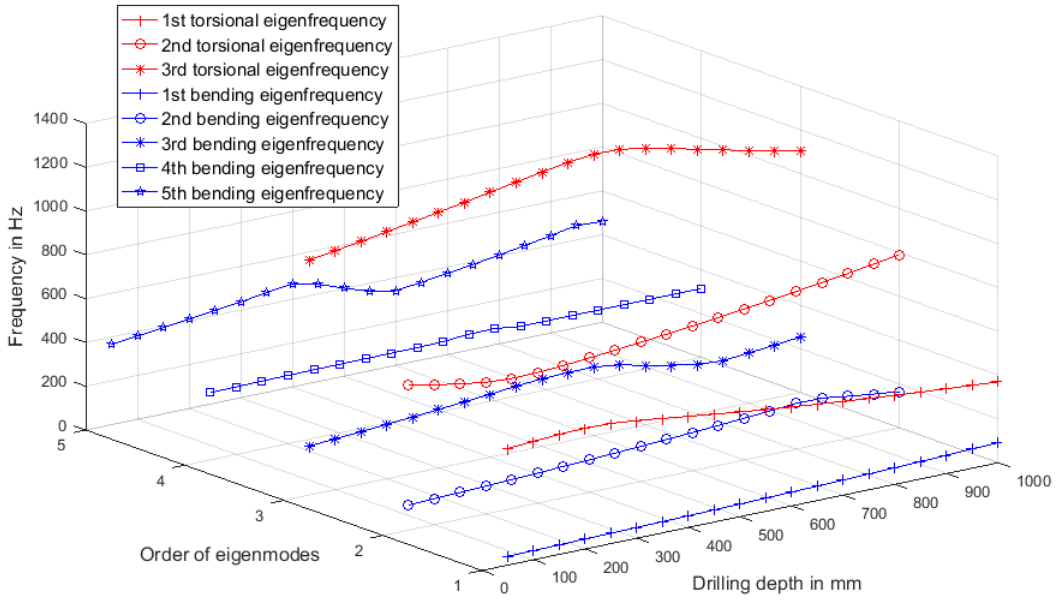

Figure 5.14: Bending and torsional eigenfrequencies with different drilling depths with moving Lanchester damper.

and torsional eigenfrequencies vary significantly with different drilling depths, which is a contrast to figure 5.12. The corresponding values can be seen in table 5.18 to 5.21.

Results regarding the first dominant bending eigenmodes and their corresponding ratios of effective mass and locations on the boring bar are listed in table 5.22 and 5.23

Drilling depth	Order of 1st dominant mode	Ratio of eff. mass	z-coordinate in m
50 mm	1	47.2%	1.57
100 mm	1	46.4%	1.54
150 mm	1	45.5%	1.51
200 mm	1	44.7%	1.49
250 mm	1	43.9%	1.47
300 mm	1	43.0%	1.44
350 mm	1	42.2%	1.41
400 mm	1	41.3%	1.39
450 mm	1	40.5%	1.36
500 mm	1	39.7%	1.34

Table 5.22: Study of the first dominant bending eigenmodes with moving Lanchester damper part 1.

Drilling depth	Order of 1st dominant mode	Ratio of eff. mass	z-coordinate in m
550 mm	1	38.8%	1.32
600 mm	1	38.0%	1.29
650 mm	1	37.1%	1.26
700 mm	1	36.3%	1.24
750 mm	1	35.5%	1.21
800 mm	1	34.6%	1.19
850 mm	1	33.8%	1.17
900 mm	1	33.0%	1.14
950 mm	1	32.1%	1.11
1000 mm	1	31.3%	1.09

Table 5.23: Study of the first dominant bending eigenmodes with moving Lanchester damper part 2.

Results regarding critical torsional eigenmodes and their corresponding ratios of effective mass are listed in table 5.24 and 5.25. Again, the criterion here for the deter-

mination of the dominant torsional mode is the comparison among the results from torsional eigenmodes only, which is different from the one in bending analysis. Similarly, comparing to the bending case, the critical location for torsional vibration is fixed at the end face of BTA tool head again.

Drilling depth	Order of 1st dominant mode	Ratio of eff. mass (torsional only)
50 mm	1	79.2%
100 mm	1	74.2%
150 mm	1	70.3%
200 mm	1	69.4%
250 mm	1	70.3%
300 mm	1	73.1%
350 mm	1	77.9%
400 mm	1	77.3%
450 mm	1	72.3%
500 mm	1	66.7%

Table 5.24: Study of the first dominant torsional eigenmodes with moving Lanchester damper part 1.

Drilling depth	Order of 1st dominant mode	Ratio of eff. mass (torsional only)
550 mm	1	62.4%
600 mm	1	63.1%
650 mm	1	67.7%
700 mm	1	74.1%
750 mm	1	71.4%
800 mm	1	61.8%
850 mm	1	50.9%
900 mm	1	50.3%
950 mm	1	51.7%
1000 mm	1	53.7%

Table 5.25: Study of the first dominant torsional eigenmodes with moving Lanchester damper part 2.

The second dominant bending eigenmodes are recorded and are given in table 5.26 and 5.27 for moving Lanchester damper.

Drilling depth	Order of 2nd dominant mode	Ratio of eff. mass	z-coordinate in m
50 mm	4	16.0%	3.49
100 mm	4	17.5%	3.45
150 mm	4	18.4%	3.40
200 mm	4	19.3%	3.36
250 mm	4	20.1%	3.31
300 mm	4	21.0%	3.27
350 mm	4	22.0%	3.22
400 mm	4	23.3%	3.17
450 mm	4	25.7%	3.11
500 mm	4	27.0%	3.07

Table 5.26: Study of the second dominant bending eigenmodes with moving Lanchester damper part 1.

Drilling depth	Order of 2nd dominant mode	Ratio of eff. mass	z-coordinate in m
550 mm	4	16.7%	0.61
600 mm	3	15.5%	2.97
650 mm	4	17.2%	2.92
700 mm	4	18.0%	2.87
750 mm	4	17.7%	2.82
800 mm	4	20.8%	2.77
850 mm	4	20.3%	2.72
900 mm	4	20.4%	2.67
950 mm	4	20.6%	2.62
1000 mm	4	20.7%	2.57

Table 5.27: Study of the second dominant bending eigenmodes with moving Lanchester damper part 2.

The corresponding characteristics of dominant eigenmodes regarding the drilling depth are shown in figure 5.15

Here it can be seen that during the whole drilling process, the ratio of effective mass of the first dominant mode decreases monotonically and the critical location moves towards the clamping end of the boring bar. The difference between the ratios of effective mass of the first and second dominant modes decreases in the process of the first 500 mm drilling depth and reaches its minimum at 500 mm, where the critical location on the boring bar of the second dominant mode is near the workpiece. Within the drilling depth between 500 and 600 mm, the ratio of effective mass of the second dominant mode decreases and the corresponding critical location on the boring bar fluctuates temporarily. From the drilling depth of 600 mm the ratio of effective mass of the second dominant mode increases again and the corresponding location moves from the area near the workpiece towards the clamping end. Although the difference regarding the ratios of effective mass for both modes narrows again, the corresponding critical location is out of the bore hole. Based on the difference of the ratios of effective mass of the two dominant modes, the influence of the second dominant mode is significant in the first 500 mm drilling depth as its critical location is near the workpiece with increasing vibrating energy.

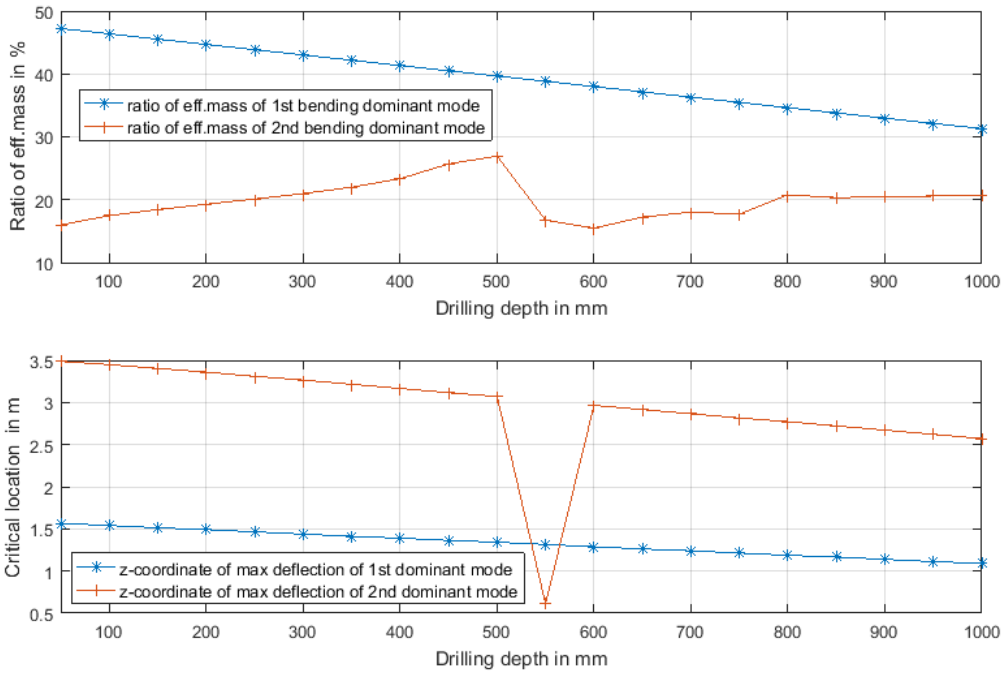

Figure 5.15: Critical analysis for bending eigenmodes with moving Lanchester damper.

5.2.6 Plots of eigenmodes for 100 and 400 mm drilling depths

A plot of an eigenmode gives an intuitive grasp of the whole form of the eigenvibration, range of influence of the vibration and the critical location with its maximal deflection, which is eventually reliable for further studies in terms of predictions and countermeasures against chatter vibration and spiralling. Figure 5.16 to 5.20 show the bending eigenmodes of the BTA machine at the drilling depth of 100 and 400 mm respectively with fixed Lanchester damper. The plots for 700 mm and 1000 mm are seen in Appendices.

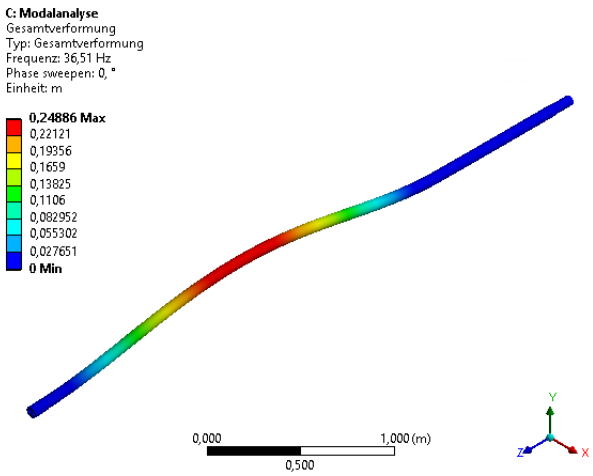

(a) Bending eigenmode 1 for 100 mm.

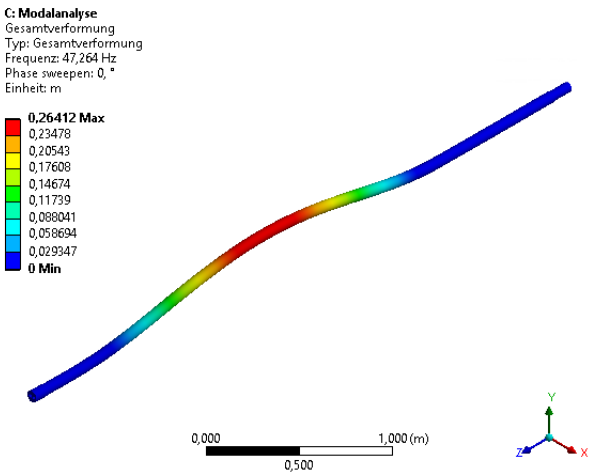

(b) Bending eigenmode 1 for 400 mm.

Figure 5.16: Bending eigenmode 1 for 100 and 400 mm with fixed Lanchester damper

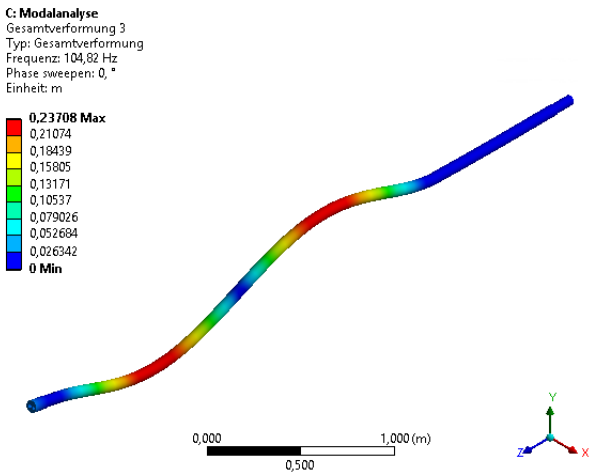

(a) Bending eigenmode 2 for 100 mm.

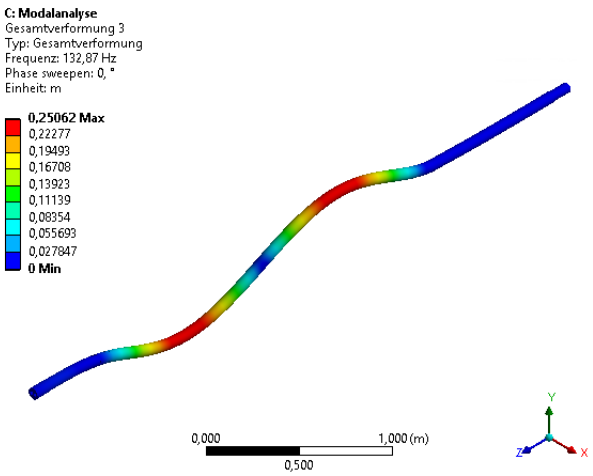

(b) Bending eigenmode 2 for 400 mm.

Figure 5.17: Bending eigenmode 2 for 100 and 400 mm with fixed Lanchester damper

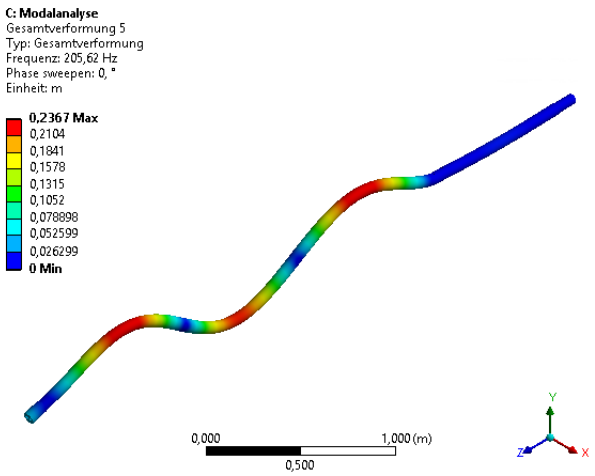

(a) Bending eigenmode 3 for 100 mm.

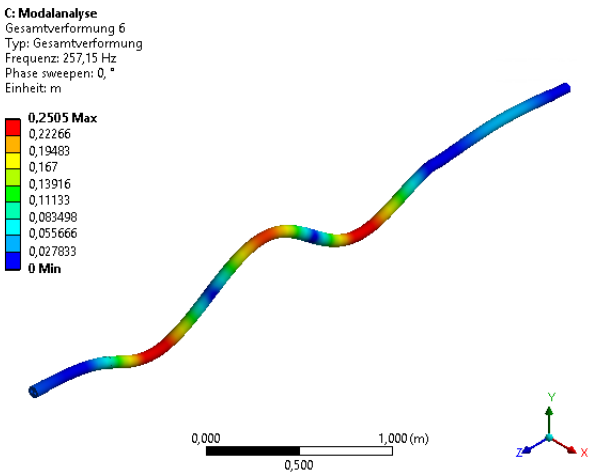

(b) Bending eigenmode 3 for 400 mm.

Figure 5.18: Bending eigenmode 3 for 100 and 400 mm with fixed Lanchester damper

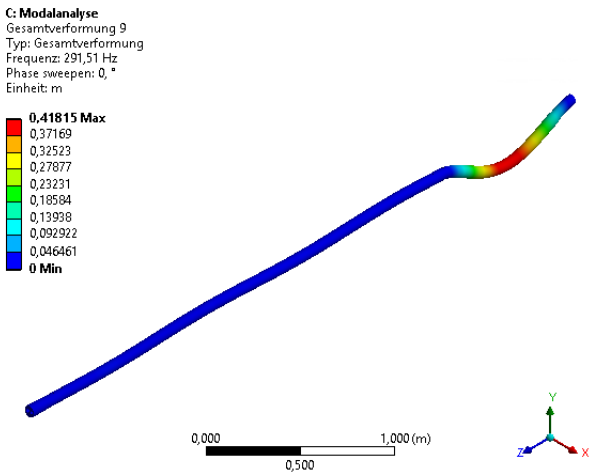

(a) Bending eigenmode 4 for 100 mm.

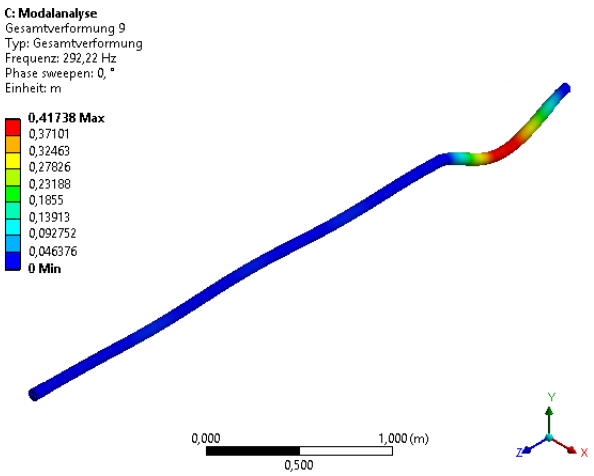

(b) Bending eigenmode 4 for 400 mm.

Figure 5.19: Bending eigenmode 4 for 100 and 400 mm with fixed Lanchester damper

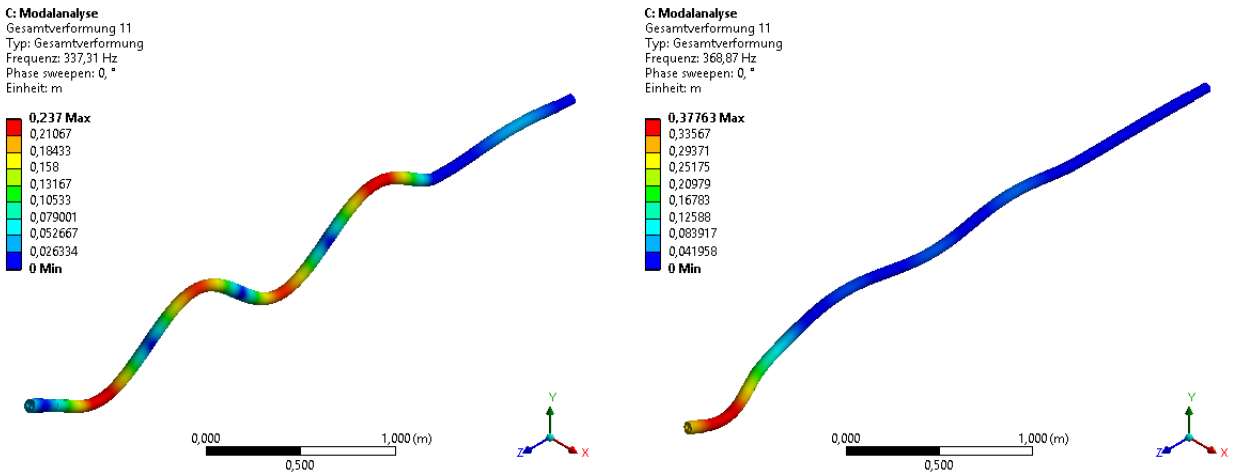

(a) Bending eigenmode 5 for 100 mm.

(b) Bending eigenmode 5 for 400 mm.

Figure 5.20: Bending eigenmode 5 for 100 and 400 mm with fixed Lanchester damper

The torsional eigenmodes don't show big difference at different drilling depths with fixed Lanchester damper. Therefore only the plots for 100 and 400 mm drilling depth are given in figure 5.21 to 5.23 as an example.

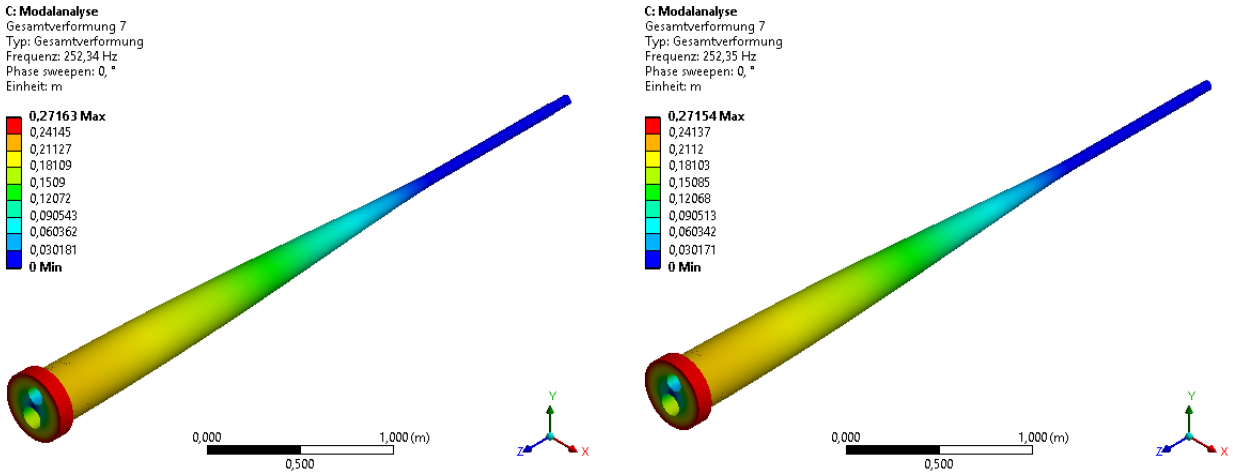

(a) Torsional eigenmode 1 for 100 mm.

(b) Torsional eigenmode 1 for 400 mm.

Figure 5.21: Torsional eigenmode 1 for 100 and 400 mm with fixed Lanchester damper

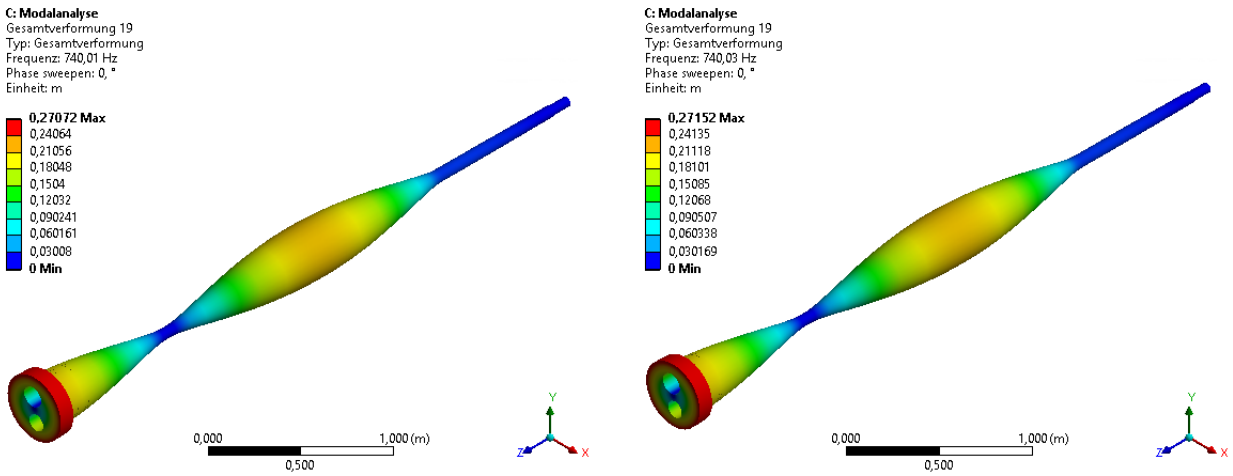

(a) Torsional eigenmode 2 for 100 mm.

(b) Torsional eigenmode 2 for 400 mm.

Figure 5.22: Torsional eigenmode 2 for 100 and 400 mm with fixed Lanchester damper

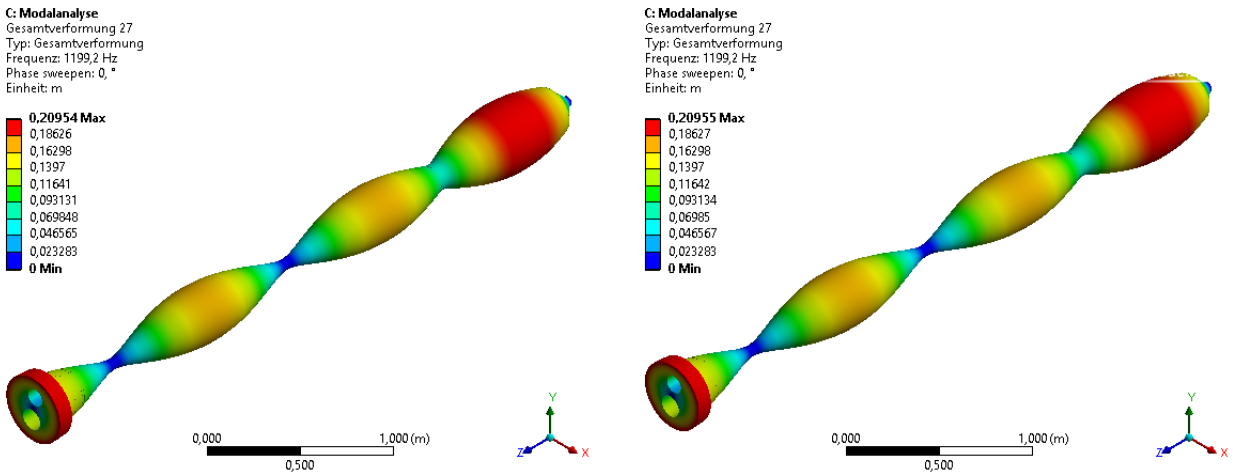

(a) Torsional eigenmode 3 for 100 mm.

(b) Torsional eigenmode 3 for 400 mm.

Figure 5.23: Torsional eigenmode 3 for 100 and 400 mm with fixed Lanchester damper

Figure 5.24 to 5.28 show the bending eigenmodes of the BTA machine at the drilling length of 100 and 400 mm respectively with the moving Lanchester damper. The plots for 700 mm and 1000 mm are seen in Appendices.

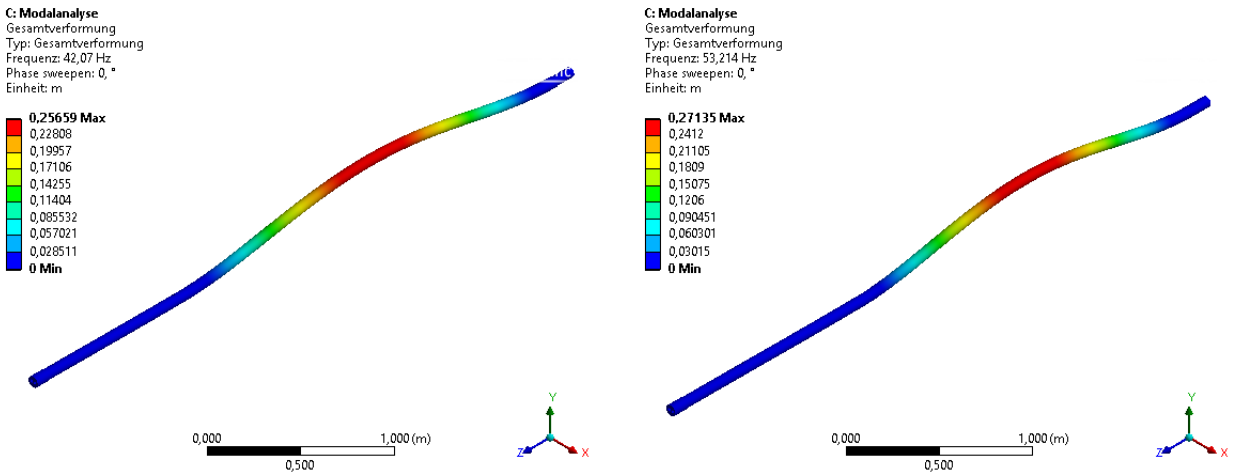

(a) Bending eigenmode 1 for 100 mm.

(b) Bending eigenmode 1 for 400 mm.

Figure 5.24: Bending eigenmode 1 for 100 and 400 mm with moving Lanchester damper

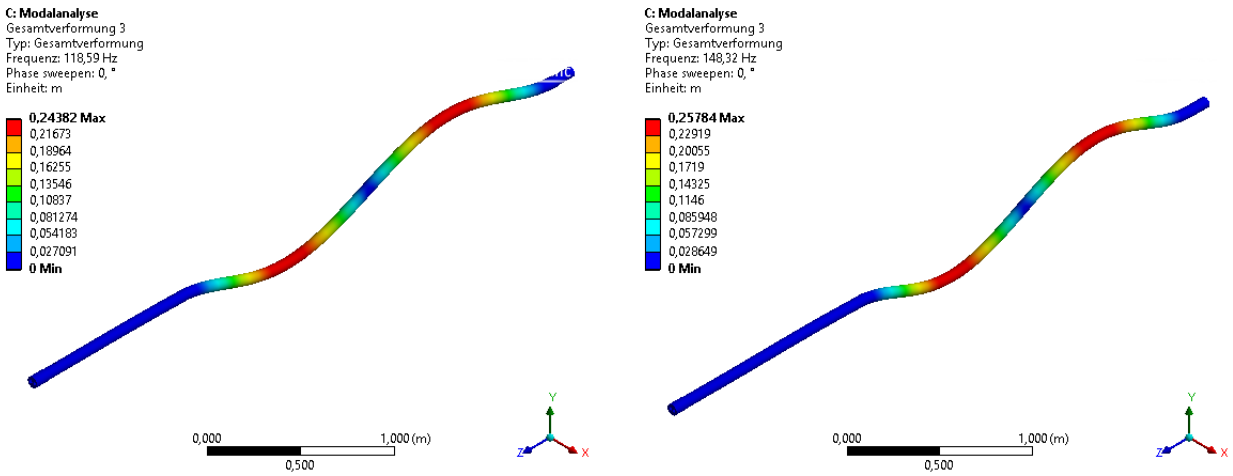

(a) Bending eigenmode 2 for 100 mm.

(b) Bending eigenmode 2 for 400 mm.

Figure 5.25: Bending eigenmode 2 for 100 and 400 mm with moving Lanchester damper

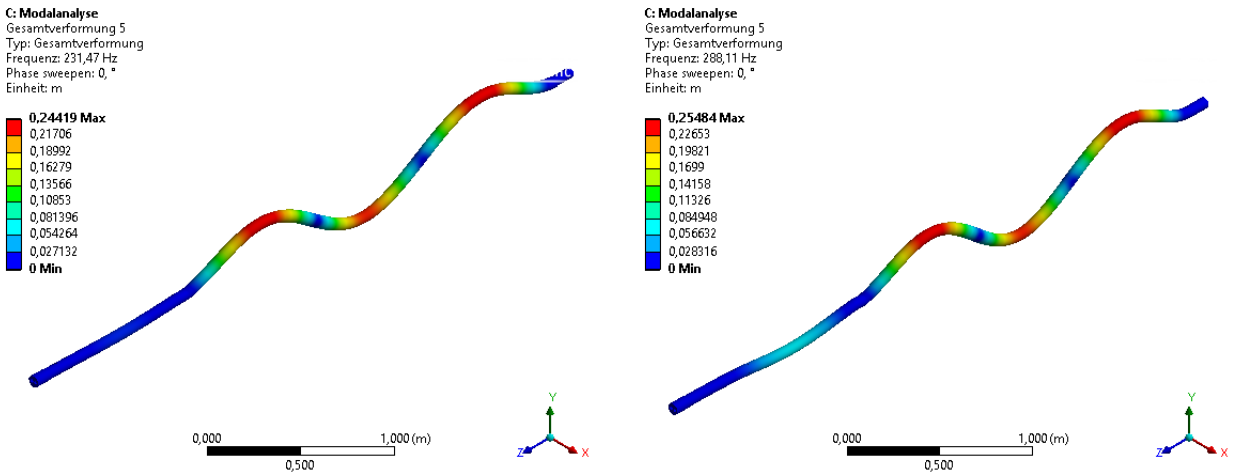

(a) Bending eigenmode 3 for 100 mm.

(b) Bending eigenmode 3 for 400 mm.

Figure 5.26: Bending eigenmode 3 for 100 and 400 mm with moving Lanchester damper

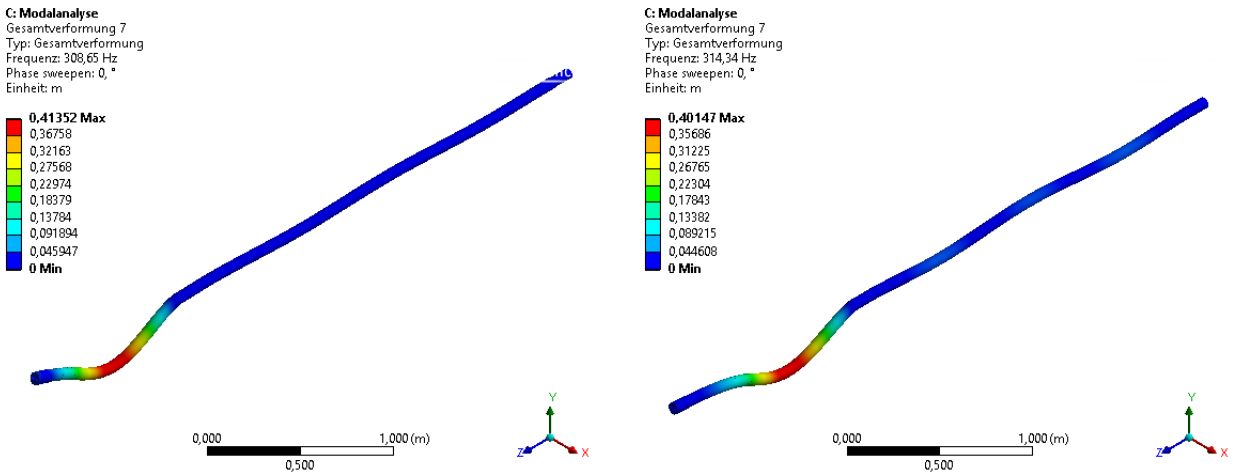

(a) Bending eigenmode 4 for 100 mm.

(b) Bending eigenmode 4 for 400 mm.

Figure 5.27: Bending eigenmode 4 for 100 and 400 mm with moving Lanchester damper

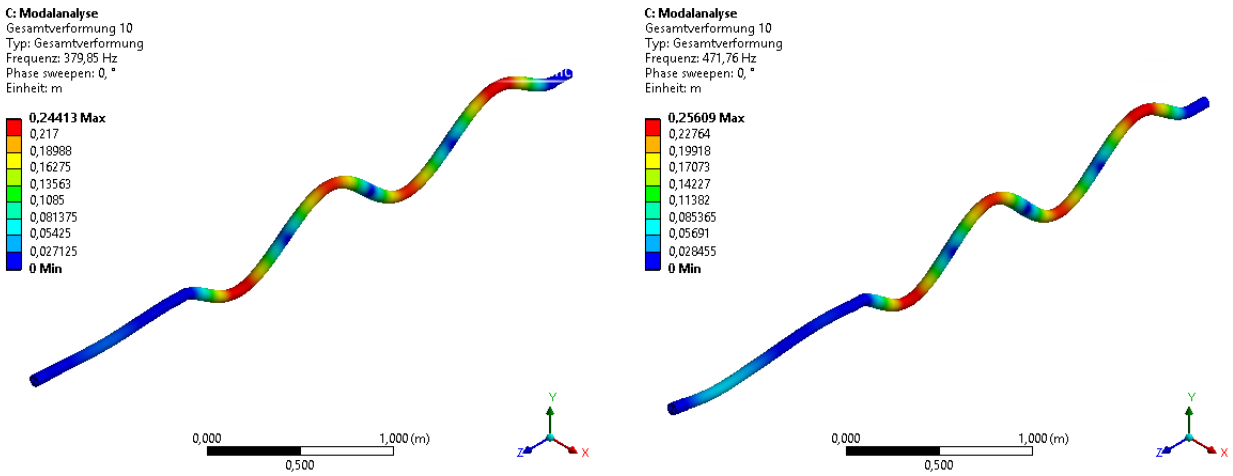

(a) Bending eigenmode 5 for 100 mm.

(b) Bending eigenmode 5 for 400 mm.

Figure 5.28: Bending eigenmode 5 for 100 and 400 mm with moving Lanchester damper

The torsional eigenmodes vary as the drilling depth changes in case Lanchester damper moves with the stuffing box with respect to the boring bar. Figure 5.29 to 5.31 show the torsional eigenmodes of the BTA machine at the drilling length of 100 and 400 mm respectively. The plots for 700 mm and 1000 mm are seen in Appendices.

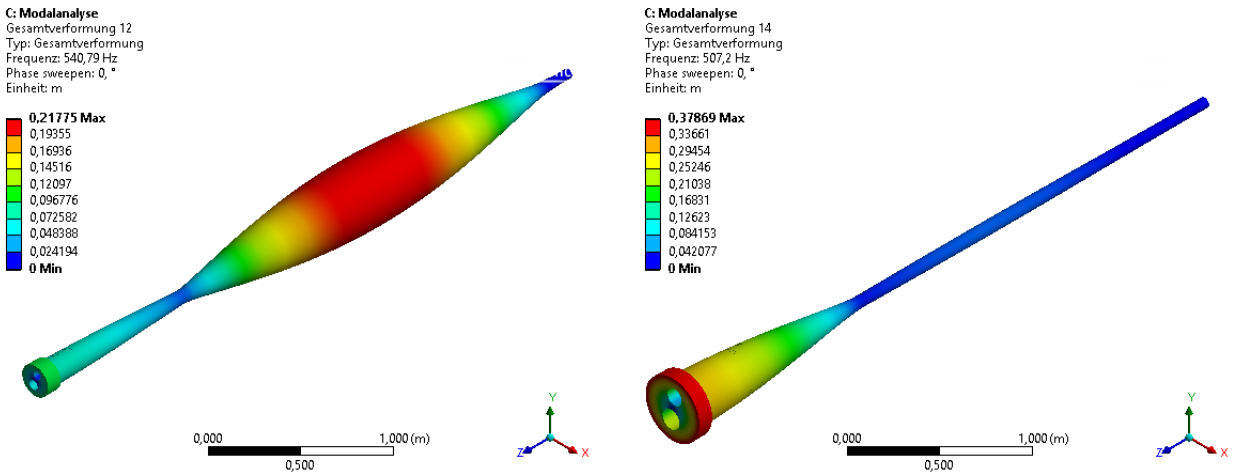

(a) Torsional eigenmode 1 for 100 mm.

(b) Torsional eigenmode 1 for 400 mm.

Figure 5.29: Torsional eigenmode 1 for 100 and 400 mm with moving Lanchester damper

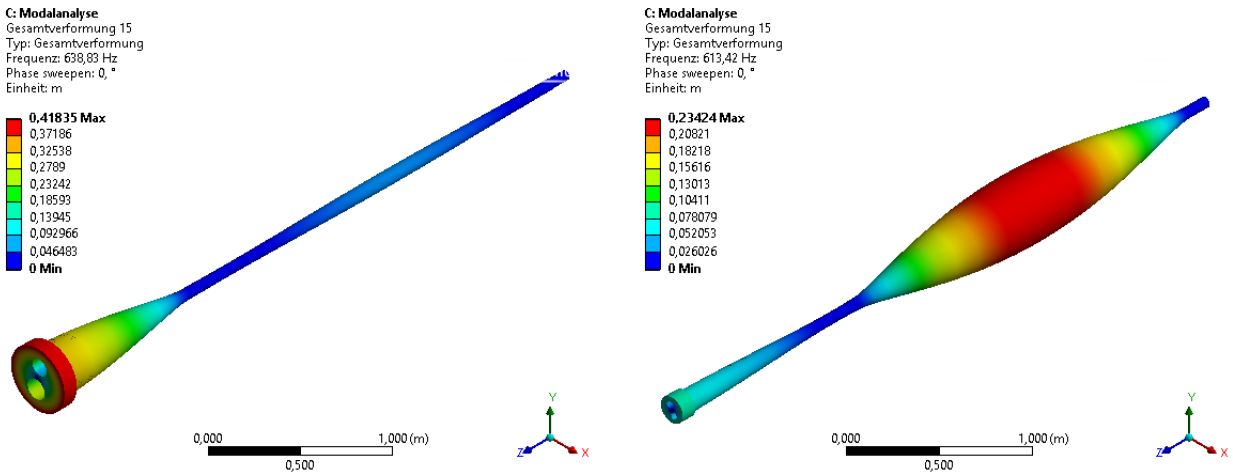

(a) Torsional eigenmode 2 for 100 mm.

(b) Torsional eigenmode 2 for 400 mm.

Figure 5.30: Torsional eigenmode 2 for 100 and 400 mm with moving Lanchester damper

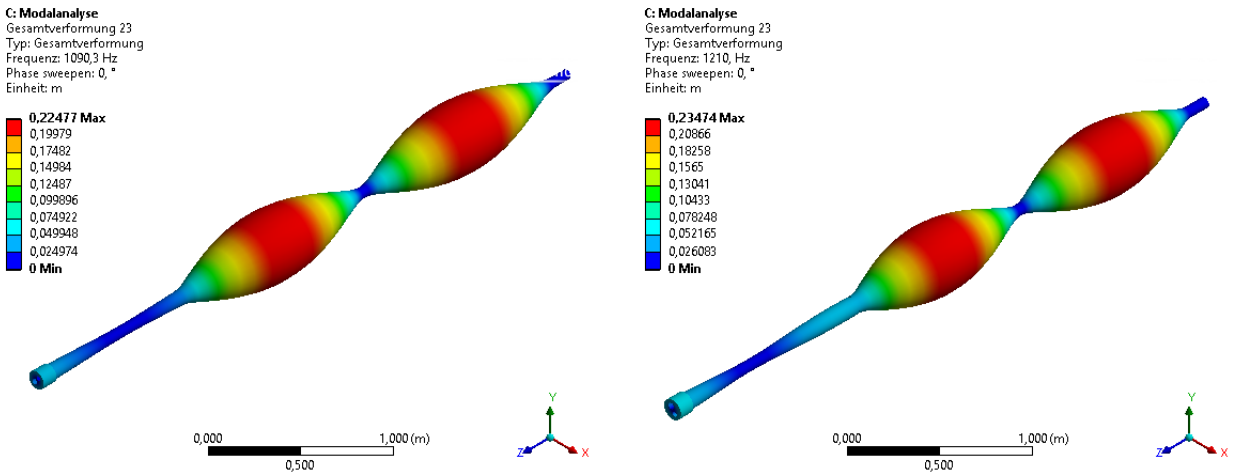

(a) Torsional eigenmode 3 for 100 mm.

(b) Torsional eigenmode 3 for 400 mm.

Figure 5.31: Torsional eigenmode 3 for 100 and 400 mm with moving Lanchester damper

6 Summary

BTA deep hole drilling has the reputation for precise finish to meet the demand of high quality of the manufactured bore during the deep hole drilling process. However, due to the high length-to-diameter ratio, BTA tool is susceptible to self-excited torsional and bending vibrations, which lead to chatter vibration and spiralling respectively. The chatter vibration could generate harsh noise and damage the BTA tool head while the spiralling causes the helical propagation of a multi-lobe like cross section and affects the inner of the bore during the deep hole drilling process. As BTA deep drilling is usually applied as the last step of the whole manufacturing procedure, the economic cost due to the dynamic instability is immeasurable.

The purpose of this thesis is via studying the self-excited torsional and bending vibrations during the BTA deep hole drilling process with numerical simulation based on Finite Element Method to support further researches regarding predictions and countermeasures for BTA deep hole drilling method.

3D model of the studied BTA tool was topologically improved in FEM software and essential convergence studies were executed with respect to relevant modules of the simulation for a higher quality of the pre-processing and satisfying reliability of the output. The corresponding real working and boundary conditions were studied and analysed.

Campbell diagrams in rotor dynamics analysis illustrated the critical rotational speeds for the corresponding eigenfrequencies at different drilling depths with different setups of the Lanchester damper. A rotor dynamics analysis was executed to fulfill the completeness of this thesis and the results of the critical rotational speed didn't have a deep influence on the operation of the BTA deep hole drilling machine.

Pre-stressed modal analysis showed how the torsional and bending eigenfrequencies varied during the deep hole drilling process with different setup of Lanchester damper. In terms of working and boundary conditions, the fluid-structure interaction and varying elastic supports of components influence the determination of eigenfrequencies significantly while the influence of the mechanical loads on the BTA tool head were restricted due to the high elastic stiffness from the workpiece to the BTA tool head. The analysis regarding dominant eigenmodes showed the varying system dynamics with different drilling depths and the results gave the reference in terms of real-time monitoring of varying dominant eigenfrequencies and the corresponding critical locations on the boring bar to prevent dynamic instabilities. Comparing to the results of torsional eigenanalysis, in which the critical locations of the dominant modes don't vary, the bending eigenanalysis showed the real-time changed critical locations on the boring bar both for the first and second dominant eigenmodes, which are of vital importance in terms of prediction and prevention for spiralling. The tendency of the narrowing difference between the first and second dominant bending eigenmodes within some ranges of drilling depths with different setups of Lanchester damper was

also captured.

Furthermore, the setup of a moving Lanchester damper on the boring bar influenced the torsional and bending eigenmodes more significantly than the one of a fixed Lanchester damper. This was mainly due to the higher influence on the real-time rearrangement of the vibrational structure with a moving Lanchester damper than that with a fixed one.

The FE simulation could be integrated into the real-time monitoring unit of an automatic damping system on a BTA tool machine for prediction and prevention of chatter vibration and spiralling. The possible countermeasures are, e.g. rotational speed control, alternation of applied Lanchester damper with varying critical location on the boring bar or setup of additional dampers.

The 3D model has the potential to be further optimized in pre-processing in order to achieve higher precision of computation and reduce computational burden and elapsed time in case professional tools for FE pre-processing are applied. The complexity of the numerical and experimental works for the determination of essential factors could also be modified for different demands of precision in the future.

References

[1] Verein Deutscher Ingenieure (2006): *VDI 3210 Part 1 Deep-hole drilling*, VDI-Gesellschaft Produktionstechnik, Germany.

[2] Chyn-Shu Deng, Jih-Hua Chin (2004): *Roundness Errors in BTA Drilling and a eigenmodel of Waviness and Lobing Caused by Resonant Forced Vibrations of Its Long Drill Shaft*, Journal of Manufacturing Science and Engineering, August 2004. doi: 10.1115/1.1765142

[3] Yuh-Lin Perng, Jih-Hua Chin (1999): *Theoretical and experimental investigations on the spinning BTA deep-hole drill shafts containing fluids and subject to axial forces*, International Journal of Mechanical Sciences 41 (1999) 1301-1322

[4] Keizo Sakuma, Koichi Taguchi, Akio Katsuki (1980): *Study on Deep-hole-drilling with Solid-boring Tool-The Burnishing Action of Guide Pads and Their Influence on Hole Accuracies*, Bulletin of the JSME, Vol. 23, No. 185, November 1980

[5] Wolfrum, P.; Gepperth, A.; Sandamirskaya, Y.; Webber, Oliver; Raabe, Nils (2006): *eigenmodelling and Understanding of Chatter*, Technical Report / Universität Dortmund, SFB 475 Komplexitätsreduktion in Multivariaten Datenstrukturen, No. 2006,22

[6] Fritz klocke, Wilfried König (2008): *Fertigungsverfahren 1: Drehen, Fräsen, Bohren*, Springer-Verlag 2008, 8.Auflage, Berlin, Heidelberg, Germany

[7] Jih-Hua Chin, Chi-Ti Hsieh and Li-Wei Lee (1996): *The Shaft Behavior Of BTA Deep Hole Drilling Tool*, International Journal of Mechanical Sciences. Vol. 38, No. 5, pp. 461-182, 1996

[8] Jih-Hua Chin and Li-Wei Lee (1995): *A Study On The Tool Eigenproperties Of A BTA Deep Hole Drill-Theory And Experiments*, International Journal of Machine Tools and Manufacture. Vol. 35. No. 1. pp. 29-49. 1995

[9] Tlustý, Polaček, Daněk, Špaček (1962): *Selbsterregte Schwingungen an Werkzeugmaschinen*, VEB Verlag. Technik, Berlin, 1962

[10] Weck Manfred, Brecher Christian (2006): *Werkzeugmaschinen, Fertigungssysteme. 5. Messtechnische Untersuchung und Beurteilung, dynamische Stabilität*, Springer, 7.Auflage, Berlin, 2006

[11] Dieter Bolle (1991): *Ein System zur automatischen Dämpfung von Ratterschwingungen beim BTA-Tiefbohren*, Dissertation, Universität Dortmund, 1991

[12] Thanh-Phuong Thai (1983): *Beitrag zur Untersuchung der selbsterregten Schwingungen von Tiefbohrwerkzeugen*, Dissertation, Universität Dortmund, 1983

[13] R.Stockert (1977): *Dralleffekte beim Tiefbohren*, VDI 301, VDI-Verlag, Düsseldorf, 1977

[14] K. Weinert, O.Webber, C. Peters (2005): *On the Influence of Drilling Depth Dependent Modal Damping on Chatter Vibration in BTA Deep Hole Drilling*, CIRP Annals - Manufacturing Technology, Volume 54, Issue 1, 2005, Pages 363-366. doi:10.1016/S0007-8506(07)60123-1

[15] G.Szepannek, N.Raabe, O.Webber, C.Weihs (2006): *Prediction of spiralling in BTA deep-hole drilling – estimating the system's eigenfrequencies*, University of Dortmund, 2006

[16] Kenichiro Matsuzaki, Takahiro Ryu, Atsuo Sueoka, Keizo Tsukamoto (2015): *Theoretical and experimental study on rifling mark generating phenomena in BTA deep hole drilling process (generating mechanism and countermeasure)*, International Journal of Machine Tools and Manufacture 88 (2015) 194–205. http://dx.doi.org/10.1016/j.ijmachtools.2014.10.003

[17] Lingfei Kong, Jih-Hua Chin, Yan Li, Yanjun Lu, Pengyang Li (2014): *Targeted suppression of vibration in deep hole drilling using magneto-rheological fluid damper*, Journal of Materials Processing Technology 214 (2014) 2617–2626. http://dx.doi.org/10.1016/j.jmatprotec.2014.05.029

[18] Oliver Webber (2007): *Untersuchung zur bohrtiefenabhängigen Prozessdynamik beim BTA-Tiefbohren*, Dissertation, Universität Dortmund, 2007

[19] Nils Raabe (2010): *Physikalisch-Statistische Modellierung von Biegeschwingungen*, Dissertation, Technische Universität Dortmund, 2010

[20] Y. B. Gessesse, V. N. Latinovic, M. O. M. Osman (1994): *On the Problem of Spiralling in BTA Deep-Hole Machining*, Journal of Engineering for Industry, May 1994, Vol. 116/161

[21] Theis, Winfried; Webber, Oliver; Weihs, Claus (2004) : *Statistics, dynamics and quality: Improving BTA-deep-hole drilling, Technical Report//* Universität Dortmund, SFB 475 Komplexitätsreduktion in Multivariaten Datenstrukturen, No. 2004,06

[22] Klaus Weinert, Oliver Webber, Anja Busse, Michael Hüsken, Jörn Mehnen, Peter Stagge (2001): *Experimental Investigation of the Dynamics of the BTA Deep Hole Drilling Process*, Production Engineering. Research and Development, 13 (2001) 2, pp. 1-4

[23] K. Weinert, O. Webber, M. Hüsken, J. Mehnen, W. Theis (2002): *Analysis and Prediction of Dynamic Disturbances of the BTA Deep Hole Drilling Process*, Department of Machining Technology, University of Dortmund; Institut fur Neuroinformatik, Ruhr-Universität, Bochum; Lehrstuhl fur Computergestützte Statistik, University of Dortmund, Germany

[24] François Axisa, Jose Antunes (2007): *eigenmodelling of Mechanical Systems (Volume 3): Fluid-Structure Interaction*, Butterworth-Heinemann; 1 edition (December 21, 2006)

[25] Joris Degroote, Klaus-Jürgen Bathe, Jan Vierendeels (2009): *Performance of a new partitioned procedure versus a monolithic procedure in fluid–structure interaction*, Computers and Structures 87 (2009) 793–801. doi:10.1016/j.compstruc.2008.11.013

[26] Hong Zhao, Jonathan B. Freund, Robert D. Moser (2008): *A fixed-mesh method for incompressible flow–structure systems with finite solid deformations*, Journal of Computational Physics 227 (2008) 3114–3140. doi:10.1016/j.jcp.2007.11.019.

[27] Gene Hou, Jin Wang and Anita Layton (2012): *REVIEW ARTICLE Numerical Methods for Fluid-Structure Interaction — A Review*, Communications in Computational Physics. Vol. 12, No. 2, pp. 337-377, August 2012. doi: 10.4208/cicp.291210.290411s.

[28] Hermann G. Matthies, Jan Steindorf (2003): *Partitioned strong coupling algorithms for fluid–structure interaction*, Computers and Structures 81 (2003) 805–812. doi:10.1016/S0045-7949(02)00409-1.

[29] Nils Raabe (2010): *Physikalisch-Statistische eigenmodellierung von Biegeschwingungen*, Dissertation, Technische Universität Dortmund, 2010

[30] Jeffrey C. Lagarias, James A. Reeds, Margaret H. Wright, Paul E. Wright (1998): *CONVERGENCE PROPERTIES OF THE NELDER–MEAD SIMPLEX METHOD IN LOW DIMENSIONS*, Society for Industrial and Applied Mathematics. SIAM J. OPTIM Vol. 9, No. 1, pp. 112–147. 1998

[31] D. J. Ewins (2000): *Modal Testing: Theory, Practice and Application, 2nd Edition* WILEY, 2nd Edition, 2000

[32] Manolis Papadrakakis, Nikos D. Lagaros and Vagelis Plevris (2000): *Optimum Design Of 3D Structures Under Static And Dynamic Loading* Computational Methods for Shell and Spatial Structures, IASS-IACM 2000

[33] Tom Irvine (2012): *Bending Frequencies Of Beams, Rods, And Pipes Revision S* Vibrationdata, November 20, 2012

[34] Tom Irvine (2015): *Effective Modal Mass & Modal Participation Factors Revision I* Vibrationdata, December 11, 2015

[35] UNISIG Deep Hole Drilling System: *http://www.unisig.com*

[36] Tiefbohren Info: *http://www.tiefbohr-lexikon.de/*

Appendices

A Input values for FE simulation

Drilling depth in mm	$k_{LD} \times 10^{10}$ in $\frac{N}{m}$	$k_W \times 10^7$ in $\frac{N}{m}$	$c_{SB,1/2}$ in $\frac{Nms}{rad}$	
50	4.91	2.68	0	1.42
100	5.21	2.68	0	1.42
150	5.37	2.68	0	1.42
200	5.52	2.68	0	1.42
250	5.82	2.68	0	1.42
300	6.07	2.68	0	1.42
350	6.32	2.68	0	1.42
400	6.61	2.68	0	1.42
450	6.83	2.68	0	1.42
500	7.15	2.68	0	1.42
550	7.37	2.68	0	1.42
600	7.62	2.68	0	1.42
650	7.87	2.67	0	1.42
700	8.21	2.67	0	1.42
750	8.46	2.67	0	1.42
800	8.72	2.67	0	1.42
850	8.91	2.67	0	1.42
900	9.17	2.67	0	1.42
950	9.48	2.67	0	1.42
1000	9.89	2.67	0	1.42
mean value	7.29	2.68	0	1.42

Table A.1: Input data for boundary conditions part 1.

Drilling depth in mm	α in $\frac{1}{s \cdot rad}$	β in s	$L_{LD,left/right}/L_{LD}$	$k_{SB,1/2} \times 10^7$ in $\frac{N}{m}$	
50	128.57	0	0.1	2.11	4.89
100	128.57	0	0.1	2.26	2.03
150	128.57	0	0.1	2.46	1.12
200	128.57	0	0.1	2.63	0.93
250	128.57	0	0.1	2.81	0.87
300	128.57	0	0.1	3.01	0.78
350	128.57	0	0.1	3.18	0.71
400	128.57	0	0.1	3.37	0.63
450	128.57	0	0.1	3.52	0.57
500	128.57	0	0.1	3.72	0.39
550	128.57	0	0.1	3.93	0.23
600	128.57	0	0.1	4.12	0.17
650	128.57	0	0.1	4.31	0.09
700	128.57	0	0.1	4.52	0.09
750	128.57	0	0.1	4.73	0.08
800	128.57	0	0.1	4.92	0.07
850	128.57	0	0.1	5.11	0.06
900	128.57	0	0.1	5.29	0.03
950	128.57	0	0.1	5.52	0.02
1000	128.57	0	0.1	5.79	0.01
mean value	128.57	0	0.1	3.88	0.71

Table A.2: Input data for boundary conditions part 2.

Drilling depth in mm	Moment $M_{N/P}$ in Nm		Torque M_T in Nm	Force F_{axial} in N
50	-43.27	-22.78	227.23	8492.71
100	-45.86	-24.95	223.86	8509.35
150	-39.74	-20.07	228.66	8553.03
200	-42.27	-26.07	230.63	8355.02
250	-46.88	-25.43	233.61	8584.24
300	-40.90	-22.75	224.42	8397.01
350	-39.44	-19.37	221.15	8477.98
400	-46.21	-24.50	223.62	8504.35
450	-45.96	-20.06	227.19	8512.47
500	-42.26	-23.45	226.77	8624.80
550	-47.27	-22.56	224.81	8433.94
600	-40.71	-23.61	225.09	8667.49
650	-41.31	-21.68	223.75	8597.24
700	-44.39	-22.98	226.29	8607.16
750	-43.75	-19.70	220.97	8474.50
800	-45.97	-23.93	221.37	8563.56
850	-47.17	-25.71	226.05	8607.21
900	-45.16	-23.11	223.92	8548.35
950	-44.92	-24.82	226.83	8520.79
1000	-43.84	-22.77	225.29	8476.82
mean value	-42.30	-24.32	226.08	8499.47

Table A.3: Input data for mechanical loads.

B Code in Matlab for numerical approximation

```
%%%%%%%%%%%%%%%%%%%%%%%%%%%%%%%%%%%%%%%%%%%%%%%%%%%%%%%%%%%%%%%%%%%%%%%%%%%%%%%%
clear;                              %Bending part
close all;
pho=7700;da=0.062;di=0.048;
Ld=0.08;lbr=3.595;E=212000*10^6;
N=130;                              %Discretization
I=pi*(da^4-di^4)/64;
mseg=pho*pi*(da^2-di^2)*lbr/4/N;
lseg=lbr/N;
summe=0;
for i=1:N
    summe=summe+i^2;
end
Kbseg=3*E*I/lbr/N^2*summe;
Kd_li=0;                            %Input from experiments
Kd=1.58*10^10;
Kd_re=0;
Ksb1=1.78*10^7;
Ksb2=2.95*10^7;
Kbk=1.18*10^7;
alpha=102;                          %Initiation of unknown material damping
beta=0.2;
M1 = 1:1;                           %Mass matrix of discrete system
V1 = repmat(M1', 1, N)';
M2 = V1(:);
M=mseg*diag(M2);
K1=1:1;                             %Stiffness matrix of discrete system
V2= repmat(K1', 1, N-2)';
K2=V2(:);
K3=1:1;
V3= repmat(K3', 1, N-2)';
K4=V3(:);
K5=-4:-4;
```

```
V4= [repmat(K5', 1, N-2) -2];
K6=V4(:);
K7=-4:-4;
V5= [repmat(K7', 1, N-2) -2];
K8=V5(:);
K9=6:6;
V6= [repmat(K9', 1, N-2) 5 1];
K10=V6(:);
K11=0:0;
V7= [repmat(K11', 1, N-50) Kd_li Kd...
 Kd Kd Kd Kd_re repmat(K11', 1, 44)];  %Arranging position of Lanchester damper
K12=V7(:);
K13=0:0;
V8= [repmat(K13', 1, N-40) Ksb1 repmat(K13', 1, 10)...
           Ksb2 repmat(K13', 1, 28)];  %Arranging position of stuffing box
K14=V8(:);
K15=0:0;
V9= [repmat(K15', 1, N-1) Kbk];        %Workpiece
K16=V9(:);
K=Kbseg/(lseg^2)*(diag(K2,2)+diag(K4,-2)...
    +diag(K6,1)+diag(K8,-1)+diag(K10))...
    +diag(K12)+diag(K14)+diag(K16);
C=alpha*M+beta*K;                      %Damping matrix
A = [zeros(size(M)), eye(size(M,1)); -inv(M)*K, -inv(M)*C];
e = eig(A);
abse = abs(imag(e));
fcomp=zeros(N,1);
for i=1:N
fcomp(i,1)=abse(2*i-1)/2/pi;
end
B = sort(fcomp);
fmessen=[100,110,200,280,350];        %Experimental input of frequency
SSE=0;
for j=1:5
    SSE=SSE+(B(j,1)-fmessen(1,j))^2;
end
```

```
h=SSE;
%%%%%%%%%%%%%%%%%%%%%%%%%%%%%%%%%%%%%%%%%%%%%%%%%%%%%%%%%%%%%%%%%%%%%%%%%%%%
clear;                                          %Torsional part
close all;
pho=7700;da=0.062;di=0.048;lbr=3.595;E=212000*10^6;miu=0.27;
G=E/2/(1+miu);
N=60;
Iseg=pho*pi*(da^4-di^4)*lbr/32/N;
Ktseg=G*pi*(da^4-di^4)*N/32/lbr;

M1 = 1:1;
V1 = repmat(M1', 1, N)';
M2 = V1(:);
M=Iseg*diag(M2);                                %Mass matrix of discrete system
K1=-1:-1;
V2= repmat(K1', 1, N-1)';
K2=V2(:);
K3=-1:-1;
V3= repmat(K3', 1, N-1)';
K4=V3(:);
K5=2:2;
V4= [repmat(K5', 1, N-1) 1];
K6=V4(:);
K=Ktseg*(diag(K2,1)+diag( K4,-1)+diag(K6)); %Stiffness matrix of discrete system
alpha=102;                                      %Result from bending part
beta=0;

Csb1=0;                                         %Initiation of unknown factors
Csb2=1.11;

C1=0:0;
V5= [repmat(C1', 1, N-40) Csb1 repmat(C1', 1, 10)...
    Csb2 repmat(C1', 1, 28)];                   %Arranging position of stuffing box
C2=V5(:);
C=alpha*M+beta*K+diag(C2);                      %Damping matrix
```

```
A = [zeros(size(M)), eye(size(M,1)); -inv(M)*K, -inv(M)*C];
e = eig(A);
abse = abs(imag(e));
fcomp=zeros(N,1);
for i=1:N
fcomp(i,1)=abse(2*i-1)/2/pi;
end
B = sort(fcomp);
fmessen=[100,110,200];                    %Experimental input of frequency
SSE=0;
for j=1:3
    SSE=SSE+(B(j,1)-fmessen(1,j))^2;
end
h=SSE;
%%%%%%%%%%%%%%%%%%%%%%%%%%%%%%%%%%%%%%%%%%%%%%%%%%%%%%%%%%%%%%%%%%%%%%%%%%%%%%%
```

C Plots of eigenmodes for 700 and 1000 mm drilling depths

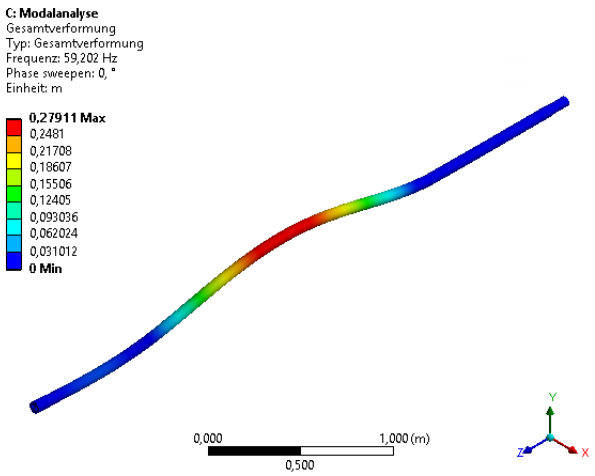

(a) Bending eigenmode 1 for 700 mm.

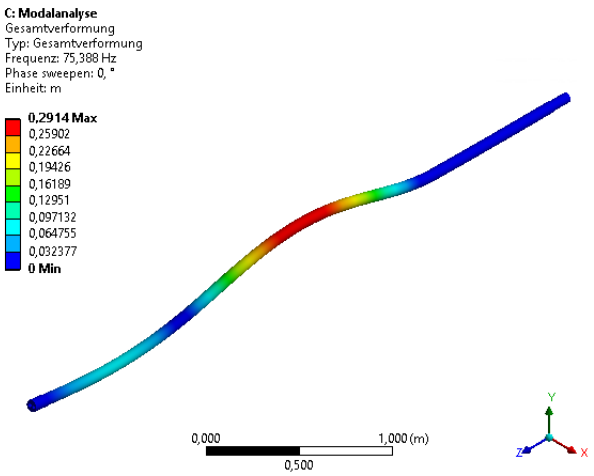

(b) Bending eigenmode 1 for 1000 mm.

Figure C.1: Bending eigenmode 1 for 700 and 1000 mm with fixed Lanchester damper

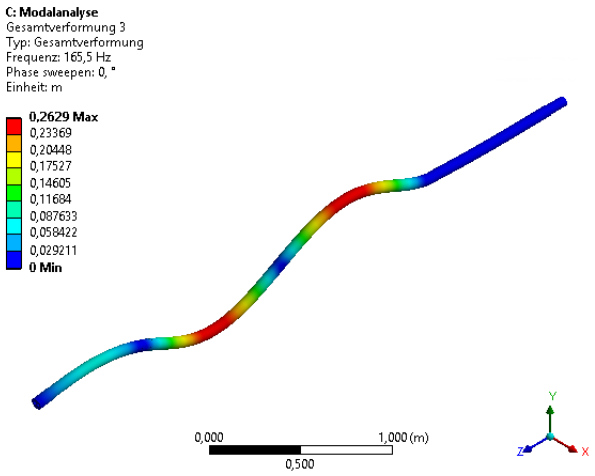

(a) Bending eigenmode 2 for 700 mm.

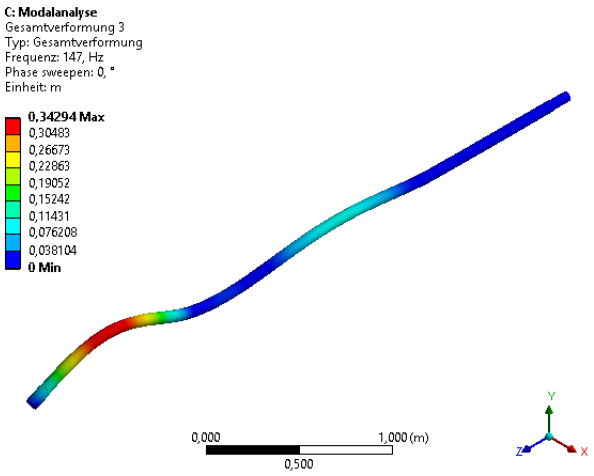

(b) Bending eigenmode 2 for 1000 mm.

Figure C.2: Bending eigenmode 2 for 700 and 1000 mm with fixed Lanchester damper

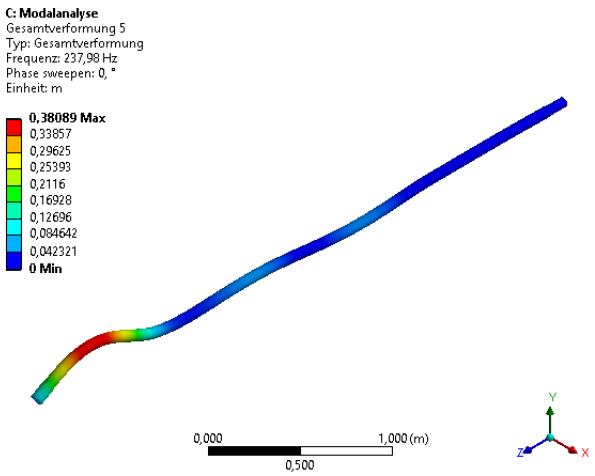

(a) Bending eigenmode 3 for 700 mm.

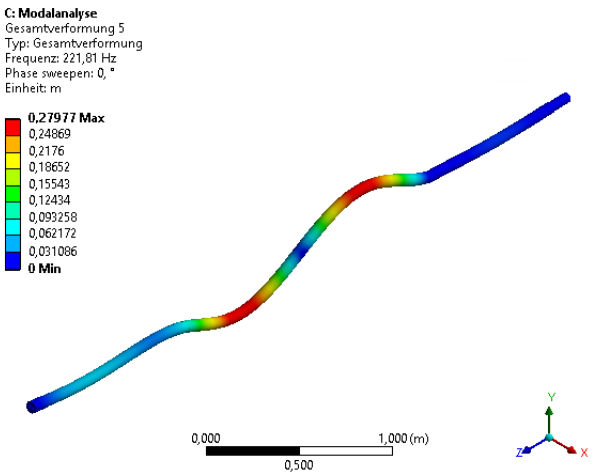

(b) Bending eigenmode 3 for 1000 mm.

Figure C.3: Bending eigenmode 3 for 700 and 1000 mm with fixed Lanchester damper

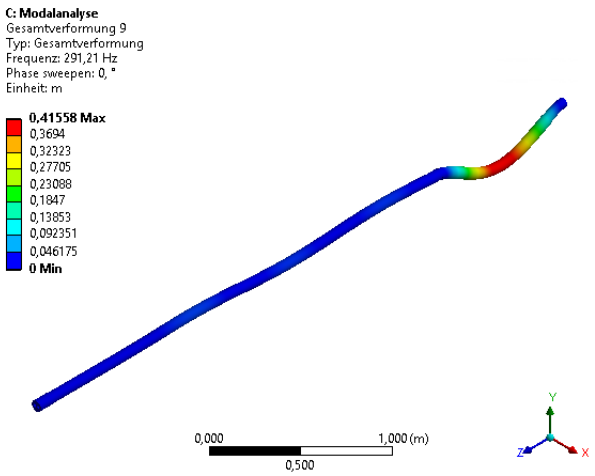

(a) Bending eigenmode 4 for 700 mm.

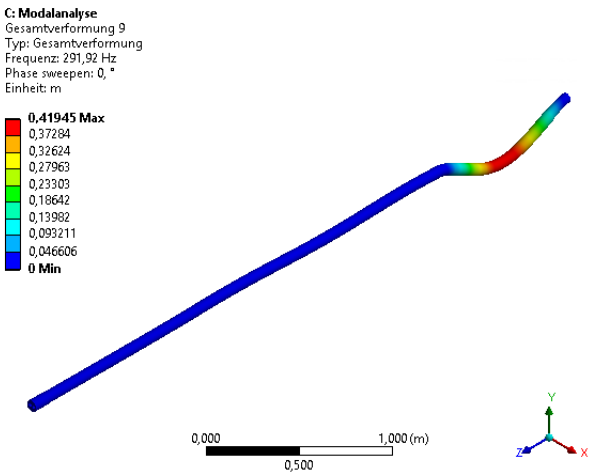

(b) Bending eigenmode 4 for 1000 mm.

Figure C.4: Bending eigenmode 4 for 700 and 1000 mm with fixed Lanchester damper

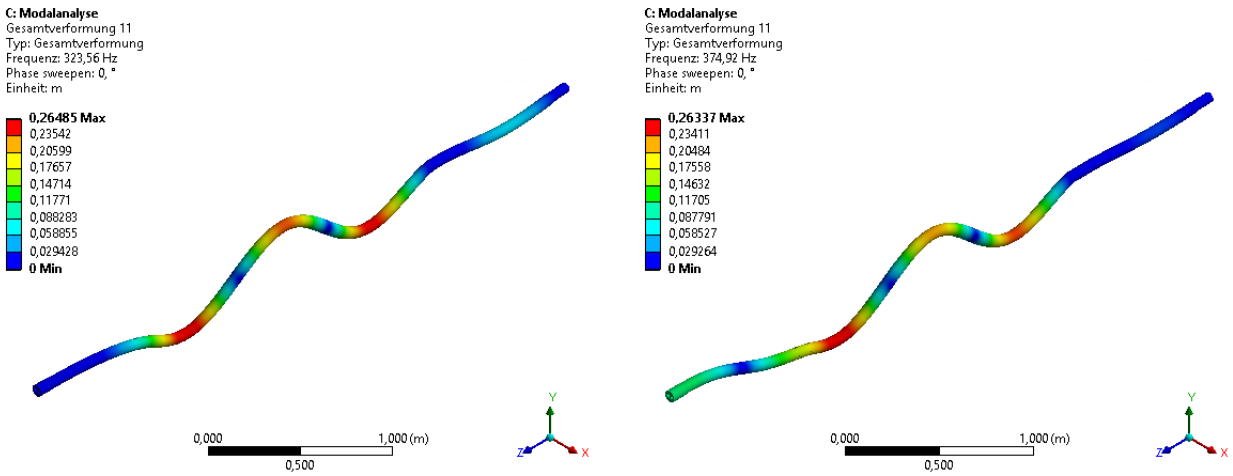

(a) Bending eigenmode 5 for 700 mm.

(b) Bending eigenmode 5 for 1000 mm.

Figure C.5: Bending eigenmode 5 for 700 and 1000 mm with fixed Lanchester damper

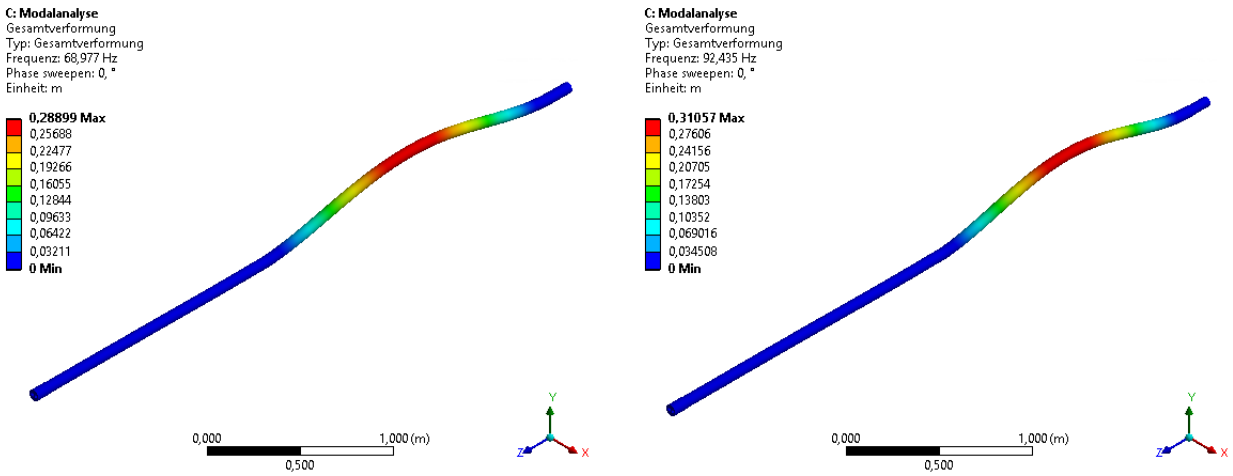

(a) Bending eigenmode 1 for 700 mm.

(b) Bending eigenmode 1 for 1000 mm.

Figure C.6: Bending eigenmode 1 for 700 and 1000 mm with moving Lanchester damper

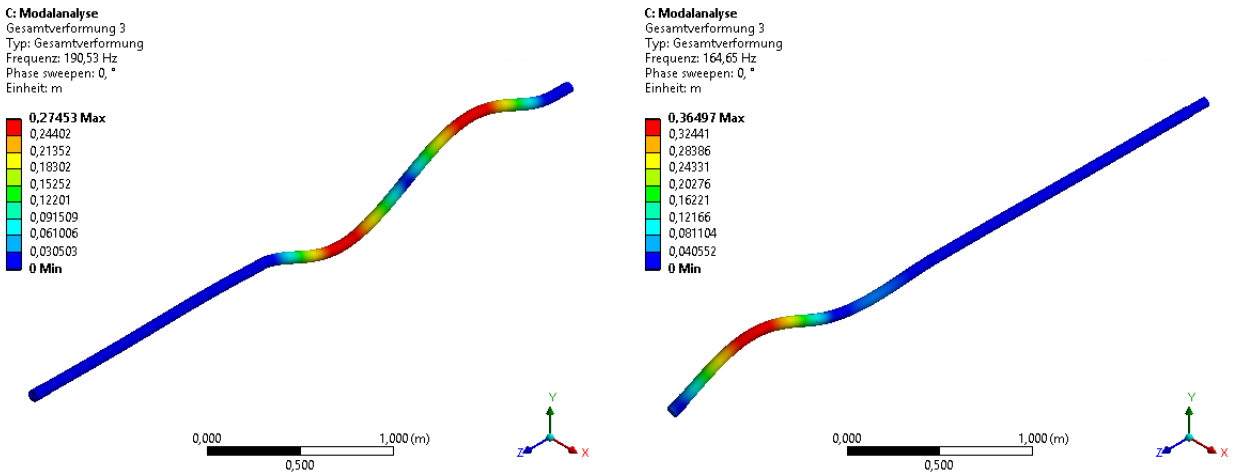

(a) Bending eigenmode 2 for 700 mm.

(b) Bending eigenmode 2 for 1000 mm.

Figure C.7: Bending eigenmode 2 for 700 and 1000 mm with moving Lanchester damper

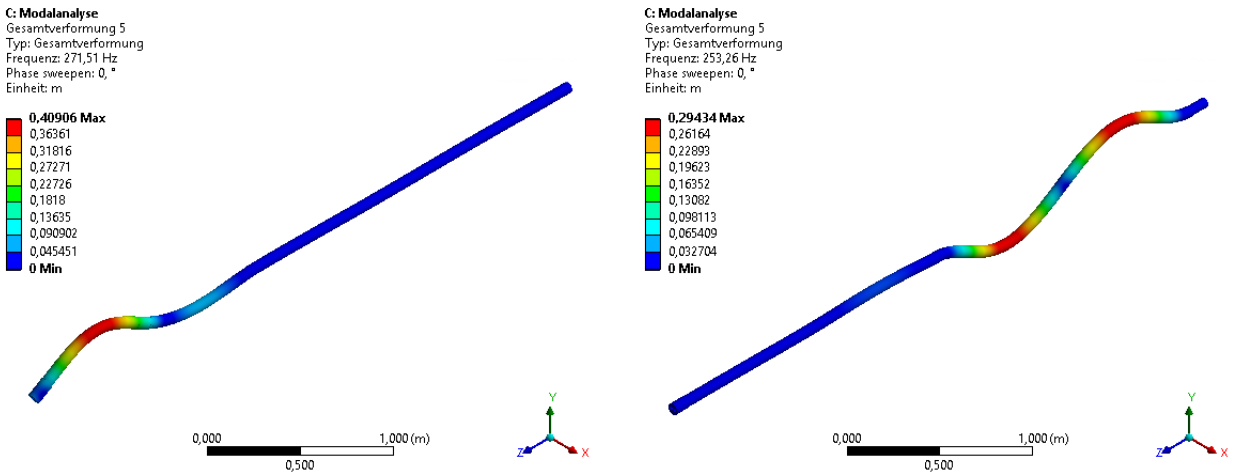

(a) Bending eigenmode 3 for 700 mm.

(b) Bending eigenmode 3 for 1000 mm.

Figure C.8: Bending eigenmode 3 for 700 and 1000 mm with moving Lanchester damper

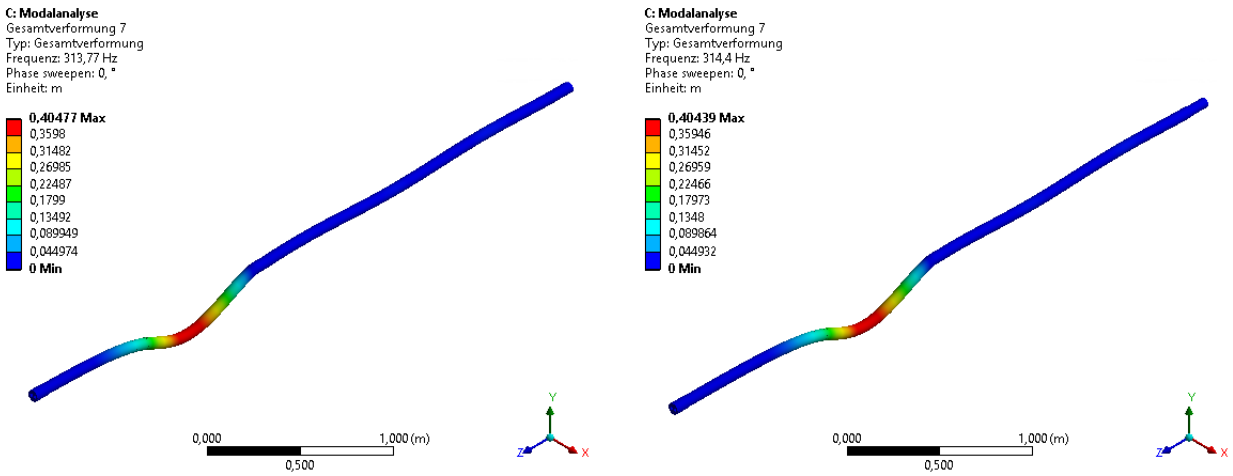

(a) Bending eigenmode 4 for 700 mm.

(b) Bending eigenmode 4 for 1000 mm.

Figure C.9: Bending eigenmode 4 for 700 and 1000 mm with moving Lanchester damper

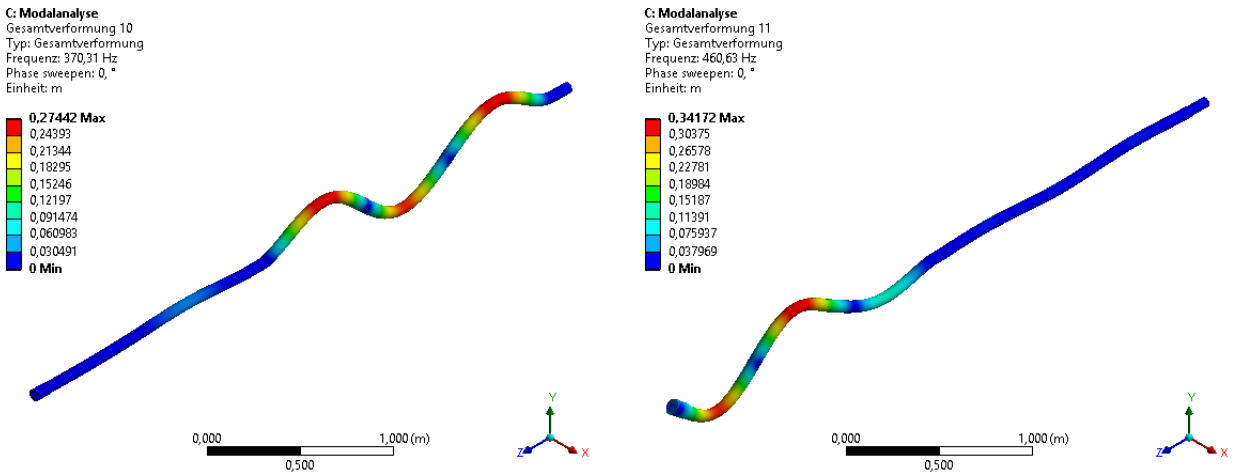

(a) Bending eigenmode 5 for 700 mm.

(b) Bending eigenmode 5 for 1000 mm.

Figure C.10: Bending eigenmode 5 for 700 and 1000 mm with moving Lanchester damper

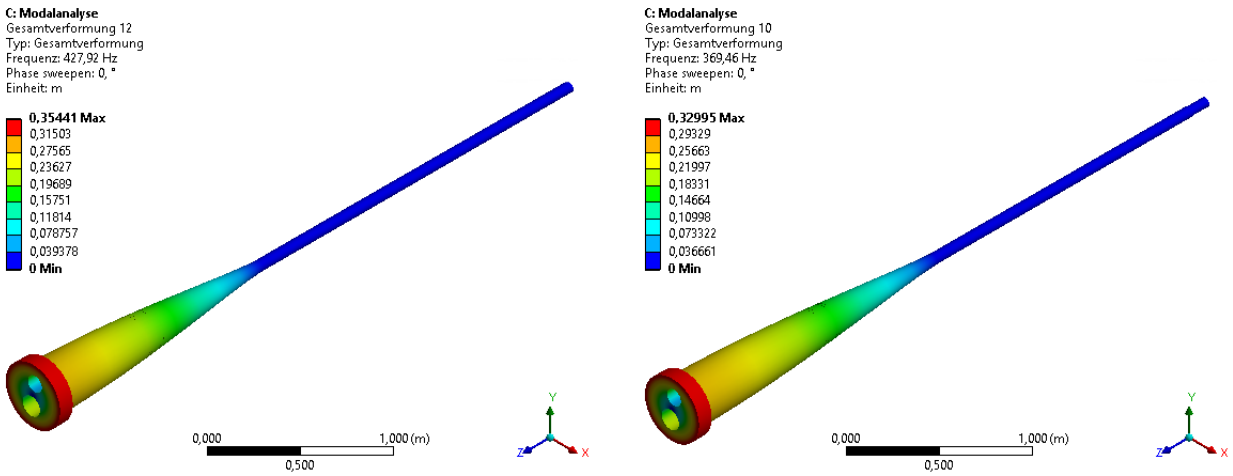

(a) Torsional eigenmode 1 for 700 mm.

(b) Torsional eigenmode 1 for 1000 mm.

Figure C.11: Torsional eigenmode 1 for 700 and 1000 mm with moving Lanchester damper

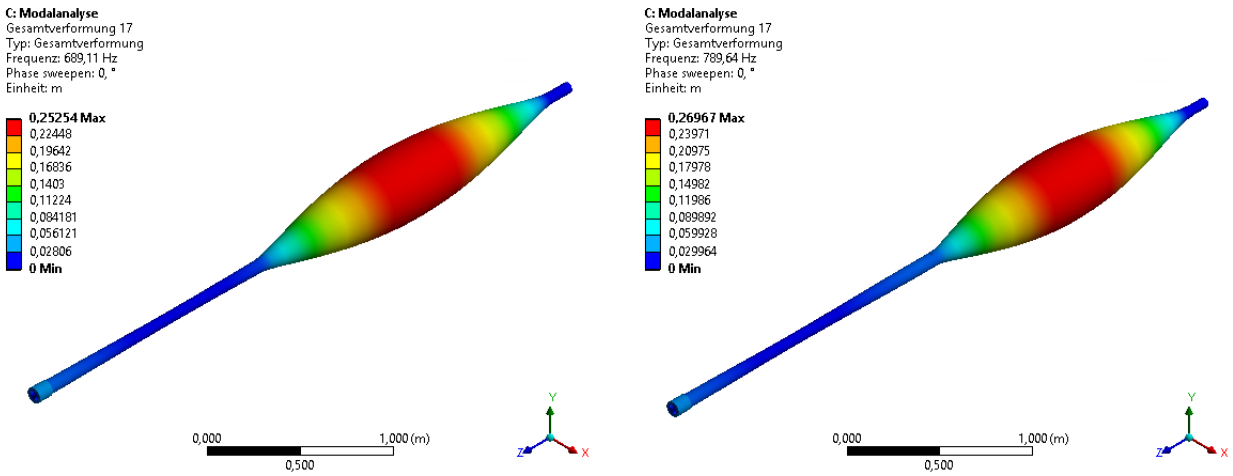

(a) Torsional eigenmode 2 for 700 mm.

(b) Torsional eigenmode 2 for 1000 mm.

Figure C.12: Torsional eigenmode 2 for 700 and 1000 mm with moving Lanchester damper

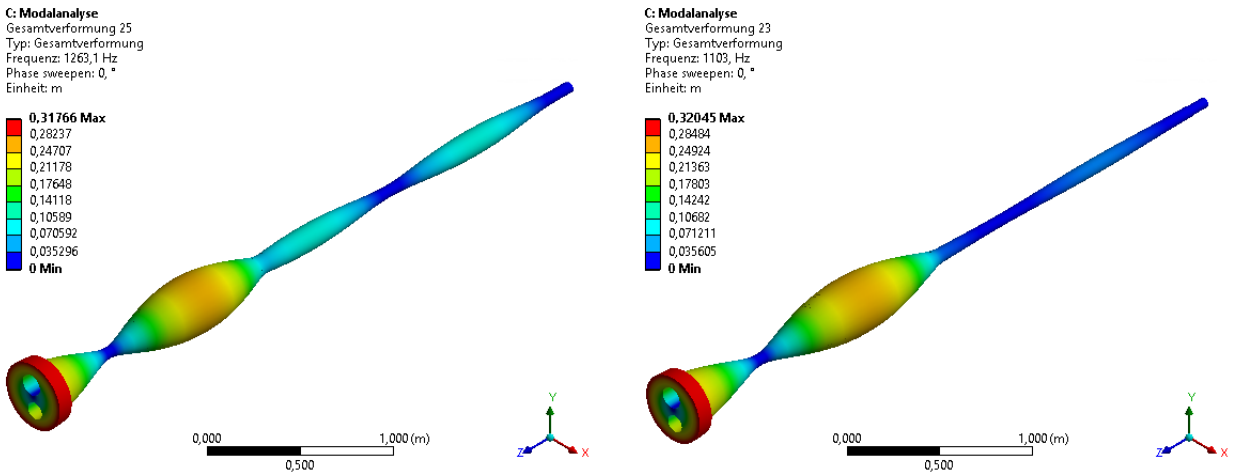

(a) Torsional eigenmode 3 for 700 mm.

(b) Torsional eigenmode 3 for 1000 mm.

Figure C.13: Torsional eigenmode 3 for 700 and 1000 mm with moving Lanchester damper

List of Figures

List of Tables

Formula Directory